ISSN: 1847-9286
Open Access Journal
www.jese-online.org

JESE

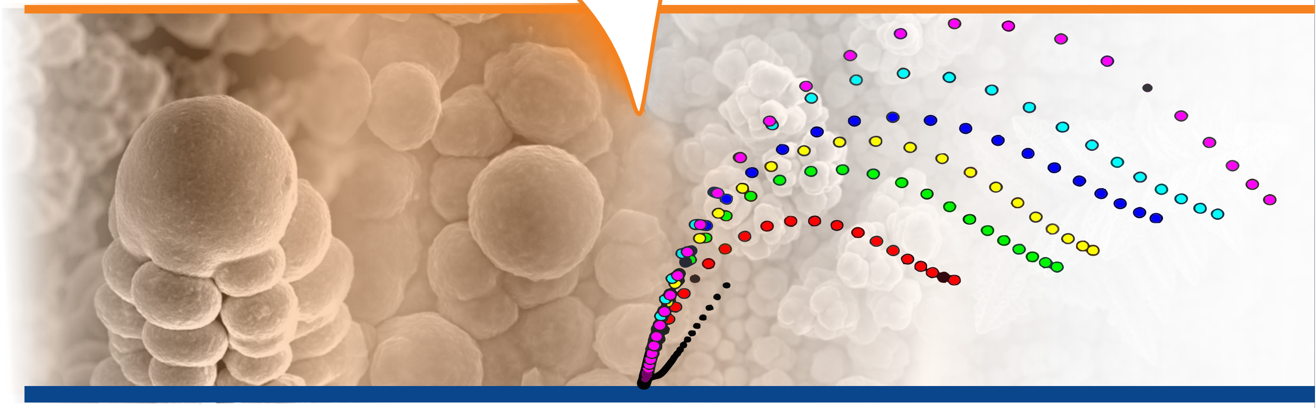

Journal of Electrochemical Science and Engineering

J. Electrochem. Sci. Eng. **6**(**3**) 2016, 215-276

IAPC
PUBLISHING

J. Electrochem. Sci. Eng. **6(3)** (2016) 215-223; doi: **10.5599/jese.296**

Open Access : : ISSN 1847-9286
www.jESE-online.org

Original scientific paper

An improved method of water electrolysis – effect of complexing agent

Seetharaman Swaminathan*, **, Balaji Rengarajan*, Ramya Krishnan*, ✉,
Kaveripatnam Samban Dhathathreyan*, Manickam Velan**

**Centre for Fuel Cell Technology, International Advanced research Centre for Powder Metallurgy and New Materials(ARCI), II Floor, IIT-M Research Park, No.6 Kanagam road, Taramani, Chennai – 600 113, India*
***Department of Chemical Engineering, A.C. College of Technology, Anna University, Chennai-600 025, India*

✉Corresponding Author: ramya.k.krishnan@gmail.com,Fax: +91-44-66632702

Received: May 17, 2016; Revised: July 1, 2016; Accepted: July4, 2016

Abstract

The present work investigates the efficiency of an alkaline water electrolysis process in the presence of a complexing agent like citric acid (CA) when added directly into the electrolyte during the electrolytic process. High surface area nickel electrodes prepared by electrodeposition technique were used as the electrode to evaluate the efficiency of the oxygen evolution reaction (OER) by the polarization measurements and cyclic voltammetry. The quantity of the complexing agent CA in the electrolyte was varied from 0-1 wt. %. An increase in the current density of about 25 % resulted at a temperature of 30 °C in the presence of 0.2 wt. % of CA at 1.0 V vs. Hg/HgO. CA was found to improve performance by forming a complex with the alloy electrode and by formation of the high surface area catalyst for efficient OER.

Keywords
Citric acid; Alkaline water electrolysis; Oxygen evolution reaction; Complexing agent

---

Introduction

Clean energy is considered as the solution to world's increasing energy demand and to concerns regarding pollution and contamination. Hydrogen is important energy alternatives as its combustion product is only water. Water electrolysis is the best technology for producing hydrogen and oxygen with no resulting greenhouse gas emissions [1-3]. The energy required for production of hydrogen by electrolytic method is very high (4.5-5 kWh N m^{-3} of H_2) in most industrial electrolyzers. Alkaline water electrolysis (AWE) offers the advantages of the use of non-noble metal catalysts, ease of manufacturing and scalability. Therefore, research on suitable catalyst materials and methods for modifying the electrodes to improve efficiency of water electrolysis techniques are always being carried out. Efficiency in electrolysis can be improved by reducing the cell voltage through the use of catalysts with increased surface area or by changing the nature of the overpotential of the reaction. In AWE anodic overpotential is a major factor that limits the efficiency and hence is researched frequently [4-6]. Ni based electrodes, being less corrosive in alkaline solution, offer low cost solution despite its higher overpotential in alkaline solutions when compared to costly RuO_2 and IrO_2 based catalyst used in acidic media [7]. Further, it has been found that incorporation of zinc and sulphur in the nickel electrode increases surface area and catalytic activity, lowers overvoltage and helps in increasing the current density by removal of the gas bubbles from the electrode surface [8].

Citric acid (CA) is a chelating agent often used for depositing metals at a controlled rate in electroplating and electroless plating operations. It is also used to buffer the pH of the plating bath. The effects of additives in the electroless nickel deposition process have been studied by electrochemical analysis [9,10]. It has been shown that the additives significantly improved the deposition rate and helped in forming finer grain structure during the plating process. The importance of additives such as boric acid, citric acid and ascorbic acids in influencing the electrodeposition of nickel alloys was described by Kieling [11]. It was shown that complexing agents influence the kinetics of powder electrodeposition, as well as the morphology of the Ni powders. According to the conclusion of the authors finer powders were produced in the presence of citric acid than those obtained with oxalic acid. A study on organic additive, tri sodium citrate as a stabilizing agent reveals that they can be used for structure related factors to control the nucleation, growth and alignment of crystal phases [12,13].

Nikolić *et al.* [14] have shown that alkaline electrolytic hydrogen production can be made efficient (~15 %) by the addition of activating compounds of tungsten and cobalt in the ionic and complex form into the electrolyte (6 M KOH) during electrolytic process. Additions of ionic activators were found to increase surface area, porosity and performance due to the synergistic effect of the two different metals on the surface of the electrode. The effect of ionic activators and complexes in alkaline water electrolysis has been emphasized by improved performance in the presence of molybdate, chromate and cobalt based compounds [15,16]. The ability of citric acid to form complexes with Ni is very well established. It has been used to decrease the precipitation of Ni as hydroxides thus stabilizing it in the electrolyte. It has been used in both the electroless and electrodeposition of Ni and its alloys [17,18]. It was hence decided to study the effect of this stabilizer during the electrolysis of water by adding it to the electrolyte, *i.e.* to study whether the Ni citrate complex formed will act similar to the ionic activator and improve the efficiency of the electrolytic process. In the present system the activator is formed in situ from the electrode and the complexing agent in the solution compared to those in the literature where the metal complexes are externally added. A systematic study on OER has been carried out by varying the concentration of citric acid in the electrolyte between 0 and 1 % by weight.

Experimental

1. Materials

Nickel sulphate (Merck), nickel chloride (Merck), zinc sulphate (Merck), ammonium nickel sulfate (Merck), sodium thiocyanate (Fisher), potassium hydroxide (Merck), citric acid (Merck) and other chemicals were all used as received. Ni mesh (procured from Champion Manufacturing Co, India with 0.10×0.32×0.20 mm nominal thickness, long diagonals of the diamond and strand width respectively) of area 9.0 cm^2 size were used for preparation of the electrodes.

2. Electrode fabrication

The surface of nickel mesh was electrochemically cleaned before electroplating using the bath solution containing nickel chloride (240 g L^{-1}) and conc. HCl (125 ml L^{-1}). A plating current density of 50 mA cm^{-2} was used for cleaning. The plating bath consisting of nickel (II) sulphate (70 g l^{-1}), ammonium nickel sulfate (40 g L^{-1}), zinc sulphate (35 g L^{-1}) and sodium thiocyanate (12 g L^{-1}) were used for plating. Electrodes were prepared by the pulse electrodeposition technique as mentioned in our previous paper with a pH of 5-6, a current density of 40 mA cm^{-2} and duty cycle of 40 % under the influence of ultrasonic vibration [19]. Once the electrodeposition was concluded, the electrodes were treated with 28 g L^{-1} of KOH to leach out excess zinc to give a porous electrode having a high surface area.

3. Cell frame-up

Electrochemical measurements were carried out using a Solartron analytical potentiostat/galvanostat 1400 cell test system in a small undivided beaker cell (volume 50 cm^3). As prepared nickel alloy electrode (working electrode), large area platinum gauze (counter electrode) and Hg/HgO reference electrode in 1 M NaOH were used for the study. The area of the electrode was 9 cm^2 and 30 % KOH solution to which CA between 0 and 1 wt. % has been added was used as the electrolyte. Figure 1 shows the cell set up used for testing of the electrodes of the present study.

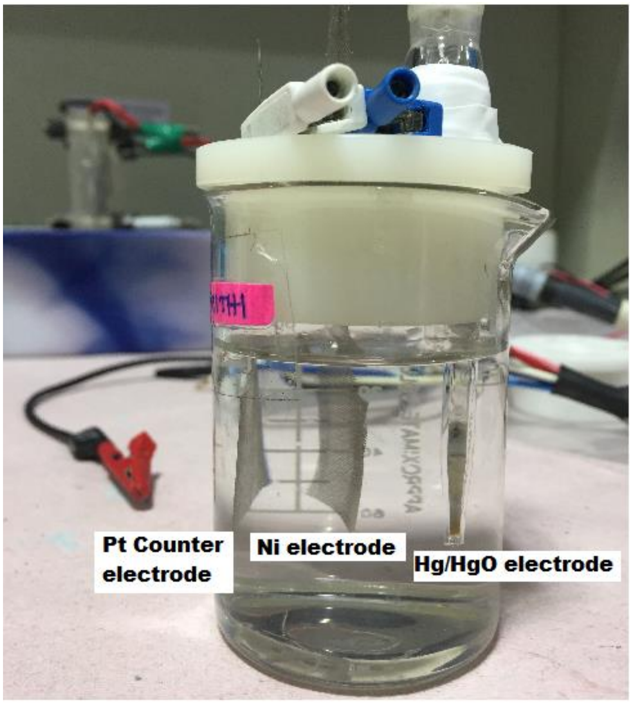

Figure 1. *Three electrode cell set up used for electrochemical characterization*

4. Electrode characterization

The surface morphology of the electrodes was studied using Hitachi SU1500 Scanning Electron Microscopy (SEM). Energy dispersive analysis of X-ray (EDAX) using Hitachi 4300 was used to study the composition of metals on the electrode. Rigakuminiflex X-Ray diffraction (XRD) with CuK$_\alpha$

(λ- 0.154 nm) radiation was used for X-ray characterization of the electrodeposits. Perkin-Elmer system was used to obtain the Fourier Transform Infrared spectra (FT-IR).

Results and discussion

1. FT-IR analysis

Figure 2 shows FT-IR spectra of the nickel electrode with and without the addition of stabilizer. The bands due carboxyl groups of citric acid are present between 1800 and 1300 cm^{-1}. The band at 1721 cm^{-1} has been ascribed to free COO$^-$ group. The band at 1630 cm^{-1} has been ascribed to the carboxylic group forming intramolecular hydrogen bonds. The band at 1425 cm^{-1} may be assigned to the bidentate carboxylate anion. For nickel alloy electrode in citric acid spectra, the band around 3450 cm^{-1} was very broad, due to hydration by water molecule indicating the electrolytes ability to wet the electrode. In spectra without citric acid due to less adsorbed water molecule this peak was small. The bands around 1150 and 650 cm^{-1} represent the stretching vibrations of the nickel sulphate used for electroplating of nickel [12]. These studies confirm the formation of nickel citrate complex on dipping the electrode in the electrolyte containing CA. Literature studies have shown that upon immersion of a nickel electrode into the solution of aqueous alkali, a film of Ni(II) oxide species (α-$Ni(OH)_2$) is formed spontaneously [20]. This on ageing dehydrates and gets converted into β–$Ni(OH)_2$. The electroprecipitation of this oxide forms Ni plaques and may lead to decrease in performance. On addition of citric acid into the electrolyte Ni forms citrate complexes that may help in cleaning the surface of the oxide layer. The complexes formed may improve the wetting ability of the electrolyte by decreasing the surface tension of the electrodes.

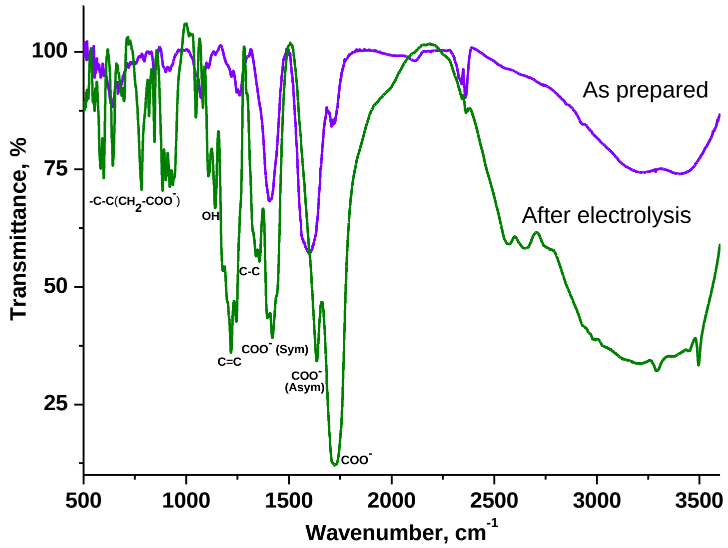

Figure 2. *FT-IR Spectra of electrolytic surface: (a) before and* ***(b)*** *after citric acid addition*

2. Effect of variation of CA

Figure 3 shows the polarization curves with the variation in the amount of CA at 30 °C. A current density of 0.40 Acm^{-2} was achieved with 0.1 wt % addition of CA compared to 0.32 A cm^{-2} achieved without the addition of CA at 1.0 V *vs.* Hg/HgO reference electrode. The maximum current density of 0.47 A cm^{-2} was obtained on the addition of 0.2 % CA at 1.0 V. Further increase in citric acid led to decrease in current density to 0.37 A cm^{-2} at 0.3 % CA addition. In alkaline solution without CA, $Ni(OH)_2$ precipitates on the surface and gets absorbed on the electrode, passivates the electrode decreasing the kinetics of the reaction. On the addition of CA, formation of $Ni(OH)_2$ on the surface decreases and a citrate complex of Ni is formed resulting in increase of current density. An increase in CA concentration leads to a strong citrate adsorption on the surface reducing the catalytic activity. Ni citrate particles present on the surface of the electrode may also act as nucleation sites for in situ deposition of metal thereby increasing the activity.

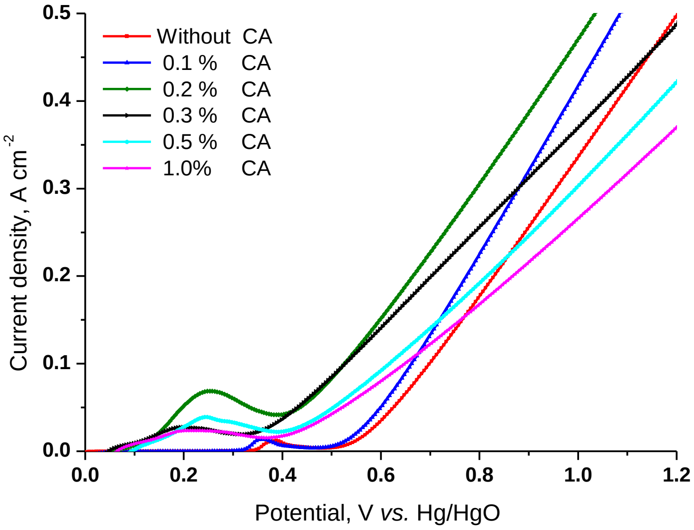

Figure 3. *Polarizations curve for alkaline water electrolysis with the different wt.% of CA at 30 °C.*

3. Cyclic voltammetry studies

Cyclic voltammograms obtained for the nickel alloy electrodes when scanned between 0 to 0.8 V *vs.* NHE at a scan rate of 5 mV s^{-1} in 30 % KOH solution are represented in Fig. 4. The oxide formation on surface of the nickel electrode is represented by the anodic current between the potentials of +0.37 and +0.58 V *vs.* Hg/HgO. The peak at potential of +0.16 V *vs.* Hg/HgO represents the oxide layer reduction upon current reversal. The Ni(II)- Ni(III) oxide transformations as represented by peaks acts as electrocatalyst for the OER[13,21]. Of all the additions, 0.2 wt. % of CA in 30 % potassium hydroxide solution showed the highest area.

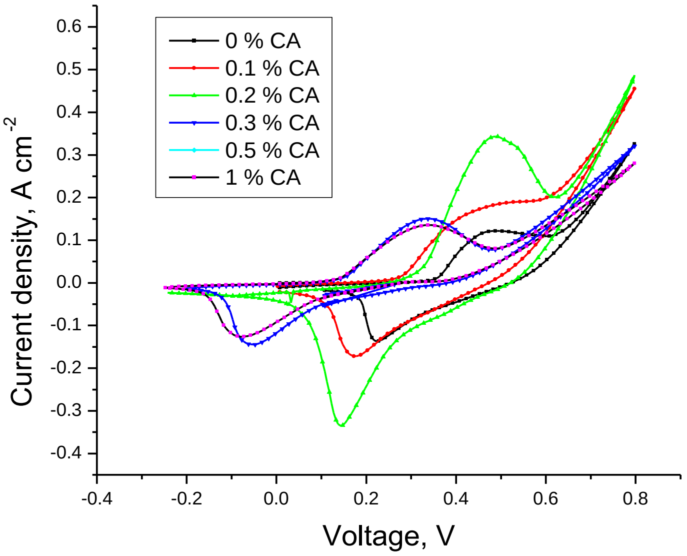

Figure 4. *Cyclic voltammograms of nickel alloy electrode with different wt.% of CA.*

The addition of 0.2 wt. % of CA enabled the current to increase more sharply when the potential reaches ~0.52 V. However, upon increasing the citric acid concentration above a 0.2 wt. % a further increase was not seen and the curve almost truncated. CA may reduce the surface tension of the electrolyte so the bubbles formed due to evolution of oxygen gas can leave the system easily. At higher concentration of CA, a strong absorption on the surface leads to decrease in catalytic sites and decrease in activity.

4. Effect of temperature

Figure 5a shows the steady state polarization curves of Ni-Zn-S alloy electrode at different temperatures on the addition of citric acid (0.2 wt. %) in alkaline water electrolysis. As can be seen from the polarization curves, performance increases with increase in temperature. A high current density of 0.78 A cm^{-2} was achieved at 1.0 V and 80 °C. With the introduction of citrate in the system, the overall efficiency increases and overvoltage also decreases for OER. The improved performance may be explained on the basis of an increase in the conductivity of the electrolyte at higher temperatures and also due to increase in catalytic activity with the increase in temperature. Figure 5b gives the long term stability of the cell, studied by holding the cell continuously at a potential of 1.0 V *vs.* Hg/HgO electrode and monitoring the current at the temperature of 30 °C. The current was constant indicating the stability of the cell with added citric acid.

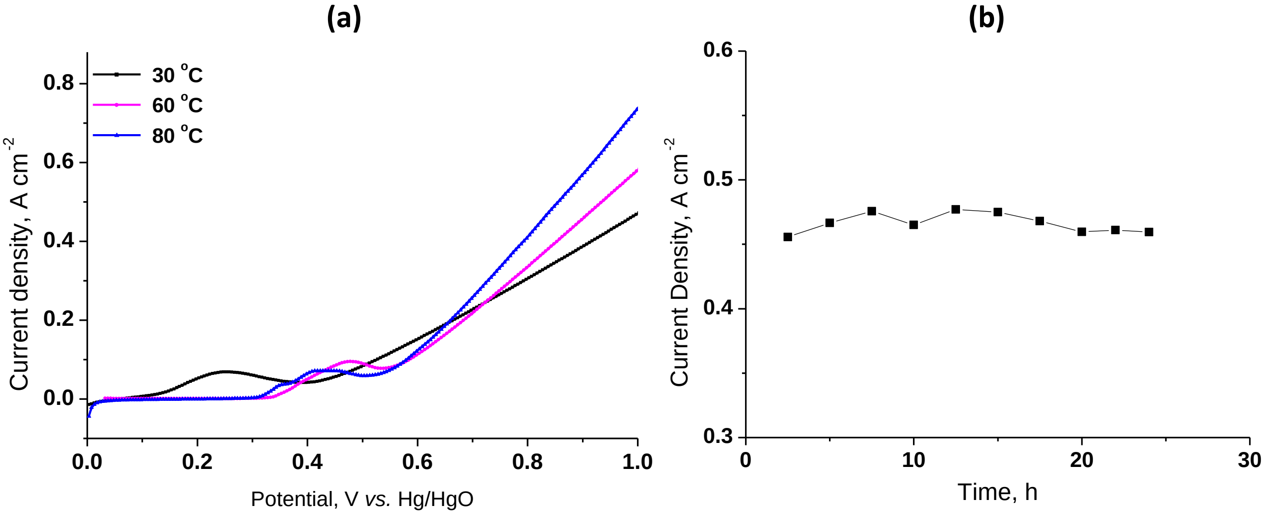

Figure 5.*Effect of temperature on the addition of CA (0.2 wt. %) in alkaline water electrolysis* ***(a)*** *and stability test with addition of CA (0.2 %) at 1.0 V* vs. *Hg/HgO at 30 °C* ***(b)***

5. SEM analysis

Scanning electron microscopy (SEM) of the nickel anode was performed before and after (24 h of continuous operation) the electrolytic process with the addition of the CA in the electrolyte. The typical SEM images are presented in Fig. 6. The morphology of deposits before electrolysis are shown in Figure 6 (a) and (b). In these micrographs homogenous globular particles are seen. The surface of the electrodes is also divided by coarser cracks and channels. The cracks are likely to be filled with the electrolyte when dipped in the solution. This increases the surface area of the catalyst in contact with the electrolyte and leads to increase in current density. Further, efficiency may also be increased due to convective replenishment of the electrolyte due to gas evolution. The EDAX data of the nickel alloy electrodes prepared has a composition of nickel (55 %), zinc (30 %) and sulphur (15 %).

The morphology of deposits after addition of the CA during the electrolytic process is shown in Fig. 6 (c) and (d). The surface of the electrodes is characterized by the presence of flakes covering the electrodeposited layers.

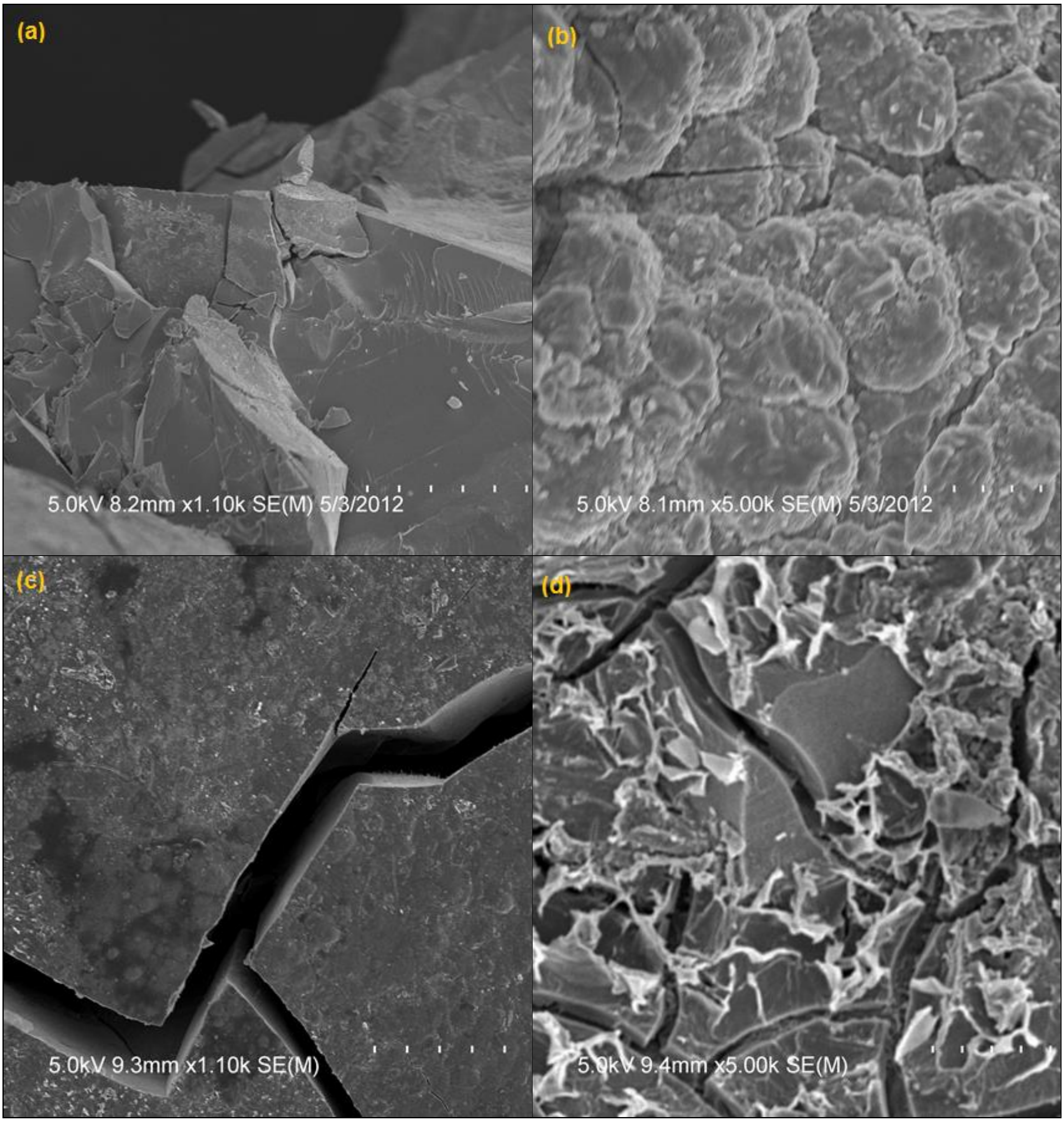

Figure 6. *SEM Images of nickel alloy electrodes:* ***(a)*** *and* ***(b)*** *after electrolysis with KOH,* ***(c)*** *and* ***(d)*** *After electrolysis with KOH and CA*

The deposits appear to be interspersed on the surface of the electrode and make the surface appear rough. Thus, it is evident that the addition of CA in the electrolyte has resulted in the deposition of Ni metal particle on the surface during the electrolytic process. Thus, an increase in surface area and an increase in possible active centers are revealed in the SEM micrographs of the sample after electrolysis. The citric acid complexing agent thus acts as a bridge for the transfer of electrolyte on the surface of the electrode and the in situ metal deposits with their high surface area and catalytic activity improve the performance of the electrode for OER. These results compare well with the powder deposits of Fe-Ni observed by use of citric acid by Lačnjavec *et al.* [22] in their studies on electrodeposition of Fe-Ni from citrate electrolytes.

6. XRD analysis

Figure 7 shows the XRD patterns of electrodeposited nickel electrodes before and after (24 h of continuous operation) electrolysis. The X-ray diffraction pattern of the before electrolysis sample has a broad peak around 44° corresponding to (111) position of Ni. Due to the high concentration of nickel, the intensity of these peaks is high and hence only these are seen. The Zn and S present are detected only by the EDAX analysis. In the after electrolysis curve the intensity of the nickel peak is very high and the peak is also very sharp. The average particle size was calculated using Debye-Scherrer relation. The particle size of samples after and before electrolysis was found to be between 11 and 16 nm respectively. This may be explained by the deposition of the in situ Ni particles from the Ni citrate complex formed. Such in situ deposited particles may be responsible for the increased electrochemical activity shown in the OER reaction. It shows that the size of Ni deposit particles can be modified by the addition of citric acid. Similar observations of metal deposition have been reported from the solution by Nikolić *et al.*[14].

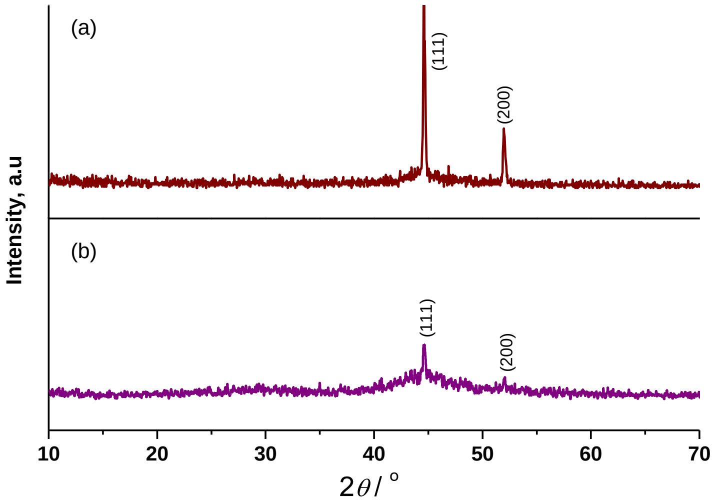

Figure 7. *XRD patterns of nickel surface: (a) after electrolysis; (b) before electrolysis*

The addition of 0.2 wt. % citric acid to the standard electrolyte as a complexing agent thus decreases the energy consumption during electrolysis of water. The addition resulted in the in situ deposition of Ni on the surface (as shown in SEM figures). The improved performance suggests that an extremely active surface center is created to improve the catalytic activity of the electrode. Further the formation of the nickel citrate complex may improve the wettability of the electrode and may act as a bridge for ion transfer between the electrolyte and the metal surface [23].

Conclusions

The results presented help in concluding that a deposit formed in-situ during the electrolytic process by using a complexing agent such as CA in the electrolytic solution is extremely active. An increase in the current density of about 25 % resulted at a temperature of 30 °C in the presence of 0.2 wt. % of CA at 1.0 V *vs.* Hg/HgO. The CA distributed throughout the nickel matrix as a complex created more organized transfer channels to produce high surface area electrodes for alkaline water electrolysis. SEM and XRD figures obtained after electrolysis confirm the deposition of the metal. This form of deposit is very active and improves the catalytic activity of the electrode. Improvement may also be explained due to increase in wettability and the bridging ability of the complexing agent to transfer ions between the electrolyte and metal surfaces. Thus, through simple processing, high current density and good efficiency can be obtained. We believe this type of complexing agent deserves further investigation and is a good candidate for use in alkaline water electrolysis.

Acknowledgement: *The authors would like to thank Director, ARCI for his constant encouragement and support and Department of Science and Technology (DST), Government of India for financial assistance. S. Seetharaman thanks ARCI for the Senior ARCI fellowship under which this work was carried out.*

References

[1] E. Rasten, G. Hagen, R. Tunold, *Electrochim. Acta* **48** (2003) 3945-3952
[2] P. Millet, D. Dragoe, S. Grigoriev, V. Fateev, C. Etievant, *Int. J. Hydrogen Energ.* **34** (2009) 4974-4982
[3] S. P. S. Badwal, S. Giddey, F. T. Ciacchi, *Ionics* **12**(2006)7-14
[4] J. Panek, A. Budniok, *Surf. Interface Anal.***40** (2008) 237-241
[5] A. A. Kamnev, B. B. Ezhov, V. Rusanov, V. Angelov, *Surf. Interface Anal.* **19**(1992) 577-580
[6] P. W. T. Lu, S. Srinivasan, *J. Electrochem. Soc.* **125** (1978) 1416-1422
[7] G. Zhang, Y. Qiu, X. Yang, X. X. Li, H. Pan, *Desalin. Water Treat.* **56** (2015) 905-911
[8] G. Sheela, M. Pushpavanam, S. Pushpavanam, *Int. J. Hydrogen Energ.* **27** (2002) 627-633
[9] M. S. Sadovnikova, V. M. Belikov, *Russ. Chem. Rev.* **47** (1978) 199-212
[10] B. H. Chen, L. Hong, Y. Ma, T. M. Ko, *Ind. Eng. Chem. Res.* **41** (2002) 2668-2678
[11] V. C. Kieling*, Surf. Coat. Tech.* **96** (1997) 135–139
[12] Q. Mao, L. Zhang, D. Huang , D. Wang, Y. Huang, H. Xu, H. Cao, Z. Mao, *Surf. Interface Anal.* **43** (2011) 903-912
[13] I. G. Casella, M. Gatta, *J. Electroanal. Chem.* **534** (2002) 31–38
[14] V. M. Nikolić, G. S. Tasić, A. D. Maksić, D. P.Šaponjić, S. M. Miulović, M. P. M. Kaninshi, *Int. J. Hydrogen Energ.* **35** (2010) 12369-12373
[15] M. P. M. Kaninski, A. D. Maksić, D. L. Stojić, S. C. Miljanić, *J. Power Sour.* **131** (2004)107-111
[16] S. M. Miulović, S. L. Maslovera, M. M.Šeović, B. B. Raduk, M. P. M. Kaninski, *Int. J. Hydrogen Energ.* **37** (2012) 16770-71675
[17] E. Gomez, S. Pane, E. Valles, *Electrochim. Acta* **51**(2005) 146-153
[18] A. Afshat, A. G. Dolati, M. Ghorbani, *Mater. Chem. Phys*. **77** (2003) 352-358
[19] S. Seetharaman, R. Balaji, K. Ramya, K. S. Dhathathreyan, M. Velan, *Ionics* **20** (2014) 713-720
[20] A. Seghiover, J. Chevalet, A. Barhoun, F. Lantelme*, J. Electroanal. Chem.* **442**(1998)113-123.
[21] M. C. Biesinger, B. P. Payne, L. W. M. Lau, A. Gerson, R. S. C. Smart, *Surf. Interface Anal.* **41** (2009) 324-332
[22] U. Lačnjevac, B. M. Jović, V. D. Jović, *Electrochim. Acta* **55** (2009) 535-543
[23] O. Gyliene, J. Aikaite, O. Nivinskiene, *J. Hazard. Mater.* **109** (2004) 105-111.

J. Electrochem. Sci. Eng. **6(3)** (2016) 225-234; doi: **10.5599/jese.289**

Open Access : : ISSN 1847-9286
www.jESE-online.org

Original scientific paper

Cyclic voltammetric study of tin hexacyanoferrate for aqueous battery applications

Denys Gromadskyi✉, Volodymyr Chervoniuk, Sviatoslav Kirillov

Joint Department of Electrochemical Energy Systems, 38A Vernadsky Ave, 03680 Kyiv, Ukraine

✉Corresponding author: d.gromadskyi@gmail.com; Tel.: +380 93 672 6654

Received: April 28, 2016; Revised: June 30, 2016; Accepted: July 7, 2016

Abstract

A hybrid composite containing 65 mass % of tin hexacyanoferrate mixed with 35 mass % of carbon nanotubes has been synthesized and its electrochemical behavior as a negative electrode in alkali metal-ion batteries has been studied in 1 mol L^{-1} aqueous solution of sodium sulfate. The specific capacity of pure tin hexacyanoferrate is 58 mAh g^{-1}, whereas the specific capacity normalized per total electrode mass of the composite studied reaches 34 mAh g^{-1}. The estimated maximal specific power of an aqueous alkali-metal ion battery with a tin hexacyanoferrate electrode is ca. 3.6 kW kg^{-1} being comparable to characteristics of industrial electric double-layer capacitors. The maximal specific energy accumulated by this battery may reach 25.6 Wh kg^{-1} at least three times exceeding the specific energy for supercapacitors.

Keywords
Aqueous alkali-metal-ion battery; Tin hexacyanoferrate-based composite

---

Introduction

Nowadays, the list of electrochemical energy storage devices is quite wide, from electric double-layer capacitors (the so-called supercapacitors) to various rechargeable batteries (lead-acid, lithium-ion and others). Their specific energy and power characteristics significantly vary depending on electrode materials, electrolyte compositions, *etc.* Supercapacitors demonstrate very high specific power values (up to 6 kW kg^{-1} at 95 % efficiency) but their specific energy is immeasurably low compared to any commercially available battery (1–8 Wh kg^{-1} vs. 26–170 Wh kg^{-1}) [1,2].

In recent years, alkali metal-ion batteries, supercapacitors and their hybrids with neutral aqueous electrolytes gain popularity due to their relatively low cost, fire safety and environmental friendliness as opposed to devices with nonaqueous organic solutions which decompose under applied voltage at the presence of a small amount of water impurity and, inter alia, may provoke the corrosion of metallic cell components [3–7]. As electrode materials for the aqueous rechargeable batteries, multivalent metal complexes (*e.g.* barium, cobalt, copper, iron, manganese, nickel, titanium and zinc hexacyanoferrates) [8–15] are commonly utilized. All these compounds having a perovskite-like structure similar to the Prussian blue ($A_xM_y[Fe(CN)_6)$, where A is an alkali metal and M is a multivalent metal) are good hosts for alkali and alkaline earth ions [16]. Their electrochemical properties arise from the process of alkali metal ion intercalation/deintercalation [17]:

$$M_y[Fe(CN)_6] + xA^+ + xe^- \leftrightarrow A_xM_y[Fe(CN)_6] \qquad (1)$$

Hexacyanoferrate anion is relatively low-toxic (LD_{50} oral-rat is 1600 mg kg^{-1}) [18] because it does not tend to release free cyanide, and the total toxicity of a salt should be defined by the harmfulness of the multivalent metal. If the data on lethal doses (LD_{50}, oral-rat) and prices for raw materials used for the synthesis of hexacyanoferrates (mainly nitrates and chlorides of reagent grade or p.a. quality) are compared, Table 1, one can see that tin chloride has a low value of LD_{50} and is quite inexpensive [18,19]. This makes tin hexacyanoferrate (SnHCF) an interesting candidate for electrochemical studies. Its theoretical specific capacity $Q_{\text{sp.(theor.)}}$ in the case of insertion/deinsertion of sodium ion,

$$Sn_{1.5}[Fe^{III}(CN)_6] + Na^+ + e^- \leftrightarrow NaSn_{1.5}[Fe^{II}(CN)_6] \qquad (2)$$

calculated as

$$Q_{\text{sp.(theor.)}} = \frac{nF}{M} \qquad (3)$$

equals to 64.9 mAh g^{-1}. In Eq. (3), n is the number of electrons taking part in the electrode half-reaction, F = 26801 mAh mol^{-1} is the Faraday constant, and M is the molecular mass of $NaSn_{1.5}[Fe(CN)_6]$.

Table 1 *Toxicity and cost of some multivalent metal chlorides and nitrates.*

	Chlorides						
	$BaCl_2$	$CoCl_2$	$CuCl_2$	$MnCl_2$	$NiCl_2$	$SnCl_2$	$ZnCl_2$
LD_{50}, mg kg^{-1}	118	80	584	1484	105	700	350
Price, € kg^{-1}	45	1272	174	199	904	148	122
	Nitrates						
	$Ba(NO_3)_2$	$Co(NO_3)_2$	$Cu(NO_3)_2$	$Mn(NO_3)_2$	$Ni(NO_3)_2$	$Sn(NO_3)_2$	$Zn(NO_3)_2$
LD_{50}, mg kg^{-1}	355	691	794	300	1620	N/A	1190
Price, € kg^{-1}	122	458	300	100	1590	N/A	38

Despite of the large number of publications referred to hexacyanoferrate-based batteries no research works exist directed towards the use of SnHCF in energy storage applications, although it serves as a material for electrochemical sensors [20]. This paper aims at filling this gap, i.e. at exploring potentialities of a SnHCF based composite as an electrode material for aqueous alkali-ion batteries.

Experimental

1. Composite synthesis

A composite containing SnHCF and multi-walled carbon nanotubes (CNTs) as a conductive additive was synthesized via room-temperature precipitation technique according to the following equation,

$$3SnCl_2 + 2K_3[Fe(CN)_6] = 2Sn_{1.5}[Fe(CN)_6] + 6KCl \tag{4}$$

FloTube^{TM} 9000 CNTs from C-Nano were treated in nitric-sulfuric acid mixture as proposed in Ref. [21], dispersed in water, and then homogenized by a mechanical stirrer for 15 min. Tin chloride dihydrate (reagent grade, ReaKhim) was added into the reaction vessel and mixed together for next 15 min. After that, the 0.3 mol L^{-1} solution of potassium hexacyanoferrate (reagent grade, ReaKhim) was added dropwise to avoid fast precipitation and coagulation of SnHCF particles. A SnHCF-CNT suspension was stirred for 1 h, filtered, washed with deionized water to neutral pH and dried at 80 °C for 12 h. It should be noted that the amount of CNTs in the SnHCF/CNT composite was varied from 20 to 80 mass %.

2. Electrode preparation and characterization

In order to prepare the electrodes a SnHCF/CNT composite was homogenized in ethanol where polytetrafluoroethylene (60 mass % dispersion in water, Sigma Aldrich) as a binding agent was added in advance. The mass ratio of the SnHCF/CNT composite and the polytetrafluoroethylene binder was 9 to 1. Pre-electrode slurries were formed by manual mixing in a mortar and alcohol evaporation. Ready-to-use electrodes were obtained after densification by rolling and drying at 80 °C for 12 h. Their porosity analysis was performed at 77 K by means of Quantachrome® Autosorb Station 3.

3. Cell assembling and electrochemical testing

Electrochemical measurements were carried out in a flat three-electrode cell by means of cyclic voltammetric technique on a home-made potentiostat at room temperature. The working electrode was the SnHCF/CNT composite with binding agent (mass 2 mg, geometric surface area 0.09 cm^2). The counter electrode with the geometric surface area of 0.5 cm^2 was made of a commercial activated carbon (Kuraray YP50F). These electrodes were separated by two layers of a porous paper membrane (TF4030, Nippon Kodoshi), and a silver sulfate reference electrode fabricated as described in Ref. [22] was located between them. Its potential was +0.137 V vs. Ag/AgCl at 25 °C. After assembling, the cell was impregnated by an electrolyte, 1 mol L^{-1} Na_2SO_4 aqueous solution.

Cyclic voltammetric testing is suitable for determining key characteristics of any energy storage material, namely its operation potential range, reversibility of charge/discharge processes as well as specific capacity [23]. The latter was calculated as

$$Q_{\text{sp.}} = \frac{I\Delta U}{3.6\times vm} \tag{5}$$

where $Q_{\text{sp.}}$ is the specific capacity (mAh g^{-1}), I is the current (A), ΔU is the operating potential range (V), v is the scan rate (V s^{-1}) and m is the electrode mass.

Results and discussion

The electrochemical behavior of SnHCF-based electrodes depending on the CNT content is shown in Fig. 1. Cyclic voltammograms (CVs) demonstrate cathodic and anodic peaks characteristic of electrodes where reversible or quasi-reversible electrochemical reactions take place. Adding CNTs leads to changing the profile of CV making it typical for electrodes with electric double-layer capacitance.

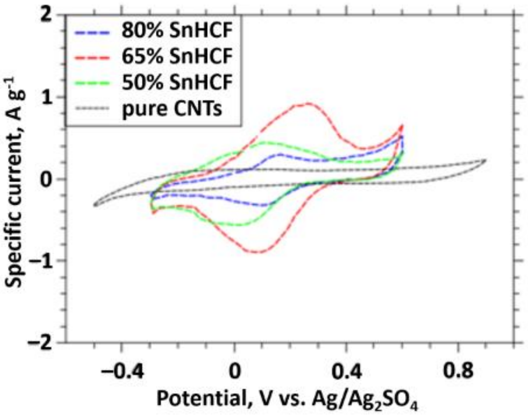

Fig. 1. *CVs of SnHCF-based electrodes containing different amount of CNTs recorded at 5 mV s^{-1}.*

The heights of the peaks responsible for the intercalation/deintercalation of Na^+ ion into/from the SnHCF structure are different. This means that respective specific capacities are also different and, moreover, non-linearly vary with the SnHCF/CNT ratio. Upon growing the amount of CNTs the specific capacity increases rapidly reaching a maximal value (~45 mAh g^{-1}) at 35 mass % of CNTs and then decreases. Such behavior presumably reflects the contribution of CNTs to the structure formation of the composites. CNTs not only play the role of a conductive additive; they create a structured framework facilitating the access of ions to electroactive hexacyanoferrate species deposited in mesopores with pore radii greater than 12 nm. This is seen from Fig. 2(a) where pore size distributions calculated according to the density functional theory (DFT) is shown. Besides, SnHCF-based composites have a slightly higher volume V of micropores of about 1 nm radii r than CNTs possibly due to oxidizing the CNT surface by potassium hexacyanoferrate. Similar behavior is observable in Fig. 2(b) for pore size distributions obtained by the Barrett-Joyner-Halenda (BJH) method, which is less sensitive to microporosity being better suitable for mesoporous materials.

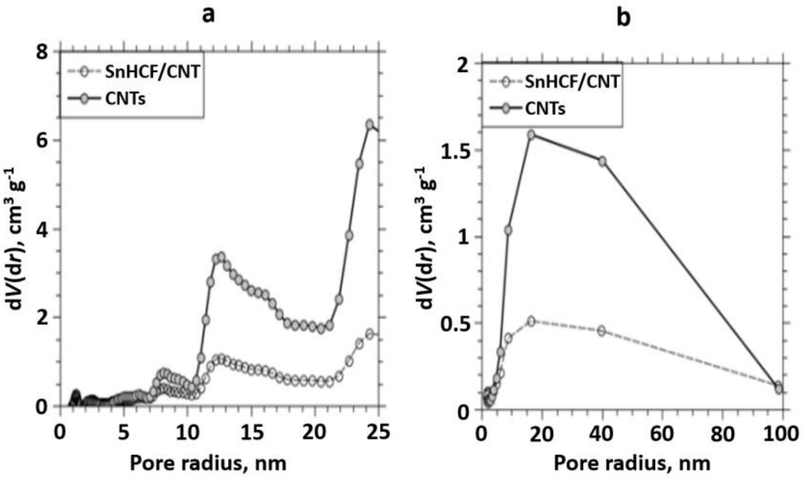

Fig. 2. (a) *Pore size distributions for SnHCF electrode with 35 mass % CNT and pure CNT electrode calculated by means of* ***(a)*** *DFT and* ***(b)*** *BJH techniques.*

As the SnHCF-based material containing 35 mass % of CNTs demonstrates the best electrochemical performance, all following experiments were conducted with it. It should be also mentioned that in performance estimates, some authors account only for the mass of the electroactive material and ignore the masses of a conductive additive and a binder [24–26]. In this work, we prefer to operate with the mass of the electrode as a whole since just this value is of practical importance. The specific capacity of the electrode material without the contribution of CNTs and polytetrafluoroethylene can be calculated via division by 0.585 in accord with the mass ratio of electrode components (see Subsections 1 and 2 in Experimental). This gives $Q_{\mathrm{sp.}}$ of about 77 mAh g^{-1}, while the specific capacity[1] of other insoluble hexacyanoferrates in aqueous electrolytes varies from 36 to 59 mAh g^{-1} for individual compounds [10,15,26]. The $Q_{\mathrm{sp.}}$ value obtained is 12 % higher than the theoretical one (64.9 mAh g^{-1}), probably due to the impact of unwanted faradaic side processes (e.g. the decomposition of electrode and/or electrolyte components). Due to this fact in what follows we confined ourselves with a narrower potential range (-0.25...+0.50 V).

The CV curves demonstrate a significant dependence on the scan rate, Fig. 3(a), and respective peak heights linearly vary with the square root of the scan rate, Fig. 3(b). This indicates the diffusion control of the Na$^+$ intercalation/deintercalation upon the charge/discharge of the SnHCF-based electrode. An analysis of the CV for the SnHCF-based electrode at the slowest scan rate (5 mV s^{-1}) shown in Fig. 4 gives the peak height ratio I_a/I_c of almost unity characterizing the electrochemical process as a reversible one in spite of the deviation of the peak shift U_a/U_c from the theoretical value of 59 mV that may be caused by interactions between intercalated species as proposed by Laviron [28].

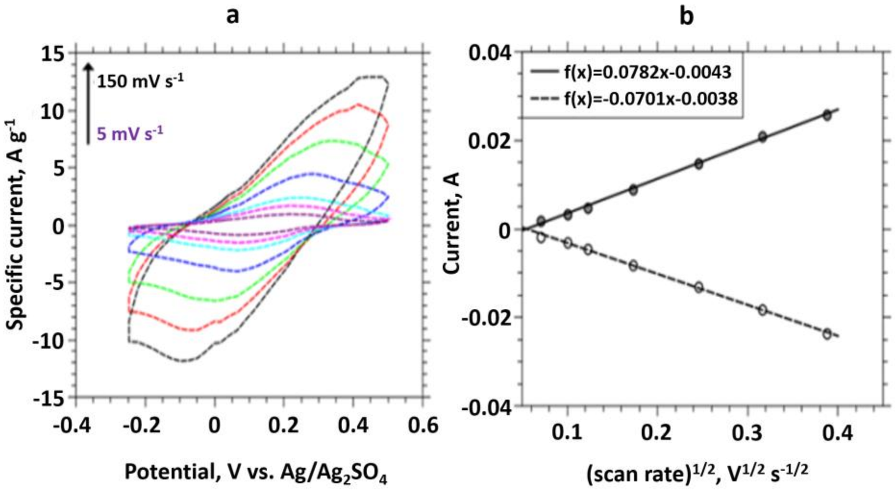

Fig. 3 (a) *CVs of SnHCF-based electrode recorded at different scan rates, and* ***(b)*** *dependence of anodic (filled circles) and cathodic (empty circles) peak current on the square root of scan rate for this electrode.*

Diffusion coefficients D for Na$^+$ cation have been determined via the Randles-Ševčik equation [29]

$$I_{\mathrm{p}} = 2.69\times 10^5 n^{3/2} A D^{1/2} C v^{1/2} \qquad (6)$$

where I_{p} is the anodic or cathodic peak current (A), n is the number of electrons taking part in the electrode half-reaction; A is the geometric surface area of the electrode (cm^2), C is the concentration of Na$^+$ ions in the electrolyte solution (mol cm^{-3}); v is the scan rate (V s^{-1}). They are 2.1·10^{-6} cm^2 s^{-1} and 2.6·10^{-6} cm^2 s^{-1} for the intercalation and deintercalation processes, respectively.

---

[1] In some articles authors consider insoluble hexacyanoferrates, which are typical battery-type materials, as supercapacitor-type ones. Consequently, they characterize them by specific capacitances instead of specific capacities that is fundamentally flawed as described in Ref. [27]. Therefore, in order to compare our data with results obtained by other researchers we transfer the specific capacitance into the specific capacity through its multiplication by operating potential range and division by 3.6.

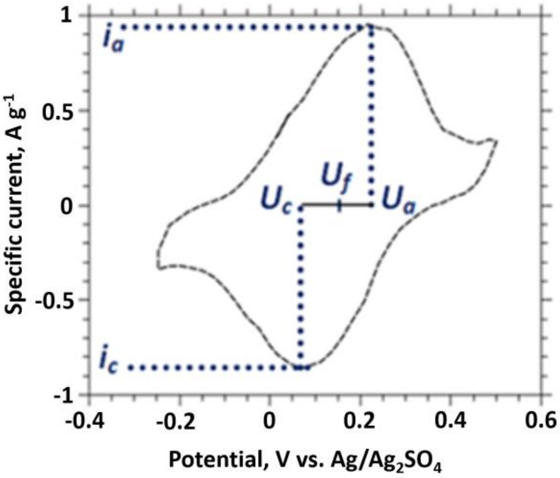

Fig. 4. *CV of SnHCF-based electrode recorded at 5 mV s^{-1}*

The *D* values obtained are significantly higher than diffusion coefficients in transition metal oxides commonly employed as electrodes in 'traditional' lithium-ion batteries, being rather comparable with effective diffusion coefficients obtained in supercapacitor electrodes produced from commercial activated carbons [30–33]. Such behavior can be explained by an effect of CNTs on the structure of the synthesized composite, where SnHCF particles are located in 12 nm pores formed by a CNT network. These nanosized particles are better accessible to electrolyte, and all advantages of finely subdivided electrode materials [34] are applicable to them.

The maximal specific capacity of the composite electrode (34 mAh g^{-1}) is observed at 5 mV s^{-1}, Fig. 5. Using a 0.585 factor as described above, the capacity related to the mass of neat SnHCF is determined as 58 mAh·g^{-1} thus representing 89 % of the theoretical value.

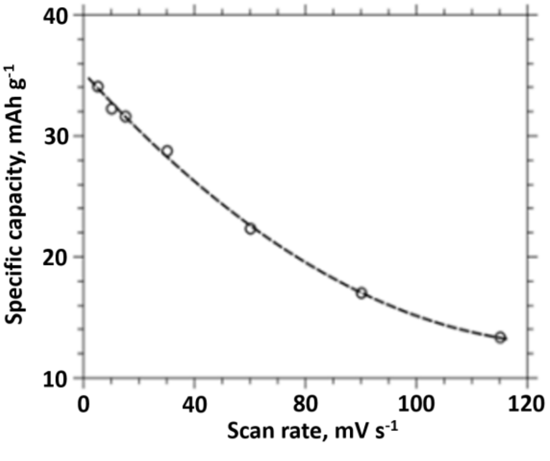

Fig. 5. *Dependence of specific capacity of SnHCF-based electrode on the scan rate*

Another important requirement for energy storage devices in addition to high specific capacity is their charge/discharge cycling stability. According to data shown in Fig. 6 the SnHCF-based electrode demonstrates an excellent cycling behavior. No capacity decrease is observed after 500 charge/discharge cycles. Furthermore, $Q_{\mathrm{sp.}}$ even increases a little (by ~5 %) at the first cycles, possibly due to deeper ion intercalation into the hexacyanoferrate structure (pretreatment), and becomes stable reaching the value of 23 mAh g^{-1}. This is confirmed by changes in the anodic and cathodic peak heights collected in Table 2, which are leveling on growing the cycle number. The insignificant drift of the formal potential on cycling (10^{-5} V cycle^{-1}) should also be considered as an additional verification of the good reversibility of the electrochemical system studied. Furthermore, it is asserted [35] that the constancy of the formal potential signifies right mass balancing of the negative and positive electrodes in the cell.

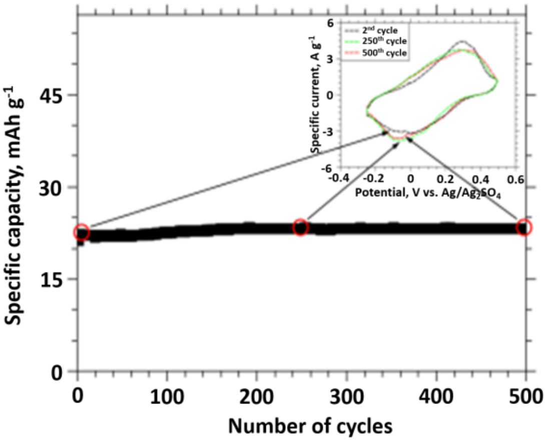

Fig. 6. *Changes in the specific capacity of SnHCF-based electrode during voltammetric cycling at 50 mV s^{-1}*

Table 2. *CV parameters of SnHCF-based electrode obtained from cyclic voltammograms given in Fig. 6.*

Cycle number	i_a, A g^{-1}	I_c, A g^{-1}	I_a/I_c	U_a, V	U_c, V	U_f, V	$Q_{sp.}$, mAh g^{-1}
2	4.43	3.19	1.39	0.28	0.0024	0.141	22.0
250	3.68	3.80	0.97	0.29	-0.0050	0.143	23.3
500	3.70	3.80	0.97	0.30	-0.0075	0.146	23.3

Using the data from Fig. 5 recalculated into the specific energy $E_{sp.}$ and power $P_{sp.}$ by means of Eqs. 7 and 8, one can build the so-called Ragone plot (Fig. 7), which helps to better understand the application field of the synthesized composite [36],

$$E_{sp.} = Q_{sp.}\Delta U \tag{7}$$

$$P_{sp.} = \frac{E_{sp.}}{\tau} \tag{8}$$

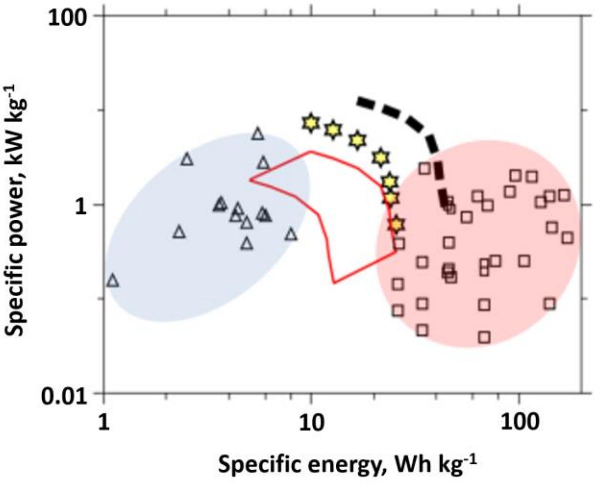

Fig. 7. *Ragone plot for pure SnHCF (dashed line), SnHCF-based electrode (stars), and a 'virtual' aqueous alkali metal-ion battery with SnHCF-based electrode (an area within the red polygon) in comparison with industrial supercapacitors (triangles limited by a blue colored area) and various rechargeable batteries (squares limited by a pink colored area) [1,2].*

In Eq. (8), τ is the time of charging or discharging the electrode in h.

In Fig. 7 we also plot the data on specific power and energy recalculated per mass of the pure electroactive material as well as per the total mass of a battery with the SnHCF-based composite as a negative electrode and additional cell elements (our approach to this calculation is given in footnote[2]). This clearly demonstrates how the characteristics are changing depending on the way of their presentation (material, electrode or device). As has been already mentioned, 'the truest' data are those normalized per electrode mass. Despite of fundamental differences in the charge storage mechanism (intercalation/deintercalation instead of adsorption/desorption), the SnHCF-based electrodes and hence energy accumulating devices with such electrodes demonstrate the specific power comparable with electric double-layer capacitors, and their specific energy values are close to lead-acid batteries. For instance, such composite electrodes can be charged up to half-capacity in a fast mode (by 7.5 seconds) with specific power of 6.1 kW kg^{-1}, while in order to charge them fully (up to 25.6 Wh kg^{-1}), less than 3 min is needed. We expect that a battery pack with SnHCF/CNT electrodes will be able to achieve the specific power and energy of (1.8–3.6) kW kg^{-1} and (12.8–25.6) Wh kg^{-1}, respectively.

The formal potentials of some multivalent metal hexacyanoferrates taken from literature sources [40–50] are collected in Fig. 8 where they are contingently divided into two groups representing negative and positive electrodes. The relatively low formal potential U_f of the SnHCF-based electrode determined as $U_f = (U_a+U_b)/2$ (+0.143 V *vs.* Ag/Ag_2SO_4 or ca. +0.28 V *vs.* Ag/AgCl) signifies an opportunity of employing the synthesized composite as a negative electrode (anode) for aqueous alkali metal-ion batteries. The best counter electrode for SnHCF that allows for getting a maximal operating voltage for a battery is VHCF and InHCF, but the extra-high cost of vanadium and indium raw materials makes CuHCF preferable for large-scale manufacturing [19]. Our further efforts will be directed towards both cathode and anode HCF materials. SnHCF-based composites mixed with other multivalent metal hexacyanoferrates (e.g. FeHCF and/or TiHCF due to their low U_f values) would be of great interest as such mixtures have been shown to have much higher specific capacity compared to the individual components [25,51].

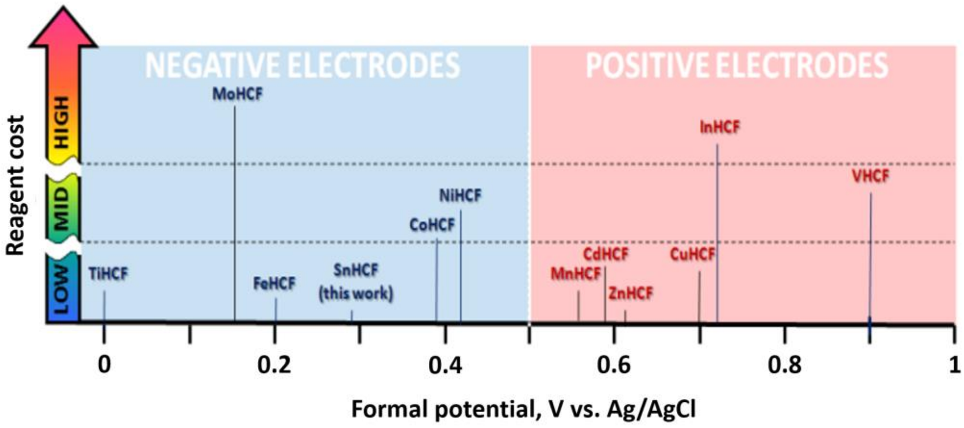

Fig. 8 *Formal potential of SnHCF-based electrode compared with formal potentials of other hexacyanoferrates in the Ag/AgCl scale.*

---

[2] Following to this approach the specific power of a single SnHCF-based electrode should be doubled if compared to the specific power of a two-electrode cell, whereas the specific energy remains almost unchanged in the case if the cell is assembled in an anode-limited design and both (negatively and positively charged) electrodes have the same working potential ranges *vs.* a nominal zero point [37]. Further, in our calculations, we account for the mass of the whole cell, since according to Refs. [38,39], the mass contribution of two electrodes to the total value of specific energy is of about 25–50 %.

Conclusions

A novel SnHCF-CNT composite has been fabricated by means of a room-temperature precipitation technique. The specific capacity of this electrode determined via cyclic voltammetry reaches 34 mAh g^{-1} at the slowest scan rate. Excellent electrochemical stability during charge/discharge cycling as well as fast ionic diffusion ($D \approx 2 \cdot 10^{-6}$ cm^2 s^{-1}) makes the synthesized SnHCF/CNT composite an attractive electrode material for low-cost and environmental friendly aqueous alkali metal-ion batteries, which can compete with supercapacitors in high-power applications.

References

[1] A. Burke, *Proc. IEEE* **95(4)** (2007) 806–820.

[2] A. Burke, *Int. J. Energy Res.* **34** (2010) 133–151.

[3] H. Kim, J. Hong, K. Y. Park, H. Kim, S. W. Kim, K. Kang, *Chem. Rev.* **114(23)** (2014) 11788–11827.

[4] A. J. Stevenson, D. G. Gromadskyi, D. Hu, J. Chae, L. Guan, L. Yu L, G. Z. Chen, *Supercapattery with hybrids of redox active polymers and nanostructured carbons*, in: X.L. Feng (Ed.), *Nanocarbons for Advanced Energy Storage*, Wiley-VCH, Weinheim, Germany, 2015, pp. 179–210.

[5] D. G. Gromadskyi, J. H. Chae, S. A. Norman, G. Z. Chen, *Appl. Energy* **159** (2015) 39–50.

[6] D. H. Hromadśkyi, Y. F. Fateev, N. H. Stryzhakova, Y. A. Maletin, *Mater. Sci.* **46**(3) (2010) 412–417.

[7] D. G. Gromadskyi, Y. F. Fateev, Y. A. Maletin, *Corros. Sci*. **69** (2013) 191–196.

[8] P. Padigi, G. Goncher, D. Evans, R. Solanki, Potassium barium hexacyanoferrate – a potential cathode material for rechargeable calcium ion batteries, J. Power Sources **273** (2015) 460–464.

[9] F. Zhao, Y. Wang, X. Xu, Y. Liu, R. Song, G. Lu, Y. Li, *ACS Appl. Mater. Interfaces* **6(14)** (2014) 11007–11012.

[10] C. D. Wessells, R. A. Huggins, Y. Cui, *Nat. Commun*. **2** (2011) Article No. 550.

[11] Y. You, X. Yu, Y. Yin, K.W. Nam, Y.G. Guo, *Nano Res*. **8(1)** (2015) 117–128.

[12] L. Wang, Y. Lu, J. Liu, M. Xu, J. Cheng, D. Zhang, J. B. Goodenough, *Angew. Chem. Int. Ed*. **52** (2013) 1964–1967.

[13] C. D. Wessells, S. V. Peddada, R. A. Huggins, Y. Cui, *Nano Lett*. **11** (2011) 5121–5425.

[14] M. Xie, Y. Huang, M. Xu, R. Chen, X. Zhang, L. Li, *J. Power Sources* **302** (2016) 7–12.

[15] H. Lee, Y.I. Kim, J.K. Park, J.W. Choi, *Chem. Commun*. **48** (2012) 8416–8418.

[16] C. Ling, J. Chen, F. Mizuno, *J. Phys. Chem*. C. **117** (2013) 21158–21165.

[17] J. Yun, J. Pfisterer, A.S. Bandarenka, *Energy Environ. Sci*. **9** (2016) 955–961.

[18] MSDS database, URL: *http://ccinfoweb.ccohs.ca/msds/search.html* (viewed on 10.02.2016).

[19] Sigma Aldrich catalog, URL: *http://www.sigmaaldrich.com/catalog/search* (viewed on 10.02.2016).

[20] H. Razmi, A. Taghvimi, *Int. J. Electrochem. Sci.* **5** (2010) 751–762.

[21] M. S. P. Shaffer, X. Fan, A. H. Windle, *Carbon* **36(11)** (1998) 1603–1612.

[22] D. G. Gromadskyi, *J. Chem. Sci*. **128** (2016) 1011– 1017.

[23] S. Zhang, N. Pan, *Adv. Energy Mater*. **5(6)** (2015) DOI: 10.1002/aenm.201401401.

[24] J. Chen, K. Huang, S. Liu, *Electrochem. Commun*. **10** (2008) 1851–1855.

[25] Y. Yang, Y. Hao, J. Yuan, L. Niu, F. Xia, *Carbon*. **84** (2015) 174–184.

[26] Y. Yang, H. Hao, X. Wang, Q. Yan, J. Yuan, Y. Shao, L. Niu, *Electrochim. Acta* **167** (2015) 364–371.

[27] A. Laheäär, P. Przygocki, Q. Abbas, F. Béguin, *Electrochem. Commun*. **60** (2015) 21–25.

[28] E. Laviron, *J. Electroanal. Chem. Interfacial Electrochem*. **52** (1974) 395–402.

[29] P. Zanello, *Inorganic electrochemistry: theory, practice and application*, Royal Society of Chemistry, Cambridge, UK, 2003, p. 615.
[30] C. K. Park, S. B. Park, S. H. Oh, H. Jang, W. Cho, *Bull. Korean Chem. Soc*. **32** (2011) 836–840.
[31] H. Hia, L. Lu, G. Ceder, *J. Power Sources* **159** (2006) 1422–1427.
[32] S. B. Tang, M. O. Lai, L. Lu, *Mater. Chem. Phys*. **111(1)** (2008) 149–153.
[33] Y. Maletin, V. Strelko, N. Stryzhakova, S. Zelinsky, A. B. Rozhenko, D. Gromadsky, V. Volkov, S. Tychina, G. Gozhenko, D. Drobny, *Energy Environ. Res*. **3** (2013) 156–165.
[34] A. S. Aricó, P. Bruce, B. Scrosati, J.M. Tarascon, W. Schalkwijk, *Nat. Mater*. **4** (2005) 366–377.
[35] Z. G. Dai, C. Peng, J. H. Chae, G. Z. Chen, *Sci. Rep.* **5** (2015) Article No. 9854.
[36] W. G. Pell, B. E. Conway, *J. Power Sources* **63** (1996) 255–266.
[37] X. Wu, Y. Cao, X. Ai, J. Qian, H. Yang, *Electrochem. Commun.* **31** (2013) 145–148.
[38] C. Liu, Z. Yu, D. Neff, A. Zhamu, B.Z. Zhang, *Nano Lett*. **10** (2010) 4863–4868.
[39] A. Du Pasquier, J. A. Shelburne, I. Plitz, F. Badway, A. S. Gozdz, G. G. Amatucci, *Proc. 11th Int. Semin. Double Layer Capacitors and Similar Energy Storage Devices*, Deerfield Beach, USA. 2001, pp. 1–10.
[40] Z. Gao, G. Wang, P. Li. Z. Zhao, *Electrochim. Acta* **36**(1) (1991) 147–152.
[41] C. H. Luangdilok, D. J. Arent, A. B. Bocarsly, R. Wood, *Langmuir.* **8(2)** (1992) 650–657.
[42] L. M. Siperko, T. Kuwana, *Electrochim. Acta* **32(5)** (1987) 765–711.
[43] K. Itaya, K. Ataka, S. Toshima, *J. Am. Chem. Soc*. **104**(18) (1982) 4767–4772.
[44] S. Dong, Z. Jin, *Electrochim. Acta* **34**(7) (1989) 963–968.
[45] P. Wang, Z. Jing, W. Zhang, G. Zhu, *J. Solid State Electrochem*. **5**(6) (2001) 369–374.
[46] S. Dong, Z. Jin, *J. Electroanal. Chem*. **256(1)** (1988) 193–198.
[47] M. H. Pournaghi-Azar, H. Razmi-Nerbin, *J. Electroanal. Chem*. **456(1–2)** (1998) 83–90.
[48] M. Jiang, X. Zhou, Z. Zhao, *J. Electroanal. Chem*. **292(1–2)** (1990) 289–296.
[49] S. Dong, F. Li, J. *Electroanal. Chem*. **210(1)** (1986) 31–44.
[50] J. Joseph, H. Gomathi, G. P. Rao, *J. Electroanal. Chem*. **431(2)** (1997) 231–235.
[51] A. Safavi, S. H. Kazemi, H. Kazami, *Electrochim. Acta* **56** (2011) 9191–9196.

J. Electrochem. Sci. Eng. **6(3)** (2016) 235-251; doi: **10.5599/jese.300**

Open Access : : ISSN 1847-9286
www.jESE-online.org

Original scientific paper

EDTA as a corrosion inhibitor for Al in 0.5 M HCl: adsorption, thermodynamic and theoretical study

Rehab E. Azooz✉

Chemistry Department, Faculty of Science, Jazan University, 2097 Jazan, Saudi Arabia

✉Corresponding Author: re_azooz@yahoo.com; Tel.: +9966532324115

Received: May 21, 2016; Revised: June 18, 2016; Accepted: July 4, 2016

Abstract

In this study; EDTA is used in very small amount (10^{-10} M) as an inhibitor for the Al corrosion in 0.5 M HCl. Thermodynamic and adsorption parameters are calculated. The result shows that, in this range of concentrations, EDTA is chemisorbed at the Al surface, forming a stable complex with Al and give inhibition efficiency up to 89 %. For more concentration, unstable complex is formed and acceleration of corrosion occurs. The adsorption fit well to Langmuir, Temkin isotherms and El-awady model. Density functional theory (DFT) is used to study the geometrical optimizations of EDTA. From the obtained optimized structure, The highest occupied molecular orbital (E_{HOMO}), the lowest unoccupied molecular orbital (E_{LUMO} and their energy difference (ΔE), the total energy (TE), electronegativity (χ), dipole moment (μ), global hardness (η), global softness (σ), electron affinity (A), ionization potential (I), the fraction of electrons transferred (ΔN) and were determined using B3LYP/6-31G(d,p) basis set.

Keywords
EDTA; Inhibition efficiency; Adsorption isotherms; Thermodynamic parameters; Theoretical parameters

---

Introduction

The study of Al corrosion is of great importance; various industrial operations depend mainly on Al. Most investigations on the corrosion of Al have been carried out on. The development of corrosion inhibitor is a good branch based on a functional organic compound. The structure and function groups of used organic compounds are useful for obtaining a good inhibitors [1-4]. Depending upon excellent conductivity (electrically and thermally) of Al; application of Al is varied and widespread. [5]. Adsorption of inhibitor on the charged metal surface is the main process to inhibit corrosion, on this basis; multiple bond(s), an electron rich atom as, S, N or P or a ring is a main centers for the adsorption processes. In aqueous media, inhibitors are used to prevent or reduce the corrosion of metals [6–11]. It was shown that, compounds containing N or/and O atoms exhibit a good inhibiting effect. A polyprotic acid, *i.e.* Ethylenediaminetetraacetic acid (EDTA), with a lone pair of electrons in its amino groups and two carboxylic acid groups is used for complexation with the charged metal ions [6,12]. Complexation occur between (free or π) -electrons from inhibitor and the vacant d-orbital of a metal through the formation of donor–acceptor surface [6,14-16]. In the last years, EDTA has been studied to protect metals from corrosion in different environments [16–19], it was found that, different parameter affects the inhibition effect of EDTA including, the pH value, temperature, concentration, and type of the metal. Nahle [20] has found that the Sn(II)–EDTA complex increased the dissolution rate of Sn in a basic medium. Milošev *et al.* [16] have investigated the corrosion of stainless steel in physiological solutions, while, EDTA prevents the formation of a passive layer and increases the solubility of the metal. Gadiyar *et al.* [22] have discovered that EDTA inhibits the corrosion of carbon steel. However, its inhibiting effect is imperfect. Alhaji and Reda [23] have stated that EDTA is effective in decreasing the corrosion rate of copper-nickel alloy in seawater contaminated with sulfur. S. Zor *et. al.* [24] observe that, the corrosion of Al is higher in 0.1 M NaCl solution in higher concentration of EDTA, and become slower at 10^{-4}M EDTA

The molecular structure, electronic structure and reactivity of Inhibitors are determined well by quantum chemical methods [25]. A powerful framework is provided by DFT [25,26] that help in understanding a lot of chemical processes [27-31]. Concepts as, electronegativity hardness or softness *etc.* are used to describe chemical reactivity [28], are appear naturally within DFT. The local electron density/population displacements represented the inflow of a single electron is measured using Fukui function [30] and is representing the relative local softness of the electron gas. In the present study the inhibition effect of EDTA for the corrosion of Al in 0.5 M HCl has been done using both weight loss and electrochemical methods. The temperature effect and adsorption isotherms will be studied in details. Also analyzing the inhibitive properties of EDTA using DFT calculations will be done.

Experimental

Chemical and reagents

Al strips have a rectangular form (4.5×3.5×0.2 cm), with the composition 99.11 % of Al, 0.019 % of Zn, 0.036 % of Cu, 0.001 % of Mg, 0.834 % of Si and, were mechanically polished using different grades of emery sheets, washed with acetone and distilled water and dried. EDTA disodium salt (Analar grade) and HCl were obtained from Fluka AG, Switzerland. All solutions were prepared using freshly prepared bidistilled water. Stock solution of EDTA was prepared, from which all used concentrations are prepared via dilution.

Methods

Weight loss measurements

The Al samples (coupons) were weighed before immersion in 250 ml beaker containing 50 ml of the respective prepared test solutions at room temperature and desired temperatures. The setups were exposed for a period of 100 min. Corrosion reaction is quenched in concentrated HNO_3

digressed in CH_3COCH_3 washed under water, dried and weighed. A mean value triplicate experiments is reported in each case. The values of weight loss in the presence and the absence of EDTA is used to calculate efficiency at the end of definite intervals of time.

Temperatures effects

The same procedure adopted where the temperature of the study was varied, in the range (303-333 K), from at the end of each experiment. The specimens were taken out, washed both in running tap water and into distilled water. They were dried and their weights were recorded.

The loss in weight was calculated. Each experiment was duplicated to get good reproducibility. Weight loss measurement was performed in 0.5 M HCl with and without the addition of EDTA in the range (6.4 – 10.07)×10^{-10} M.

Electrochemical methods

All electrochemical experiments were recorded using a potentiostate/galvanostate (EG&G 326A, U.S.A). The potential was scanned at the scan rate 10 mV s^{-1}. All experiments were repeated to ensure reproducibility. Fresh solution was used for each experiment. The cell used is a three compartment home-made one, with a reference saturated calomel electrode (SCE), an auxiliary (Pt-foil) electrode and a working (Al) electrode with 0.4 cm^2 area exposed to corroded solution was used.

Adsorption isotherms

The adsorption of inhibitor at a metal /solution interface is the main source of inhibition effect, accordingly, the isotherms of adsorption can be determined. In order to obtain the isotherm the fractional surface coverage values (θ) as a function of inhibitor concentration must be obtained. The values of θ can be easily determined from the weight loss measurements by the ratio;

$$\theta = \frac{I.E.}{100}$$

where *IE* is inhibition efficiency obtained by a weight loss method. So, it is necessary to determine empirically which isotherm fits best to the adsorption of inhibitor on the Al surface.

Scanning electron microscopy (SEM)

After a period of 100 min, Al coupons was removed from solution, rinsed with a double distilled water, dried and observed in a Scanning Electron Microscope (JSM-T20 Electron Probe Micro-analyzer (JEOL, Tokyo, Japan)) to examine the surface morphology. The following cases were examined, to understand the morphology of the Al surface in the absence and presence of inhibitors, (i) aluminum coupon after polishing, (ii) aluminum coupon dipped in 0.5 M HCl for 100 min. at 303 K and (iii) aluminum coupon dipped in 0.5 M HCl containing 2.7×10^{-10} M of EDTA inhibitor 100 min

Quantum chemical calculations

DFT is used to obtain the complete geometrical optimizations of EDTA, with Beck's exchange functional along with nonlocal correlation functional (B3LYP) of Lee–Yang–Parr [32–34] with 6-31G* basis set in Gaussian 03 program package [35]. From the obtained optimized structure, serval quantum chemical parameters were calculated; E_{HOMO}, E_{LUMO}, ΔE_{gap}, the dipole μ and *TE*.

Results and discussion

The molecular structure of an organic compound used in the present study is given in Scheme 1.

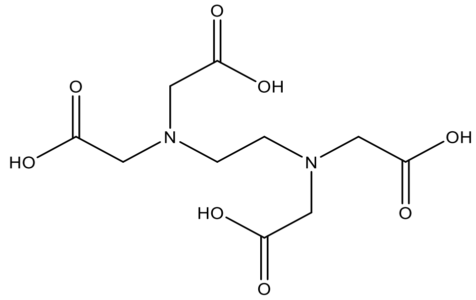

Scheme 1. *Structure of EDTA*

Open circuit potential

Potential-time curves was recorded for 60 minutes of immersion of the Al specimens in aqueous 0.5 M HCl solution without and with EDTA at required concentrations. As seen in Figure 1. From Figure 1, when Al is immersed in the HCl solution E_{OCP} drop sharply, then began to increase to more positive value and reached a stationary value after 25 minutes of immersion. The aggressiveness of the corroded solution may cause the differences in E_{OCP} values at the beginning of Al exposure, It was suggested that, adsorption of EDTA molecules on the Al surface is the reason for the initial negative shift.

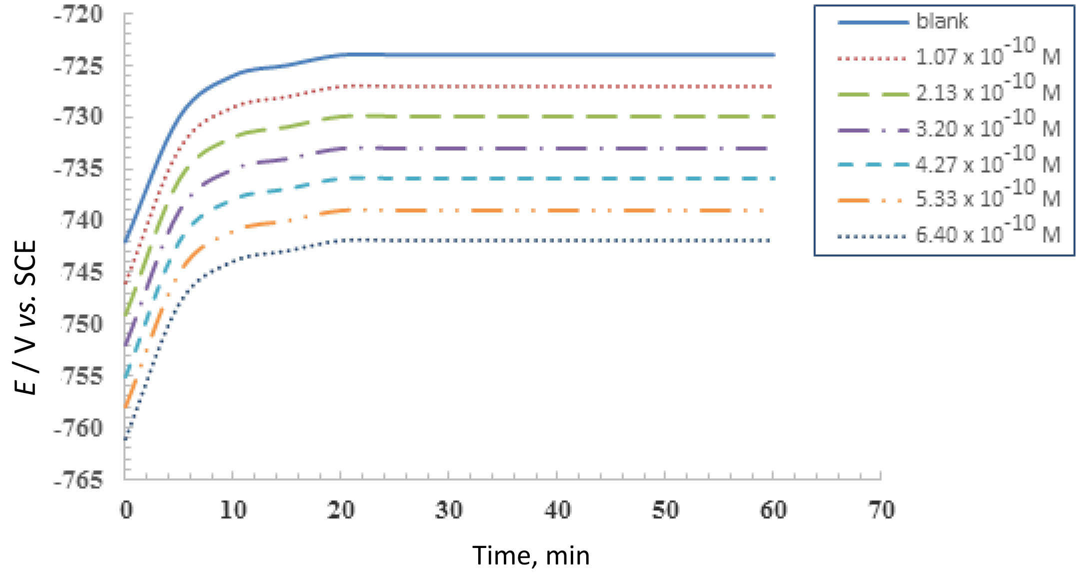

Figure 1*.Potential - time curves for Al in 0.5 M HCl in absence and presence of different concentrations of (EDTA) at 303 K.*

The results have shown that the addition of EDTA molecules at the beginning shifts E_{OCP} to more negative values. And then become more positive with time, due to oxide film growth [36]. In particular, initial values are more negative than steady state values, also the dependence of the E_{OCP} on concentration suggests that, the inhibitor molecules are strong and rapidly adsorbed at the steady state potentials [36].

Potentiodynamic polarization studies

The cathodic and anodic polarization curves of Al in 0.5 M HCl in the absence and presence of different EDTA concentrations at 303 K are shown in Fig. 2. The electrochemical kinetic parameters (in the potential range ±50 mV from E_{corr}), namely, corrosion current (i_{corr}), corrosion potential (E_{corr}), and Tafel slopes, (β_c and β_a), have been determined simultaneously and are listed in Table 1. Data infer that, the addition of EDTA to the acid solutions increases both the anodic and cathodic overpotentials, decreases the corrosion current density, i_{corr}, and shifts the E_{corr} to more positive values. This means that the presence of EDTA inhibits the partial anodic dissolution of Al and also retards the partial cathodic reduction of hydrogen ion.

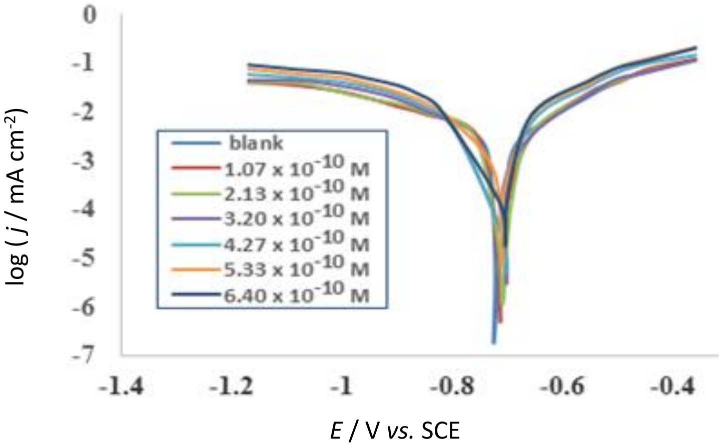

***Figure 2**. Potentiodynamic polarization curves for Al in 0.5M HCl at 303 K with scan rate of 10 mV s^{-1} with and without different concentrations of EDTA.*

These results reveal that EDTA acts as a mixed type inhibitor. The inhibition efficiency *IE*, at different inhibitor concentrations at 303 K for Al electrode in 0.5 M HCl solution was calculated from the Equation 1 [37-39]:

$$IE\,/\,\% = \left(1 - \frac{i_{corr}}{i^{0}_{corr}}\right) \times 100 \tag{1}$$

where, $i^{\circ}_{\mathrm{corr}}$ and i_{corr} are corrosion current density for uninhibited and inhibited solutions respecttively.

***Table 1**. The electrochemical kinetic parameters (i_{corr}, E_{corr}, β_c and β_a) and inhibition efficiency (IE) obtained from polarization curves of Al electrode in 0.5M HCl at 303 K in the absence and the presence of EDTA.*

c_{EDTA} / M	i_{corr} / mA cm^{-2}	-E_{corr} / mV	-β_c / mV dec^{-1}	-β_a/ mV dec^{-1}	*IE* / %
Blank	0.89	670	122	0.69	--
1.07 10^{-10}	0.47	660	118	0.60	47.2
2.13 10^{-10}	0.46	650	116	0.53	48.3
3.20 10^{-10}	0.35	630	118	0.52	60.7
4.27 10^{-10}	0.21	580	112	0.51	76.4
5.33 10^{-10}	0.12	530	115	0.50	86.5
6.40 10^{-10}	0.10	500	114	0.50	88.8

Mass loss

The mass losses of Al in 0.5 M HCl solution, with and without different concentrations of the EDTA were recorded after 100 min. of immersion at different temperatures. The corrosion rates of Al alloy were calculated using Equation 2 [37].

$$CR = \frac{87.6\Delta m}{Atd} \tag{2}$$

where Δ*m* is the mass lost (g), 87.6 is a constant, *A* is the surface area of the coupon (cm^2), *d* is the density (g cm^{-3}), *t* is the time of exposure (h). The calculated *CR* fits into the range (less than 0.50 mm year^{-1}) at which the application is acceptable [39]. Figure 3 (A and B) shows the variation in mass loss for Al coupons in the absence and the presence of EDTA. The mass loss in the presence of inhibitor is much smaller than the blank solution. The significant difference shows reduce impact on the *CR* of Al in 0.5 M HCl.

Both of the surface coverage (θ) and the inhibition efficiency (*IE*) were calculated using mass loss data according to Equations 3 and 4, respectively [38].

$$\theta = \left(1 - \frac{w_{inh}}{w_{blamk}}\right) \tag{3}$$

$$IE / \% = \theta \times 100 \tag{4}$$

where, w_{blank} is the corrosion rate in the uninhibited environments. w_{inh} is the corrosion in the inhibited environment. The high inhibition efficiency as the inhibitor concentration increases could be understood to be due to the reduction in corrosion rate. Thus, EDTA could be considered as an inhibitor of Al in 0. 5 M HCl solution given the high level of inhibition efficiency. The inhibitor efficiency, increased with the inhibitor concentration.

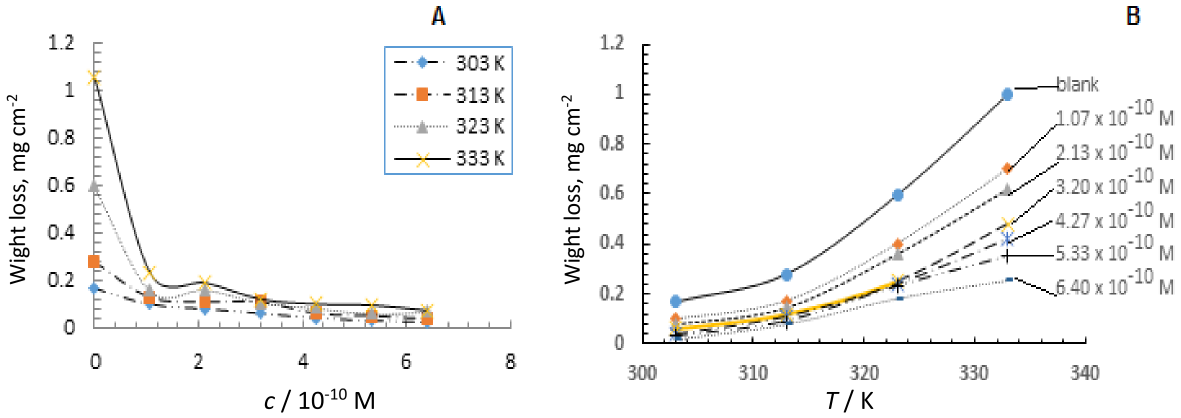

***Figure 3**. Mass loss of Al immersed for 100 min. in 50ml HCl in the presence or absence of EDTA at different temperatures and EDTA concentrations.*

Figure 4 shows the inhibition efficiency in different concentration of the EDTA and it is seen that the *IE* increases linearly with the inhibitor concentration.

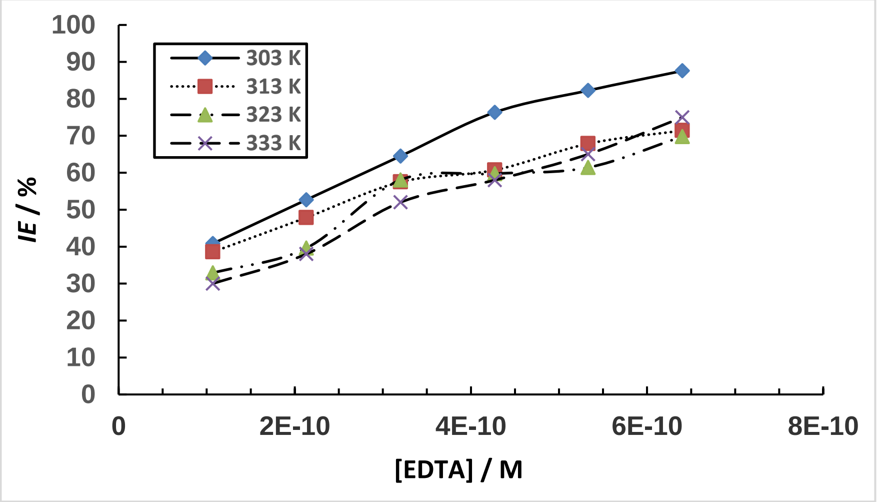

***Figure 4.** IE after 100 min. in 50 ml HCl at different [EDTA] at different temperatures*

Adsorption studies

Inhibition efficiencies of Al in 0.5 M HCl was increase with increasing additive concentrations of EDTA, this phenomenon can be explained on the basis of adsorption. Adsorption of the inhibitor can explain the nature of Al/EDTA interaction. In the acid solution, firstly inhibitor is adsorbed on the metal surface and cover certain area from corroded solution and decrease or prevent this area from dissolution, whereas corrosion reactions normally occurred on inhibitor-free areas. Accordingly, the area covered with inhibitor species (θ), can follow as a function of inhibitor concentration and/or solution temperature. When θ is tested as a function of the concentration (at constant temperature), the adsorption isotherm can be evaluated at the equilibrium condition. Four adsorption isotherms were tested using data from both weight loss and electrochemical techniques;

A. Langmuir's isotherm

The dependence of θ at the concentration of the inhibitor, was fitted to Langmuir's isotherm, assuming that, a fixed number of adsorption sites is present on Al surface, each one of these sites holds only one adsorbed species. Figure 5 shows linear plots of c/θ versus c with $R^2 \geq 0.90$, the average correlation coefficient, which suggests that adsorption was fitted to Langmuir's isotherm as in Equation 5 [37].

$$\frac{c}{\theta} = \frac{1}{K_{\text{ads}}} + c \tag{5}$$

where c is inhibitor concentration, K_{ads} adsorptive equilibrium constant representing the degree of adsorption (*i.e.* if K_{ads} having higher value, the inhibitor is strongly adsorbed on metal surfaces).

As shown in Table 2, the value of K_{ads} which was obtained from the reciprocal of the intercept of a Langmuir plot lines, and R^2 of all lines were near unity. This means that obtained results is fit well with Langmuir isotherm. The higher values of K_{ads} indicating a strong interaction between EDTA and the Al surface. It seemed, therefore, that electrostatic interaction (physisorption) between inhibitor molecules existing as cations should prevail over molecular interaction, and this often results in strong interactions (chemisorption).

Table 2. *Data obtained from Figure 3*

Temperature, K	303		313		323		333	
Technique used*	Wt.-loss	Elec.	Wt.-loss	Elec.	Wt.-loss	Elec.	Wt.-loss	Elec.
R^2	0.99	0.93	0.99	0.96	0.98	0.97	0.98	0.97
ΔG^o_{ads}, kJ mol^{-1}	-66.38	-66.38	-67.25	-70.95	-70.78	-70.76	-71.83	-75.16

* Wt.-loss - Weight loss measurements; Elec. - Electrochemical methods

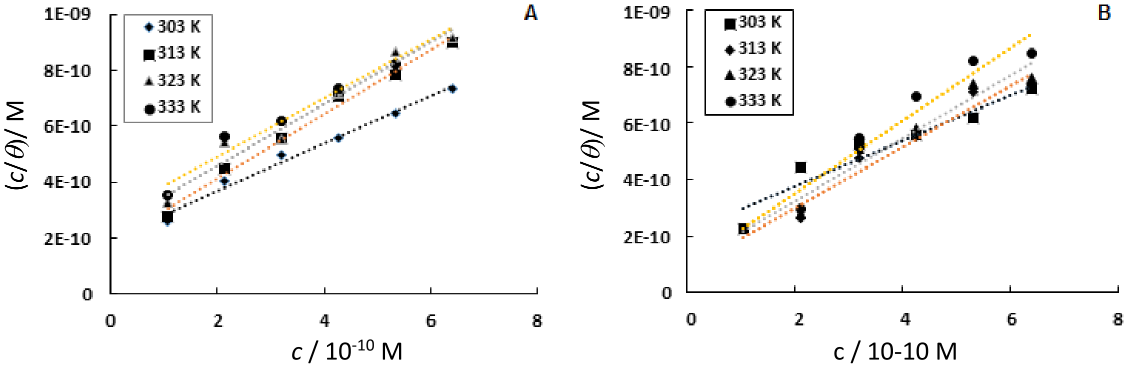

Figure 5. *Plots of* c/θ *versus* c *of Langmuir's adsorption isotherm for the corrosion of Al in 0.5 M HCl at different temperatures. A: From weight loss technique and B: from electrochemical technique*

The Equilibrium constant of adsorption K_{ads} is related to the standard adsorption free energy ($\Delta G^{\mathrm{o}}_{\mathrm{ads}}$) by Equation 6:

$$K_{ads} = \frac{1}{55.5}\exp\left(-\frac{\Delta G^{0}_{\mathrm{ads}}}{RT}\right) \tag{6}$$

where 55.5 is the concentration of water in the solution expressed in, R is the gas constant and T is the absolute temperature. From Table 1, the average value of standard adsorption free energy ($\Delta G^{\mathrm{o}}_{\mathrm{ads}}$) > -40 kJ mol^{-1}. The negative value of $\Delta G^{\mathrm{o}}_{\mathrm{ads}}$ ensures spontaneity of the adsorption process and the stability of the adsorbed layer on metal surfaces. In general, the values of ($\Delta G^{\mathrm{o}}_{\mathrm{ads}}$ up to -20 kJ mol^{-1} are consistent with the electrostatic interaction between the charged molecules and the charged metal (physisorption), while those around -40 kJ mol^{-1} or higher are associated with chemisorption as a result of sharing or transferring of electrons from organic molecules to metal surface to form a coordinate type of bond. In the present work, the calculated value of $\Delta G°$ in all studied temperatures in both techniques are > -40 kJ mol^{-1} indicating that the adsorption mechanism of EDTA on Al surfaces in 0.5 M HCl solution was typical of chemisorptions.

B. Temkin isotherm

The nature of the interaction at metal/solution interface is studied by Temkin isotherm. By assuming a uniform distribution of the adsorption energy that increases with the increase of the θ. Temkin isotherm model are given by the Equation (7a and 7b).

$$\exp\,(f,\theta) = K_{\mathrm{ads}}c \tag{7a}$$

and it is rearranged

$$\theta = (1/f)\log c + (1/f)\log K_{\mathrm{ads}} \tag{7b}$$

where K_{ads} is the equilibrium constant, c is the inhibitor concentration, θ is the surface coverage, f is the interaction term parameter, a lateral attraction between the adsorbing molecules is assumed if $f > 0$, but if $f < 0$, there is a lateral repulsion. The plot of θ versus log c, yields curve with linear correlation coefficient $R^2 \geq 0.90$, close to unity, in all cases. The obtained value of K_{ads}(average) ≈ 4.1×10^4 and ≈4.4×10^4 in case of weight loss and polarization techniques repetitively, $f > 0$ indicating a strong lateral attraction between the adsorbing molecules of EDTA and the surface of the Al.

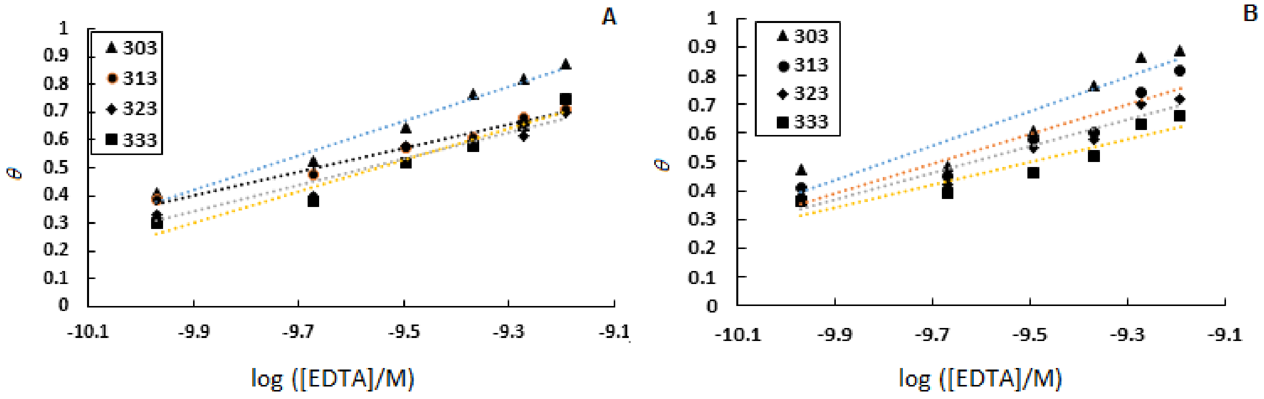

***Figure 6**. Plots of c versus θ of Temkin's adsorption isotherm for the corrosion of Al in 0.5 M HCl at different temperatures, A: from weight loss technique and B: from electrochemical technique*

Table 3. *Data obtained from Figure 4*

T / K	303		313		323		333	
Technique used*	Wt.-loss	Elec.	Wt.-loss	Elec.	Wt.-loss	Elec.	Wt.-loss	Elec.
f	1.6	1.7	2.3	1.93	2.1	2.15	1.8	*2.49*
K_{ads}	3.9 x10^4	4.1 x10^4	5.1 x10^4	4.2 x10^4	4.1 x10^4	4.4 x10^4	3.3 x10^4	*4.7* x10^4
R^2	0.95	0.90	0.96	0.90	0.95	0.91	0.95	*0.91*

* Wt.-loss - Weight loss measurements; Elec. - Electrochemical methods

C. Flory-Huggins isotherm

The amount of the inhibitor molecules that could displace the water molecules from the metal surface is studied using Flory-Huggins isotherm, which is showed by equation. 8

$$\log(\theta/c) = \log k + x \log(1-\theta) \tag{8}$$

where *x* is the size parameter that measure the number of adsorbed water molecules replaced by a given inhibitor molecule. Figure 7 shows the plot of log (θ/c) *vs.* log ($1-\theta$), linear relationships with $R^2 > 0.8$ is obtained, and indicating Flory-Huggins isotherm was obeyed. The obtained $(K_{ads})_{avg} = 1.5\times10^4$ and the calculated $\Delta G_{ads} > -34$ kJ/mol. The size parameter is approximately 1.

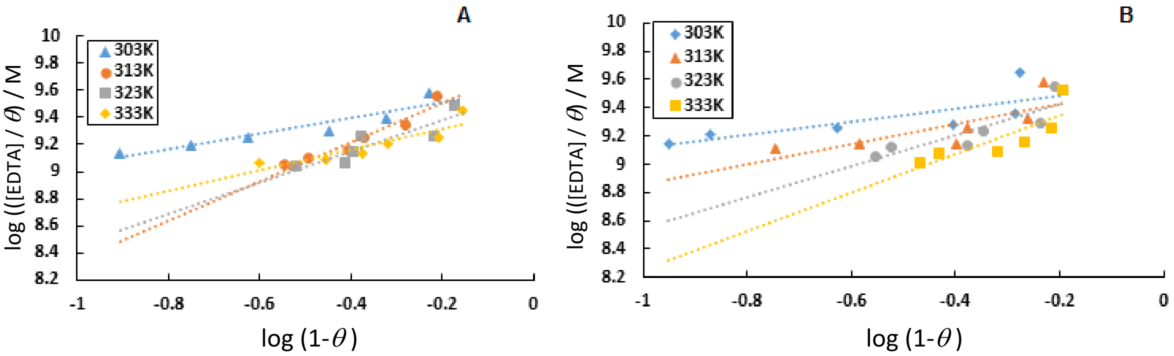

Figure 7. *Plots of log (1- θ) versus log (θ/c) of Flory Huggin's adsorption isotherm for the corrosion of Al in 0.5 M HCl at different temperatures, A: From weight loss technique and B: from electrochemical technique*

Table 4. *Data obtained from Figure 5*

T / K	303		313		323		333	
Technique used*	Wt.-loss	Elec.	Wt.-loss	Elec.	Wt.-loss	Elec.	Wt.-loss	Elec.
x	0.58	0.47	1.45	0.71	1.15	1.1	0.76	*1.4*
K_{ads}	1.5 x10^4	1.5x10^4	1.8 x10^4	1.4x10^4	1.5 x10^4	1.5x10^4	1.3 x10^4	*1.5* x10^4
R^2	0.96	0.90	0.98	0.90	0.95	0.91	0.95	*0.91*

* Wt.-loss - Weight loss measurements; Elec. - Electrochemical methods

D. Thermodynamic-kinetic model

The surface coverage values obtained from the gravimetric and polarization measurements were also fitted into the adsorption isotherm of the thermodynamic-kinetic model of El-Awady et al. are represented in Equation. 9

$$\log\left(\frac{\theta}{1-\theta}\right) = \log K'c + y \log c \tag{9}$$

where *c* is the concentration of the exudates, θ is the degree of surface coverage, K_{ads} is the Equilibrium constant of adsorption process, and $K_{ads} = K^{1/y}$. $1/y$ is the number of inhibitory molecules occupying one active site (or the number of water molecules replaced by one molecule of EDTA. Curves fitting of the data in the thermodynamic-kinetic model is shown in Fig. 8. This data gave straight lines, the values of $1/y$ and K_{ads} calculated from the El-Awady *et al.* curve model is given in

Table 4. The values of 1/*y* (average) obtained are more than unity in all cases, indicating that each molecule EDTA involved in the adsorption process is attached to more than one active site on the metal surface.

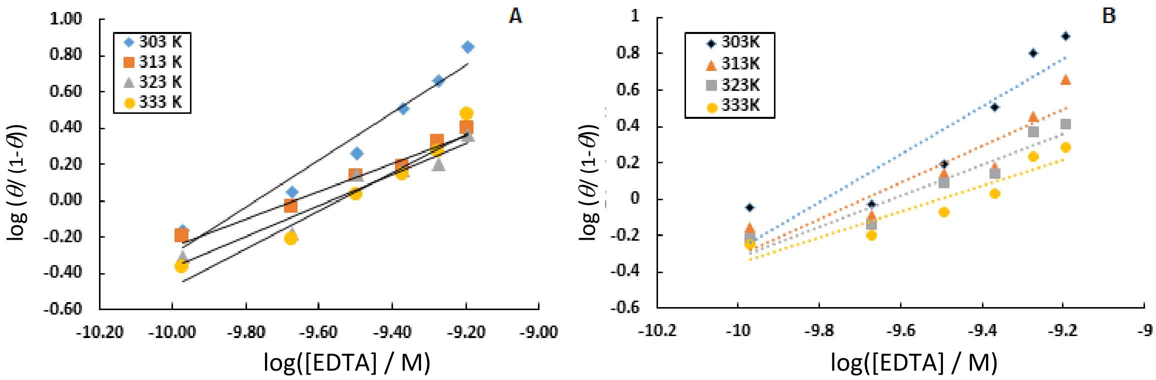

***Figure 8**. Plots of log* c *versus log (*θ */ 1-*θ*) of thermodynamic-kinetic model for the corrosion of Al in 0.5 M HCl at different temperatures, A: From weight loss technique and B: from electrochemical technique*

***Table 5**. Data obtained from Figure 5*

T / K	303		313		323		333	
Technique used*	Wt.-loss	Elec.	Wt.-loss	Elec.	Wt.-loss	Elec.	Wt.-loss	Elec.
y	1.31	1.32	0.77	1	0.86	0.84	1.05	*0.72*
1/y	0.77	0.76	1.31	1	1.22	1.18	0.92	*1.39*
K^l	7.7 x10^{14}	9.1x10^{14}	4.1 x10^{12}	3.7 x10^{13}	8.9 x10^{12}	7.9x 10^{12}	5.3x 10^{13}	*2.1x1012*
R^2	0.95	0.90	0.94	0.90	0.94	0.92	0.93	*0.91*

* Wt.-loss - Weight loss measurements; Elec. - Electrochemical methods

By rearrangement of Gibbs-Helmholtz equation we obtain Equation 10, which is used to calculate the enthalpy of adsorption (ΔH_{ads})

$$\Delta G_{\text{ads}}/T = (\Delta H_{\text{ads}}/T)\ K \qquad (10)$$

A plot between the variations of ($\Delta G_{\text{ads}}/T$) and ($1/T$) gave a straight line whose slope is ΔH_{ads} as shown in Figure 9. The entropy of adsorption ΔS_{ads} was calculated using the following thermodynamic Equation (Equation 11):

$$\Delta S_{\text{ads}} = (\Delta H_{\text{ads}}\ \Delta G_{\text{ads}})\ /\ \mathrm{T} \qquad (11)$$

where, data of ΔG_{ads} were taken from Langmuir isotherm results (from its R^2 value, it is the best fit model)

The obtained date of the calculated ΔH_{ads} and ΔS_{ads} was tabulated in Table 6.

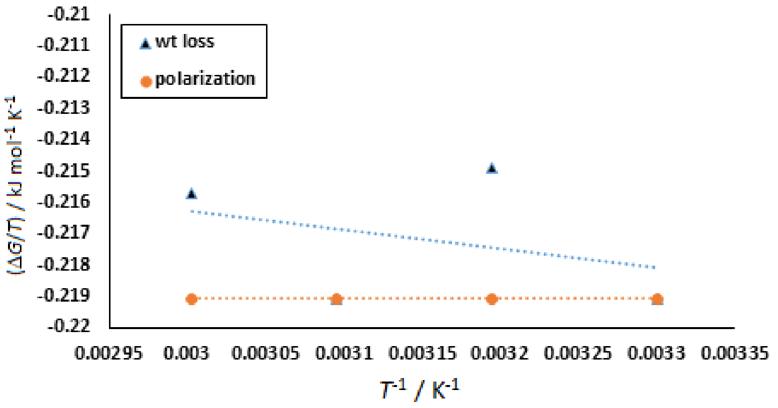

***Figure 9**. Gibbs-Helmholtz rearranged relation between (*ΔG_{ads}*/T) and (1/T)*

Table 6. *Adsorption thermodynamic parameters obtained using Langmuir isotherm*

T / K	303		313		323		333	
Technique used*	Wt.-loss	Elec.	Wt.-loss	Elec.	Wt.-loss	Elec.	Wt.-loss	Elec.
$-\Delta G_{\rm ads}$ / kJ mol^{-1}	66.38	66.38	67.25	70.95	70.78	70.76	71.83	75.16
$-\Delta H_{\rm ads}$ / kJ mol^{-1}	6.02	0.02	6.02	0.02	6.02	0.02	6.02	0.02
$\Delta S_{\rm ads}$ / J mol^{-1} K^{-1}	199.2	196.1	195.6	203.7	200.4	196.1	197.6	202.7

* Wt.-loss - Weight loss measurements; Elec. - Electrochemical methods

The negative sign of $\Delta H_{\rm ads}$ indicated the exothermic process of adsorption of the inhibitor on aluminum surface in HCl. The positive value of $\Delta S_{\rm ads}$ in the presence of inhibitor can be attributed to the increase in the solvent entropy and more positive desorption entropy. It is also interpreted that the increase of disorderness is due to more water molecules which can be desorbed from the metal surface by one inhibitor molecule. Therefore, it is revealed that decrease in the enthalpy is the driving force for the adsorption of the inhibitor on the surface of aluminum [28,29].The calculated values of heat of adsorption and entropy of adsorption are listed in Table (6).

Effect of temperature

Based on temperature effect, inhibitors may be classified into three groups:

1. Inhibitors whose inhibition efficiency (*IE)* decreases with temperature increase. The value of the apparent activation energy $E_{\rm a}$, found is greater than that in the uninhibited solution;
2. Inhibitors in whose *IE* does not change with temperature variation. The apparent activation energy $E_{\rm a}$, does not change with the presence or absence of inhibitors;
3. Inhibitors in whose presence the *IE* increases with temperature increase while the value of $E_{\rm a}$ for the process is smaller than that obtained in the uninhibited solution.

Thus, in examining the effect of temperature on the corrosion process in the presence of EDTA, the Arrhenius Equation (Eq. 12) is helpful

$$\log CR = \frac{-E_{\rm a}}{2.303\,RT} + \log A \qquad (12)$$

where CR is the corrosion rate, $E_{\rm a}$ is the apparent activation energy, R is the molar gas constant, T is the absolute temperature, and A is the frequency factor. Figure 10 represents the Arrhenius plot as log CR *vs.* 1/T for Al corrosion in 0.5 M HCl in free so inhibited solution, linear plots were obtained. The values of $E_{\rm a}$ were obtained from the slope of the Arrhenius plot and are presented in Table 8. From the table, it is seen that $E_{\rm a}$ increases in the presence of the inhibitors compared to the blank. The higher value of the activation energy of the process in an inhibitor's presence when compared to that in its absence is attributed to its physisorption, while the opposite is the case with chemisorption.

According to Eyring relationships (Eq. 13), both of S^* and H^* could be obtained,

$$-\ln \frac{Rh}{NT} R_c = \frac{\Delta H^*}{RT} - \frac{\Delta S^*}{R} \qquad (13)$$

where h is the Planck's constant (6.626176×10^{-34} J s), N is the Avogadro's number (6.02252×10^{-23} mol^{-1}), R is the universal gas constant, ΔH is the enthalpy of activation and ΔS is the entropy of activation. The kinetic results were found to fit the Arrhenius and Eyring equation, where plots of $1/T$ *vs.* $\ln Rc/T$ or $1/T$ *vs.* $-\ln(hRc/k_{\rm B}T)$ ($k_{\rm B}$ is Boltzman constant and equation the term R/N) resulted in good straight lines. The activation parameters ΔH^* and ΔS^* can be evaluated from the slopes and intercepts of the straight line.

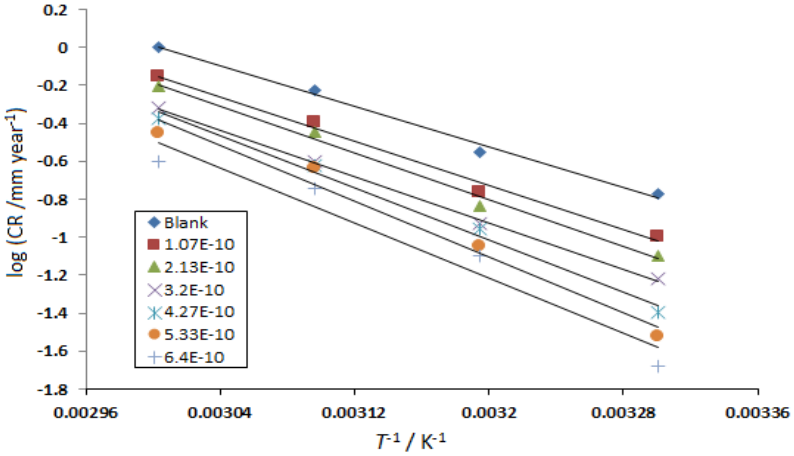

***Figure 10**. Arrhenius plot as log CR vs. 1/T for Al corrosion in 0.5 M HCl in the absence and presence of various concentrations of EDTA. Data obtained from weight loss technique*

***Table 7**. Activation energy, E_a for aluminum corrosion in the presence of EDTA in 0.5 M HCl.*

c / M	$-E_a$ / kJ mol^{-1}
0	51.05
1.07 x10^{-10}	56.01
2.13 x10^{-10}	59.11
3.20 x10^{-10}	58.55
4.27 x10^{-10}	65.93
5.33 x10^{-10}	70.02
6.40 x10^{-10}	69.64

Figure 11 shows Eyring plot and all lines are straight from which ΔH and ΔS were evaluated and their values are put in Table 8.

The positive values of ΔH reflect the endothermic dissolution of Al in the presence and absence of the inhibitor. The increase in ΔH_a with the increase in the concentration of the inhibitor for Al corrosion reveals that, the decrease in Al corrosion rate is mainly controlled by kinetic parameters of activation. The negative values of ΔS may reflect the association mechanism of corrosion, *i.e.*, the decrease in disorder takes place on going from reactants to the activated state.

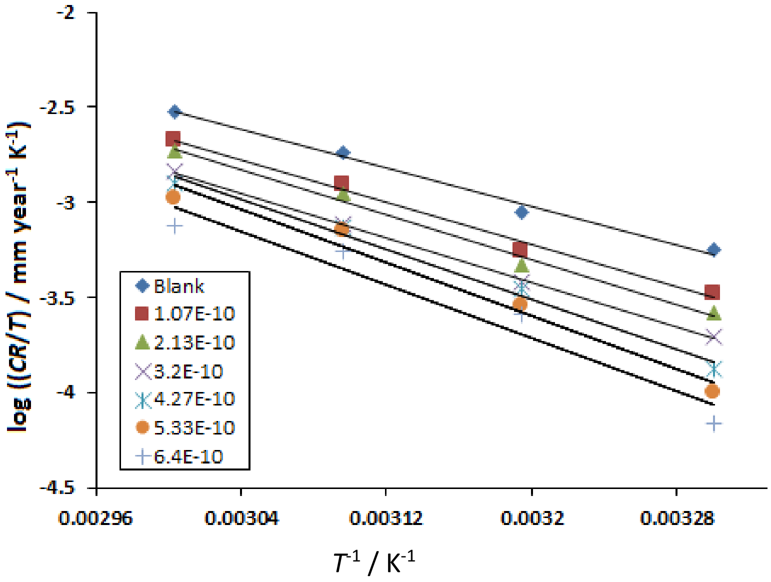

***Figure 11**. Eyring plot as log CR/T vs. 1/T for Al corrosion in 0.5 M HCl in the absence and presence of various concentrations of EDTA. Data obtained from weight loss technique*

***Table 8**. Thermodynamic parameters, ΔH and ΔS (for aluminum corrosion in the presence of EDTA in 0.5 M HCl)*

c / M	-Δ*S** / J mol^{-1} K^{-1}	Δ*H** / kJ mol^{-1}
0	100.49	21.02
1.07 10^{-10}	88.52	23.18
2.13 10^{-10}	80.07	24.52
3.20 10^{-10}	84.13	24.28
4.27 10^{-10}	62.26	27.48
5.33 10^{-10}	50.85	29.26
6.40 10^{-10}	54.26	29.10

SEM

SEM analysis of Al metal surface, The SEM image of the aluminum specimen before and after immersing in 0.5M HCl for100 min in the absence and presence of inhibitor system are shown in Figures 12 (A, B and C) repetitively. The SEM micrographs of aluminum surface after polishing (Fig. 8A) shows a smooth surface of the Al with no corrosion products on its surface. The SEM micrographs of the Al surface immersed in 0.5 M HCl (Fig. 12B) Shows its roughness which indicate the corrosion of Al in HCl. Fig. 12C indicates that in the presence of 10^{-10} M of EDTA, the surface coverage increases, which in turn results in the formation of insoluble complex on the surface of the metal (EDTA/inhibitor complex) and the surface is covered by a thin layer of inhibitor which effectively control the dissolution of aluminum.

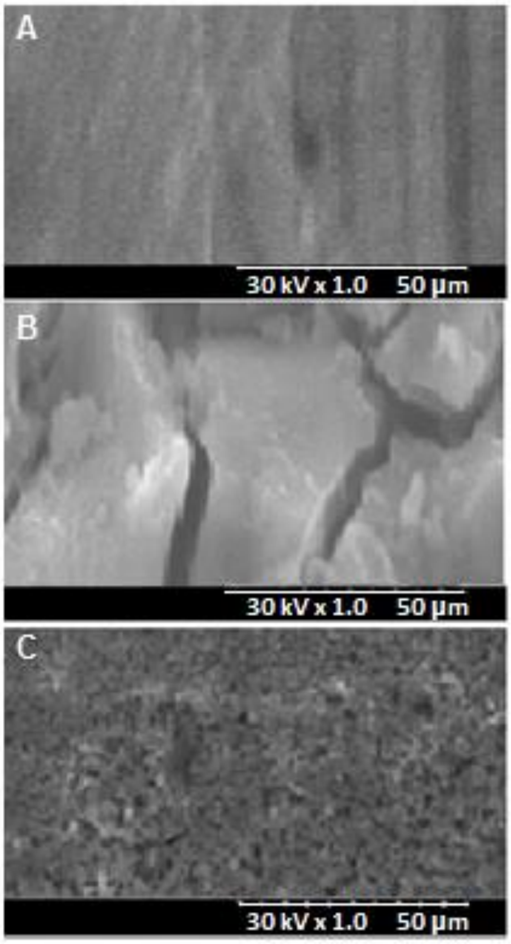

***Figure 12**. SEM of Al surface at 30 °C; A) After polishing, B) after immersion in 0.5 M HCl for 100 min., and C) the same as B but in the presence of 2.7x10^{-10} M EDTA*

Quantum chemical calculations

The activity properties of an inhibitor is related to its geometry as well as the nature of its Frontier Molecular Orbitals, FMO, namely, the HOMO and LUMO. Therefore, in this study, quantum chemical calculations were performed to investigate the relationship between molecular structure of this compound and their inhibition effect. The optimized molecular structure and the FMO density distribution of the studied molecule are shown in Figs. 13 and 14, and the calculated quantum chemical parameters are given in Table 9 .

Adsorption centers of the inhibitor molecules are predicted by FMO. These centers are responsible for the interaction with surface metal atoms [42,43]. It was reported that, inhibitors with high HOMO energy offering electrons to unoccupied d orbital of the metal. Where, inhibitors with lower LUMO energy accept electrons from metal surface, as the ΔE_g decreased, the efficiency of inhibitor improved [44]. The dipole moment (μ) of EDTA is 5.0542 Debye (1.69×10^{-29} C m), which is higher than that of H_2O ($\mu = 6.20\times10^{-30}$ C m = 1.856 Debye). The high value of μ probably increases the adsorption between EDTA and Al surface [45]. Accordingly, the adsorption of EDTA from the aqueous solution can be regarded as a quasi-substitution process between the EDTA in the aqueous phase [$EDTA_{sol}$] and water molecules at the electrode surface [H_2O_{ads}]. Analysis of Fig. 13 shows that the distribution of two energies HOMO and LUMO localized in the nitrogen and oxygen atoms, consequently this is the favorite sites for interaction with the metal surface. The total energy of the EDTA is equal to -691282.91 kcal mol^{-1}. This result indicated that EDTA is favorably adsorbed through the active centers of adsorption.

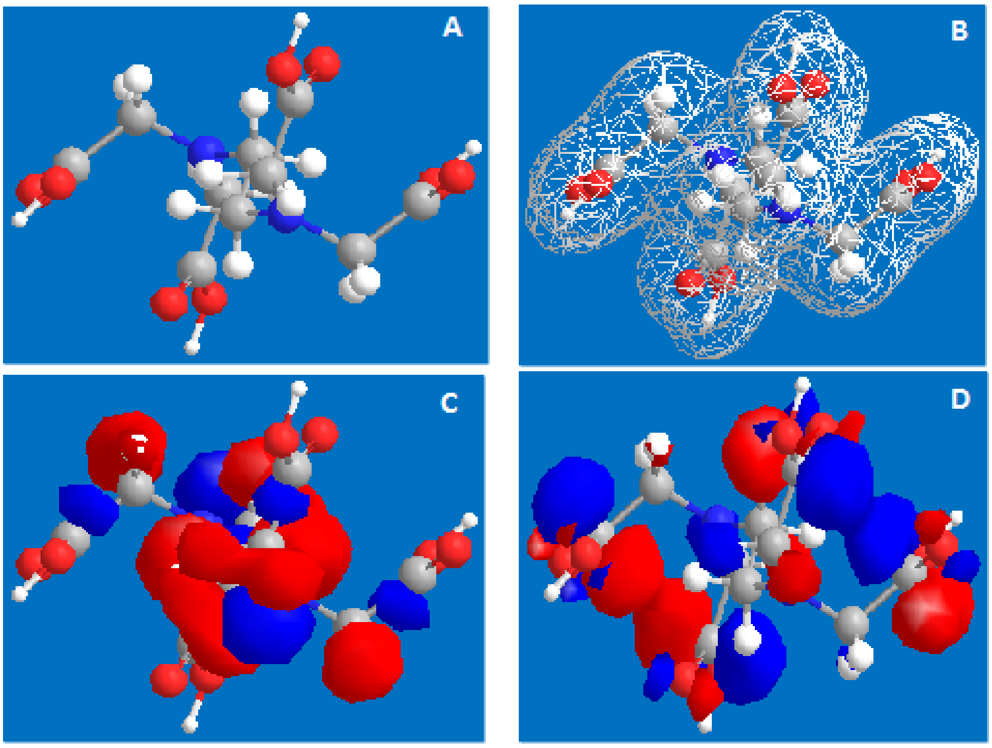

***Figure 13**.Optimized structure (A), total energy (B) Frontier molecular orbital diagrams; HUMO (C) and LUMO (D) of the EDTA by B3LYP/6-31G (d,p)*

The number of transferred electrons (ΔN) was also calculated according to Eq. (14) [46,47]

$$\Delta N = \frac{\chi_{Al} - \chi_{EDTA}}{2(\eta_{Al} + \eta_{EDTA})} \qquad (14)$$

Where χ_{Al} and χ_{EDTA} denote the absolute electronegativity of Al and EDTA molecule, respecttively; η_{Al} and η_{EDTA} denote the absolute hardness of Al and EDTA molecule, respectively. These quantities are related to electron affinity (A) and ionization potential (I)

$$\chi = \frac{I+A}{2} \text{ and } \eta = \frac{I-A}{2}$$

where, I and A are related in turn to E_{HOMO} and E_{LUMO}

$I = -E_{HOMO}$ and $A = -E_{LUMO}$

Values of η_{EDTA} and χ_{EDTA} were calculated by using the values of I and A obtained from quantum chemical calculation. The theoretical values of χ_{Al} and η_{Al} are 3.230 and 2.77 eV mol^{-1}, respectively [46]. The fraction of electrons transferred from inhibitor to the iron molecule (ΔN) was calculated. According to other reports [46,47], value of ΔN showed inhibition effect resulted from electrons donation. Also the softness is calculated depending upon the following relation:

$\sigma = 1/\eta$

In this study, the EDTA was the donators of electrons while the Al surface was the acceptor. The EDTA was bound to the Al surface, and thus formed inhibition adsorption layer against corrosion.

The adsorption centers of EDTA are estimated by Mulliken population analysis [48]. Authors believe that, the heteroatom with more negatively charged, is adsorbed on the metal surface through the donor-acceptor type reaction [43].

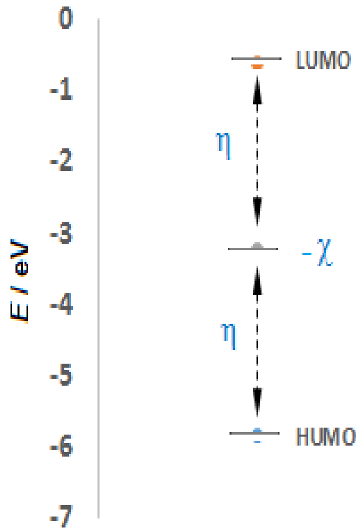

***Figure 14**. Energy distribution of EDTA using B3LYP/6-31G (d,p)*

***Table 9**. Calculated quantum chemical data for EDTA by B3LYP/6-31G (d,p)*

T.E. / kcal mol^{-1}	E_{HUMO} /eV	E_{LUMO} / eV	ΔE_{gap}/ eV	μ / Debye	I / eV	A / eV	χ / eV	η / eV	σ / eV	ΔN / eV
-691282.91	-5.849	-0.613	5.236	5.0542	5.849	0.613	3.231	2.618	0.382	-9.28×10^{-5}

The Mulliken charge of EDTA was shown in Table 10. It can be seen that the most favorable sites for the interaction with the Al surface were the following atoms: N32, N24, N30, N13, O23, O31, O15 and O14. Because these atoms have larger negative charge, that donate electron. This being the preferred zone for nucleophilic attack. For EDTA, the HOMO is localized over the nitrogen N and oxygen O atoms, consequently this is the favorite sites for interaction with the metal.

***Table 10**. Mulliken charge of EDTA by B3LYP/6-31G (d,p)*

Atom	Charge	Atom	Charge	Atom	Charge
1 C	0.214984	**22 C**	0.325515	**43 H**	0.121164
2 C	-0.086817	**23 O**	-0.567231	**44 H**	0.133160
3 C	-0.127361	**24 N**	-0.721935	**45 H**	0.133125
4 C	-0.144686	**25 C**	0.210742	**46 H**	0.140598
5 C	-0.066095	**26 C**	-0.010327	**47 H**	0.139131
6 C	0.015268	**27 C**	-0.083902	**48 H**	0.140004
7 C	0.216462	**28 C**	-0.148904	**49 H**	0.151805
8 C	0.040626	**29 C**	-0.123161	**50 H**	0.116621
9 C	-0.006822	**30 C**	0.326666	**51 H**	0.379970
10 C	0.000002	**31 O**	-0.567208	**52 H**	0.337115
11 C	-0.073095	**32 N**	-0.732883	**53 H**	0.147454
12 C	0.028970	**33 C**	0.185485	**54 H**	0.162757
13 N	-0.306615	**34 C**	0.001330	**55 H**	0.130880
14 O	-0.413216	**35 C**	-0.084377	**56 H**	0.379729
15 O	-0.419654	**36 C**	-0.146845	**57 H**	0.336862
16 N	-0.302210	**37 C**	-0.105158	**58 H**	0.154020
17 C	0.220038	**38 C**	0.388987	**59 H**	0.167164
18 C	-0.031616	**39 O**	-0.588086	**60 H**	0.137476
19 C	0.044560	**40 N**	-0.863854	**61 H**	0.351188
20 C	-0.021716	**41 H**	0.134813	**62 H**	0.302186
21 C	-0.140200	**42 H**	0.120365	**63 H**	0.346753

Conclusions

1. EDTA acts as inhibitors for aluminum corrosion in acidic medium at very low concentrations 10^{-10} M.
2. Inhibition efficiency of EDTA increases with increase in concentration of the inhibitors, but decreases with increase in temperature.
3. The values of ΔG^{o}_{ads} are negative, which suggests that the inhibitors were strongly adsorbed on the Al surface. The values obtained support the chemisorption adsorption mechanism.
4. EDTA is found to obey Langmuir, Temkin adsorption isotherm and kinetic-thermodynamic model of El-Awady et al for both weight loss and polarization techniques, from the fit of experimental data.
5. Thermodynamic parameters revealed that the adsorption process is spontaneous.
6. Quantum chemical parameters such as E_{HOMO}, E_{LUMO}, ΔE (E_{LUMO} - E_{HOMO}), dipole moment (μ), number of transferred electrons (ΔN), and total energy (TE) were found to give good correlation with experimentally determined inhibition efficiency

References

[1] J. W. Diggle, T. C. Downie, C. W. Goulding, *Chem. Rev.* **65** (1969) 365-405
[2] C. M. A. Brett, *J. Appl. Electrochem*. **20** (1990) 1000-1003
[3] J. B. Bessone, D. R. Salinas, C. E. Mayer, W. J. Lorenz, *Electrochim. Acta.* **37** (1992) 2283-2290
[4] G. R. T Schueller, S. R Taylor, E. E. Hajcsar, *J. Electrochem. Soc*, **139** (1992) 2799-2805
[5] T. D. Burleigh, A. T. Smith, *J. Electrochem. Soc*. **138(8)** (1991) L34-L35
[6] Q. Qu, S. Jiang, W. Bai, L. Li, *Electrochim. Acta* **52(24)** (2007) 6811-6820
[7] E. M. Sherif, S. M. Park, *Electrochim. Acta* **51(22)** (2006) 4665-4673
[8] M. A. Quraishi, R. Sardar, *Corrosion* **58(9)** (2002) 748-755
[9] S. Zor, P. Doğan, B. Yazici, *Corros. Sci.* **47(11)** (2005) 2700-2710
[10] S. Zor, P. Doğan, *Corros. Rev*. **22(3)** (2004) 209-217

[11] S. Zor, *Turkish J. Chem*. **26(3)** (2002) 403-408

[12] S. T. Selvi, V. Raman, N. Rajendran, *J. Appl. Electrochem*. **33(12)** (2003)1175-1182

[13] Y. K. Agrawal, J. D. Talati, M. D. Shah, *J. Appl. Electrochem*. **46(3)** (2004) 633-651

[14] M. A. Quraishi, H. K. Sharma, *Mater. Chem. Phys*. **78(1)** (2003) 18-21

[15] N. Ochoa, F., Moran N. Pebere, B. Tribollet, *Corros. Sci*. **47(3)** (2005) 593-604

[16] G. M. Treacy, A. L. Rudd, C. B. Breslin, *J. Appl. Electrochem*. **30(6)** (2000) 675-683

[17] N. S. Gaikwad, C. H. Bhosale, *Mater. Chem. Phys*. **76(2)** (2002) 198-203

[18] L. R. B. Holzle, D. S. Azambuja, C. M. S. Piatnicki, G. E. Englert, *Mater. Chem. Phys*. **91(2-3)** (2005) 375-380

[19] L. Di Palma, R. Mecozzi, *J. Hazard. Mater*. **147(3)** (2007) 768-775

[20] A. Nahle, *Bull. Electrochem*. **14(2)** (1998) 52-56

[21] I. Milošev, *J. Appl. Electrochem*. **32** (2002) 311-320

[22] H. S. Gardiyar, N. S. D. Elayathu, *Corrosion* **36(6)** (1980) 306-312

[23] J. N. Alhajji, M. R. Reda, *J. Electrochem. Soc*. **141(6)** (1994)1432-1439

[24] S. Zor, H. Ozkanzanc, M. Bingul, *Mater. Sci.* **44(6)** (2008) 850-856

[25] E. Kraka, D. Cremer, *J. Am. Chem. Soc*. **122 (2000)** 8245-8264

[26] R. G. Parr, W. Yang, *Density Functional Theory of Atoms and Molecules*; Oxford University Press, New York, NV, USA, 1989

[27] M. H. Cohen. *In Topics in Current Chemistry*; R. F. Nalewajski, Ed.; Springer-Verlag: Heidelberg, Germany, **183** (1996) 143-173

[28] R.T Sanderson, *J. Am. Chem. Soc*. **74 (1952)** 272-274

[29] M. K. Awad, *J. Electroanal. Chem*. **567** (2004) 219-225

[30] R. G. Parr, W. Yang, *J. Am. Chem. Soc*. **106** (1984) 4049-4050

[31] R. G. Pearson, *J. Am. Chem. Soc*. **85** (1963) 3533-3543

[32] A. D. Becke, *J. Chem. Phys.*, **96** (1992) 9489-9502

[33] A. D. Becke, *J. Chem. Phys*. **98** (1993) 1372-1377

[34] C. Lee, W. Yang, R. G. Parr, *Phys. Rev. B* **37** (1988) 785-789

[35] M. J. Frisch, *et al.*, *Gaussian 03, Revision B.01*, Gaussian, Inc., Pittsburgh, PA, USA, 2003.

[36] F. El-Hajjaji, R. A. Belkhmima, B. Zerga, M. Sfaira, M. Taleb, M. Ebn Touhami, B. Hammouti, S. S. Al-Deyab, E. Ebenso, *Int. J. Electrochem. Sci.*, **9** (2014) 4721-4731

[37] S. S. Abd El Rehim, S. M. Sayyah, M. M. El-Deeb, S. M. Kamal, R. E. Azooz, *Mater. Chem. Phys.* **123** (2010) 20-27

[38] S. S. Abd El Rehim, S. M. Sayyah, R. E. Azooz, *Port. Electrochim. Acta* **30(1)** (2012) 67-80

[39] D. William, Jr. Callister, *Materials Science and Engineering: an Introduction*, 7th edition, John Wiley & Sons, Inc., New York, NY, USA, 2007

[40] B. Bouklah, M. Hammouti, F. L. Bentiss, *Corr. Sci*. **48(9)** (2006) 2831-2842

[41] J. I. Bhat, D. P.Vijaya,*J. Korean Chem. Soc*. **55(5)** (2011) 835-841

[42] J. Fang, J. Li, *J. Mol. Struct. THEOCHEM* **593** (2002) 179-185

[43] G. Bereket, E. Hur, C. Ogˇretir, *J. Mol. Struct. THEOCHEM* **578** (2002) 79-88

[44] K.F. Khaled, *Appl. Surf. Sci.* **255** (2008) 1811-1818

[45] K. Ramji, D.R. Cairns, S. Rajeswari, *Appl. Surf. Sci*. **254** (2008) 4483-4493

[46] I. Lukovits, E. Kalman, F. Zucchi, *Corrosion* **57** (2001) 3-8

[47] H. Ju, Z. Kai, Y. Li, *Corros. Sci*. **50** (2008) 865-871

[48] M. Sahin, G. Gece, E.K. Arci, S. Bilgic, *J. Appl. Electrochem*, **382** (2008) 809-815

J. Electrochem. Sci. Eng. **6(3)** (2016) 253-263; doi: **10.5599/jese.307**

Open Access : : ISSN 1847-9286
www.jESE-online.org

Original scientific paper

Preparation of NiO-graphene oxide nanosensor for adsorptive stripping voltammetric determination of dinoterbon in food samples

Kasaram Roja, Puthalapattu Reddy Prasad, Punyasamudram Sandhya*,
Neelam Yugandhar Sreedhar✉

Electroanalytical Lab, Department of Chemistry, Sri Venkateswara University, Tirupati-517 502, A. P., India
**Department of Chemistry, Sri Padmavati Mahila Visvavidyalayam, Tirupati-517 502, A. P., India*

✉Corresponding Author: sreedhar_ny@rediffmail.com; Tel.: +91-877-2249666 (303)

Received: May 29, 2016; Revised: August 28, 2016; Accepted: September 9, 2016

Abstract

Graphene oxide (GO) modified NiO electrochemical nanosensor was developed for the determination of the dinoterbon in food samples using adsorptive stripping voltammetry. The modified nanosensor characterized by TEM, XRD, cyclic and adsorptive stripping voltammetry. Dinoterbon pesticide exhibited a single well-defined cathodic peak at pH 4.0 at Britton–Robinson buffer (-810.0 mV). The voltammetric characterization of the pesticide residues is evaluated and the parameter such as the effect of pH, scan rate, pulse amplitude, deposition potential and deposition time were optimized. The current–concentration plot obtained using this peak was straight-lined over the range from 0.05 to 50.00 μg mL^{-1} with limit of detection (LOD) 0.028 μg mL^{-1}. The proposed method was efficiently applied to the determination of dinoterbon in food samples. The mean recoveries of the pesticide 97.40 to 99.88 % with a relative standard deviation of 0.114 % in food samples respectively.

Keywords
Nanosensor, pesticide, voltammetry

Introduction

Wide-range usage of pesticides in agriculture, which leads to accumulation of pesticide residues in soil, water and food, has imposed a serious risk to human health and the environment worldwide [1]. Carbamates are one of the major classes of synthetic pesticides and due to their broad biological activity, these compounds are used on a large scale around the world [2]. The most commonly used pesticide with acaricides and fungicides activity is dinoterbon (2-*tert*-butyl-4,6-dinitrophenyl ethyl carbonate), see Fig. 1. It has been used extensively by farmers on major crops and other field crops [3]. However, it is used to prevent the larvae of the pests from growing up. Dinoterbon, like all fungicide pesticides exhibits toxicity to humans, including carcinogenicity, reproductive, developmental toxicity, neurotoxicity and acute toxicity [4].

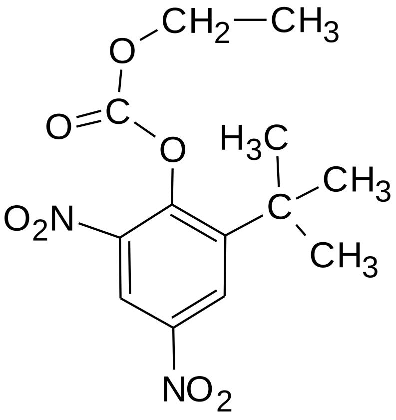

Figure 1. *Chemical structure of dinoterbon*

Graphene oxide a two-dimensional sheet of sp^2-bonded carbon atoms arranged in a honeycomb lattice, has attracted increasing attention since it was first isolated from three-dimensional graphite by mechanical exfoliation [5]. Due to its extraordinary thermal, mechanical, and electrical properties, graphene is usually considered as a competitive candidate for next generation electronic application devices such as super capacitors [6,7], batteries [8], fuel cells [9], solar cells [10], sensors [11], biosensors [12], energy storage [13] and catalysts [14]. However, many researchers have reported that the pure graphene actually exhibit unsatisfactory electrical conductivity because of the inevitable aggregation [15]. On the contrary, functionalized graphene sheets are easier to disperse in organic solvents, which can improve the dispersion and the homogeneity of the graphene with in aqueous solutions and yield novel types of electrically conductive nanocomposites [16-18]. Also, some of the useful and unique properties of graphene can only be realized after it is functionalized with organic groups such as hydroxyl, carboxyl and amino groups [19]. However, nanostructural metal oxide semiconductors possess a high surface area, nontoxicity, good biocompatibility, catalytic activity and chemical stability. Among the metal oxide semiconductors, nickel oxide (NiO), a p-type semiconductor with a wide band gap of 4.0 eV at 300 K, has been investigated for various applications such as solar cells, electrochemistry nanosensors [20,21]. Electrochemical nanosensors based voltammetric techniques have become extremely useful for the monitoring of pesticides [22,23].

In the present paper authors developed a novel NiO/GO electrochemical sensor prior to determination of dinoterbon pesticide residues at low concentration levels in food samples. The developed NiO-GO/GCE nanocomposite characterized by XRD, TEM, cyclic voltammetry and adsorptive stripping voltammetry (AdSV). Under the optimized operational conditions, the developed electrochemical nanosensor showed a specific and excellent performance with a good sensitivity, selectivity and wide dynamic range toward the quantification of dinoterbon. The results implicate the applicability of NiO/GO nanocomposite for rapid, sensitive and selective analysis of dinoterbon.

Experimental

Instrumentation and reagents

The electrochemical measurements were carried out in Autolab, three electrode systems consisting of modified glassy carbon electrode as a working electrode, Ag/AgCl (salt KCl) as a reference electrode and a platinum wire as an auxiliary electrode. Transmission electron microscopy (TEM) micrographs were performed a JEOL JEM 200CX operating at 200 kV. All reagents used were of analytical reagent grade. Ultrapure water was used throughout the experiment. The technical grade samples of dinoterbon fungicide in the form of 50 % wet-table powders were obtained from Bayer India Ltd. India.

Synthesis of nickel oxide nanocomposite

The NiO prepared from $NiNO_3{\cdot}6H_2O$ precursor by drop wise addition of 0.1 mol L^{-1}, KOH to a 0.1 M $NiNO_3{\cdot}6H_2O$ solution was kept vigorously stirred until the pH becomes 10.0. The precursor was filtered and rinsed with ultrapure water for twice and with ethanol once. Wet cake obtained was dried in oven at 100 °C overnight and was heated at 400 °C for 4 h to form black NiO nanoparticles.

Fabrication of the NiO-GO modified GCE

Before modification, the bare GCE (diameter 3 mm) was prudently polished to a mirror-like surface with 0.3, 0.05 M alumina slurries in sequence, then sonicated in ethanol and distilled water for 3 min respectively and dried with nitrogen. The 15 µL of NiO/GO suspension, prepared by simply mixing of NiO and GO suspensions with an appropriate volume ratio (v/v), was then dropped onto the clean electrode. Then the electrode was dried under room temperature, making the GO/GCE, NiO/GCE, GO and NiO-GO modified GCE.

Recommended analytical procedure for the determination of dinoterbon

An aliquot of working standard solution containing 5.0 µg mL^{-1} of dinoterbon pesticide is taken into 25 mL volumetric flask. To this 5 mL of Britton-Robinson buffer of (pH 4.0) added and transferred into electrolytic cell and diluted with 9.0 mL of supporting electrolyte and then deoxygenated with nitrogen gas for 5 min. The pesticide residue was treated with electrochemical NiO-GO nanocomposite on the surface of glassy carbon electrode. The dinoterbon pesticides were determined by cyclic and AdSV mode. Electrolysis was done at +0.8 to -1.20 V *vs.* SCE, accumulation time 80 s, pulse amplitude of 25 mV, scan rate 20 mV s^{-1} and pH 4.0. The maximum voltammetric peaks appearing for sample is at -0.810 V for dinoterbon.

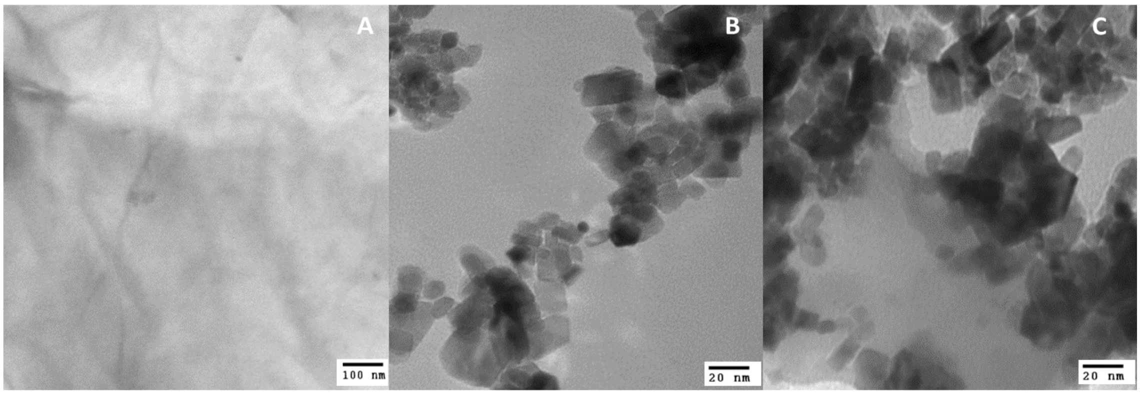

Figure 2. *TEM images of GO (A), NiO (B) and NiO/GO (C) modified glassy carbon electrode.*

Results and discussion

The structure of the GO fabricated NiO nanocomposite was examined by TEM and XRD. The morphological structure of the resulting NiO/GO was investigated by TEM (Fig. 2). The TEM image of single layer graphene oxide as shown in Fig. 2A. Fig. 2B, shows the TEM image of many NiO nanoparticles with sphere-like morphology are homogeneously dispersed. The many NiO nanoparticles with sphere-like morphology are homogeneously anchored on the surface of the GO sheets as shown in Fig 2C. The revealing sphere-like NiO nanoparticles with an average size of 28.6 nm. The XRD was used to investigate the phase structure of the resulting hybrids (Fig. 3). Fig. 3a shows the X-ray diffraction spectrum of NiO samples. The XRD patterns exhibit five prominent peaks at 2θ = 37.4°, 43.3°, 63.5°, 75.4° and 79.6° can be readily indexed as (111), (200), (220), (311) and (222) crystal planes of the bulk NiO, respectively. Fig. 3b shows the X-ray diffraction spectrum of GO fabricated NiO nanocomposite. The XRD pattern of the NiO/GO hybrid exhibits crystalline NiO diffraction peaks, which are in good agreement with the standard NiO (JCPDS No. 04-0835). The as-prepared GO displays a characteristic (002) peak at 25.4 which is in good agreement with previous reports [24]. By applying the Scherer formula to the XRD peaks, the average crystal size was calculated to be 22.4 nm for the nickel crystalline particles. This result indicates that the intermediate products was completely converted to NiO, which can be indexed as disordered stacked graphitic sheets. This finding indicates that GO is similar to previous reports [25].

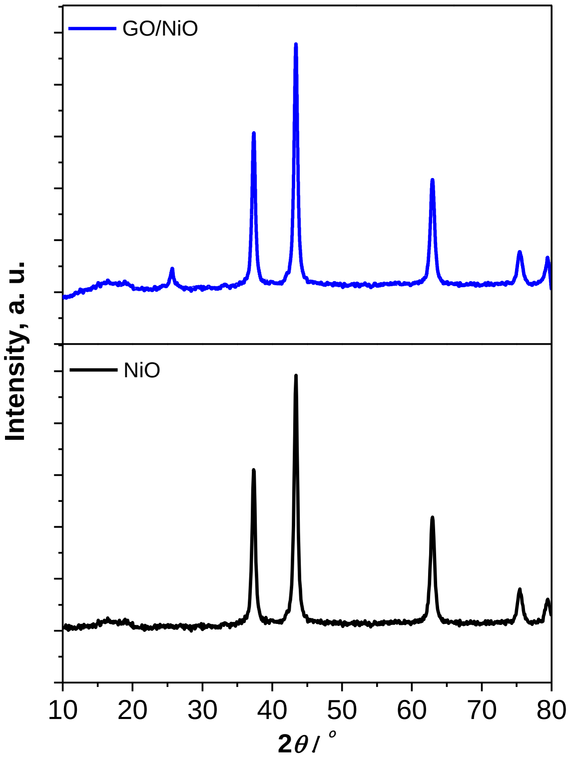

Figure 3. *XRD patterns of NiO and GO-NiO nanocomposite*

Voltammetric response of dinoterbon at various electrodes

The electrochemical performance of various electrodes was first investigated by cyclic voltammetry. Fig. 4, showed the cyclic voltammetry of the bare GCE, GO/GCE, NiO/GCE and NiO-GO/GCE in 0.1 M pH 4.0 BR buffer solution in the presence of 5.0 µg mL^{-1} dinoterbon. There was no obvious peak observed at bare GCE. However, a cathodic peak response at −0.810 V was observed at the NiO/GCE and GO/GCE, respectively. According to the currently accepted mechanism [24,25], the reduction peak should be attributed to a four-electron transfer reduction of the each nitro group (-NO_2) to give the hydroxylamine derivative. It can be reoxidized to the nitroso compound at a more positive potential. Under subsequent cycling, the nitroso group was reversibly reduced to respective hydroxylamine. Consequently, the redox behaviors of dinoterbon at the NiO-GO electrode is shown in scheme. 1.

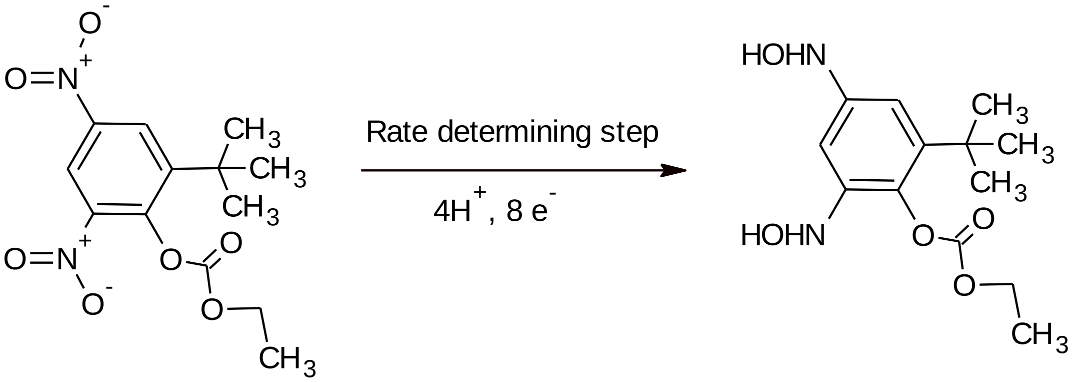

***Scheme 1.** Reduction mechanism of dinoterbon*

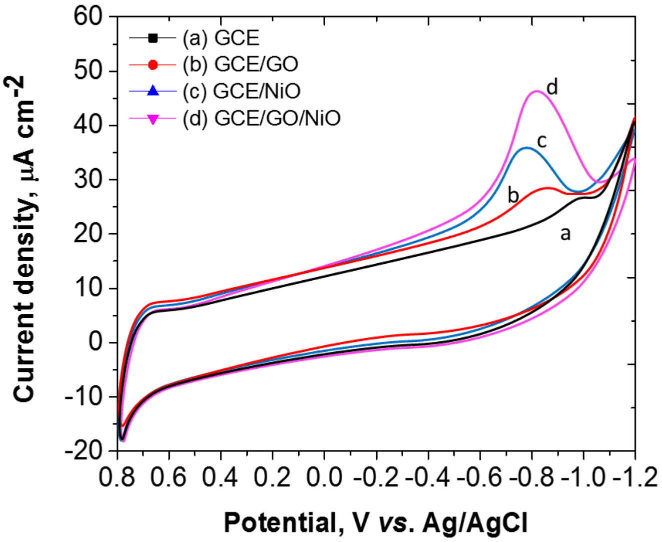

***Figure 4.** Typical cyclic voltammogram of dinoterbon for an accumulation time of 80 sec at GCE (a); GO/GCE (b); NiO/GCE (c); NiO-GO/GCE(d); rest time: 10 s; scan rate: 20 mVs^{-1}; concentration: 5.0 µg mL^{-1}; pH: 4.0 (BR buffer); pulse amplitude: 25 mV.*

The NiO-GO/GCE strong cathodic peak current response at -0.810 V, which was more prominent than those obtained at the bare GCE, NiO/GCE and GO/GCE. Furthermore, one can see that the incorporation of NiO into GO nanocomposite possesses more prominent peaks, indicating that the use of GO can significantly enhance the electron transfer between NiO-GO and the GC electrode. The normalized signal response of the different electrodes to 5.0 µg mL^{-1} dinoterbon were calculated. The dinoterbon response at the NiO-GO/GCE is more than the normalized response at the NiO/GCE and GO/GCE. These showed the NiO/GO/GCE gave the highest normalized signal response. The enhanced performance of the NiO-GO/GCE nanocomposite can be attributed to the excellent affinity of dinoterbon with NiO and the enhanced electron transfer, which could amplify the interaction between dinoterbon and NiO due to the formation of entangled NiO-GO structure.

The difference in the electrochemical behaviour of dinoterbon at bare GCE, GO/GCE and NiOGO/GCE were also evaluated by AdSV in 0.1 mol L-1 BR buffer pH 4.0, containing 20 µg mL-1 dinoterbon, at scan rate of 20 mV s–1 (Fig. 5).

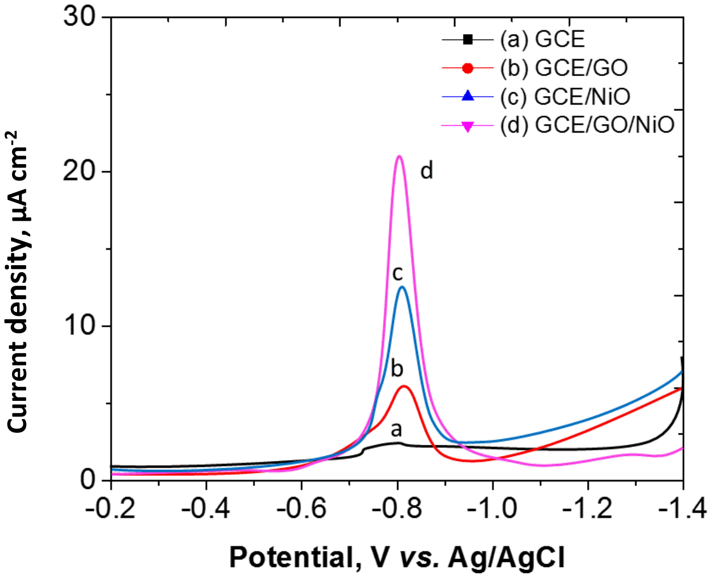

Figure 5. *Adsorptive stripping voltammogram of dinoterbon at bare GCE (a), GCE/GO (b), GCE/NiO (c), NiO-GO/GC electrode(d); pH 4.0 (BR buffer) accumulation time: 80 s.; stirring rate: 1500 rpm; scan rate:20 mVs^{-1}; pulse amplitude: 25 mV.*

No characteristic peak related to the dinoterbon reduction was observed for the bare glassy carbon electrode which indicates GCE does not exhibit electrocatalytic activity for dinoterbon. However, when the determination was performed at the GO/GCE, NiO/GCE and NiO-GO/GCE electrodes, there was a peak for dinoterbon at -0.713 and -0.688 V, respectively. These peaks indicate that both GO/GCE and NiO-GO/GCE electrodes exhibit electrocatalytic activity and can identify the fungicide dinoterbon. However, the electrode modified with the hybrid material, NiO-GO/GCE, showed a well electrocatalytic response with higher catalytic current and the potential was less positive compared to the other modified electrodes. It can be explained due to the GO physically incorporated into the NiO nanocomposite were oriented in such a way that their extremities were more susceptible to reacting with the fungicide dinoterbon.

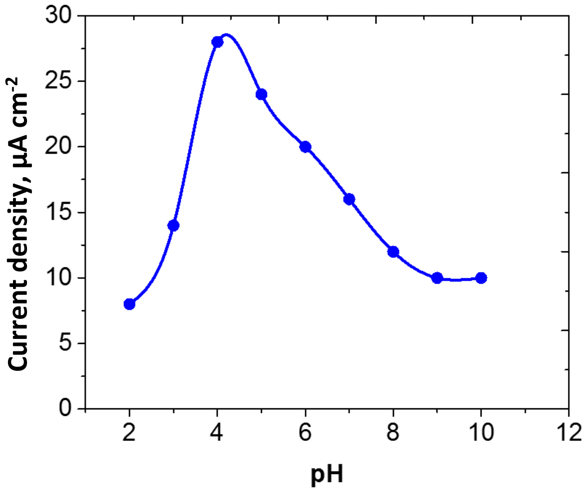

Figure 6. *Effect of pH on dinoterbon at NiO-GCE/GCE; accumulation time: 80 s.; rest time: 10 s., stirring rate: 1500 rpm; scan rate: 20 mVs^{-1}; concentration: 5.0 μg mL^{-1}; pulse amplitude: 25 mV.*

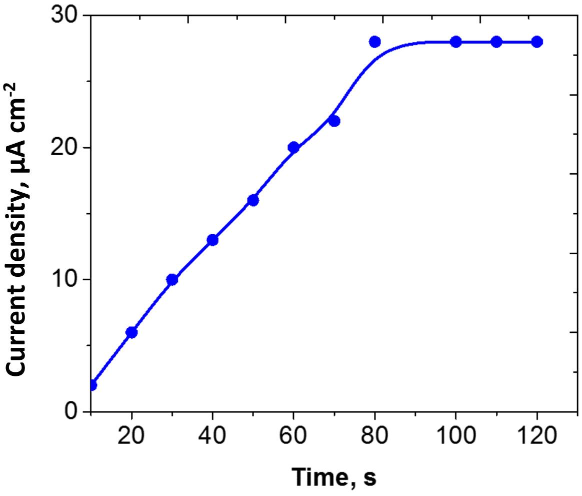

Figure 7*. Effect of accumulation time on the AdSV response of dinoterbon at NiO-GO/GCE; rest time:10 s; stirring rate: 1500 rpm; scan rate: 20 mVs^{-1}; concentration: 5.0 μg mL^{-1}; pH: 4.0 (BR buffer); pulse amplitude: 25mV.*

Optimization parameters for dinoterbon detection at NiO-GO/GCE

The peaks of AdSV for dinoterbon (20 µg mL^{-1}) with NiO-GO/GCE were compared in different supporting electrolytes, namely, 0.1 mol L^{-1} Britton–Robinson buffer, 0.2 mol L^{-1} sodium acetate–acetic acid buffer, 0.1 mol L^{-1} phosphate buffer, carbonate buffer, and borate buffer solution. The highest peak current was obtained with 0.1 mol L^{-1} Britton–Robinson buffer as the electrolyte. Thus, 0.1 mol L-1 Britton–Robinson buffer was chosen as the analytical medium, in which the peak shape was well defined. As shown in Fig. 6, the effects of pH on the AdSV peak current of dinoterbon (20 µg mL^{-1}) with NiO-GO/GCE was also studied in 0.1 M Britton–Robinson buffer (pH 2.0–10.0). The maximum current appeared at pH 4.0 for the determination of dinoterbon. In the following experiment, pH 4.0 was selected.

Further investigation of electroactivities using the various ratios of NiO to GO was preliminarily studied to optimise the catalytic performance of NiO-GO/GCE toward dinoterbon. The mass ratio of NiO:GO was varied from 1:0.25 to 1:0.5, 1:1, 1:2, and 1:4; the highest peak current was obtained at a mass ratio of 1:2. The catalytic activity of the as-prepared NiO-GO hybrid for dinoterbon reduction was under the synergistic effect of the primary component (NiO) and the support component (GO). The combination of GO with NiO is an ideal strategy of improving the catalytic performance of NiO by enhancing its charge transfer efficiency. However, excessive GO in the composite can also decrease the loading level of NiO. Thus, the mass ratio of NiO-GO has an important influence on the catalytic oxidation reactions of dinoterbon. The optimum catalytic performance was achieved from NiO-GO with a mass ratio of 1:2. The excellent adsorption capacity of GO, (2) the larger effective surface area of NiO-GO/GCE, and (3) the synergistic catalytic effect of GO, and NiO toward dinoterbon, as detailed above.

The AdSV peak current of dinoterbon increases with accumulation time increasing from 0 to 80 s, as shown in Fig. 7. But when it exceeds 80 s the peak current remains almost constant for a 5.0 µg mL^{-1} dinoterbon solution, meaning that an accumulation/or extraction equilibrium is achieved at the electrode/solution interface. The influence of accumulation potential is examined from +0.3 to −0.5 V. The results showed that the peak current of dinoterbon is almost independent of accumulation potential. This is due to the neutral nature of dinoterbon under this condition. Thus, an accumulation is performed under open-circuit.

The effect of pulse height variation on the peak current of dinoterbon voltammograms was studied in the range of 15–100 mV. The obtained results showed that increasing the pulse heights up to 25 mV will cause an increase in peak current. Pulse heights more than 25 mV cause broadening of the dinoterbon voltammogram and so decreasing the peak current intensity of the analyte. So the optimum pulse height value was selected to be 25 mV.

Table 1. *Tolerance limits of matrix substances for determination of dinoterbon by the AdSV method*

substances	Tolerance limit, µg mL^{-1}	substances	Tolerance limit, µg mL^{-1}
Na^+, K^+, NH_4^+	1200	Cu^{2+}, Cr^{6+}	60
$Ca^{2+,}$ Mg^{2+}	1000	Phenols and nitrophenols	50
Cl^-, NO_3^-, HCO_3^-	800		
PO_4^-, SO_4^{2-}	750		
Al^{3+}, Zn^{2+}, Fe(II)	400		

Interference study

Prior to the application of the developed method on food samples it was vital to investigate the effect of some of the interfering ions on the recovery percentage of dinoterbon. The AdSV determination of dinoterbon was tested in the presence of spiked known amounts of interfering ions and molecules. The tolerance limit was defined as the amount of the foreign substance causing a change of ±5 % in the peak current intensity reading. The tolerable limits of interfering substance are given in Table 1. The results showed that most of the investigated substances do not interfere in the AdSV determination of dinoterbon in food samples

Determination of dinoterbon pesticide in food samples

The food samples namely, Onion (*Alium sepa*), Cauliflower (*Brassica olera. var. Botrytis*), Lady's Finger *(Abelmoschus esculentus)*, Cucumber (*Cucumis sativus*), Sweet Potato (*Ipomoea*) and Tomato (*Lycopersicum esculentum*) were collected from the Tirupati local market, A.P, India. Afterwards, they were taken in small mesh and dried in an oven at 90 °C to constant weight. In order to digest the samples, 1.0 g of food sample was digested with 10 mL concentrated HNO_3 (65 %) and 3.0 mL H_2O_2 (30 %) in microwave system, then again evaporated to near dryness. After evaporation, 10 mL of deionized water was added and the sample was mixed. The resulting mixture was filtered through filter paper. The filtrate was diluted to 25 mL with deionized water. All the samples were stored in polyethylene bottles. For sample analysis spiked with dinoterbon standards at 10.0, 50.0, 100 µg mL^{-1}. Then 10 µg mL^{-1} of the digested sample solution was dissolved in 25 µL BR buffer solution at pH 4.0 for determination. Samples were also analyzed by GC methods. The recovery rates in food samples exhibited a range of 97.40 to 99.88 % (average of five determinations) with less than 1.72 % of RSD and precision data are reported in Table 2.

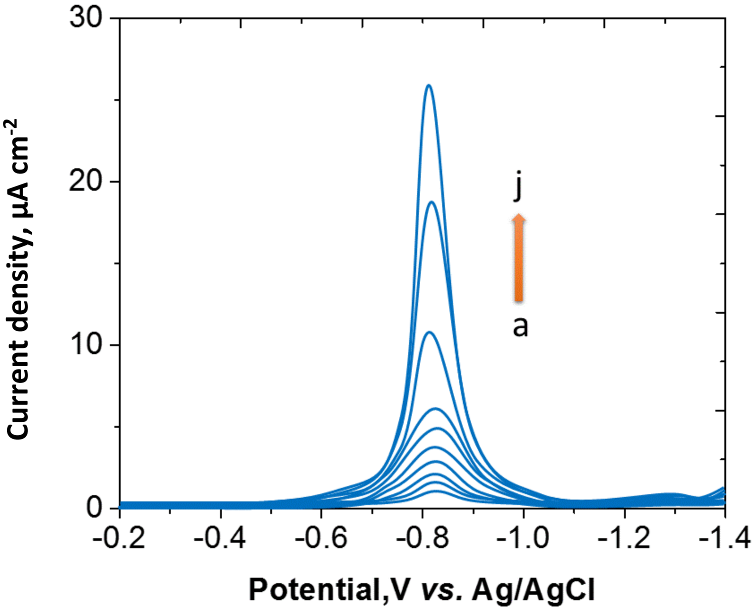

Figure 8. *AdSV of the NiO-GO/GCE by (a) 0.2, (b) 0.4, (c) 0.8, (d) 1.0 (e) 2.0 (f) 4.0, (g) 8.0, (h) 16, (i) 32 (j) 50 µg mL^{-1} dinoterbon; accumulation time of 80 s, stirring rate:1500 rpm; scan rate: 20 mVs^{-1}; pH: 4.0 (BR buffer); pulse amplitude:25 mV.*

Adsorptive stripping voltammetric quantification of dinoterbon

Due to the good sensitivity of adsorptive stripping voltammetry was applied for further electrochemical detection of dinoterbon under the optimized operating conditions. Fig. 8, displayed the AdSV of the NiO-GO/GCE in 0.1 mol L^{-1} pH 4.0 BR buffer solution at a potential range from −0.4 V to 0.2 V in the presence of various dinoterbon concentrations. Well-defined peaks, proportional to the concentration of the corresponding dinoterbon, were observed in plots. The corresponding calibration plot was presented in Fig. 9, indicating that the response was gradually saturated at a higher dinoterbon concentration. Under the optimal experimental conditions, NiO–GO/GCE was used to detect dinoterbon by AdSV. It can be seen from the figure that well-defined AdSV responses from adsorbed dinoterbon were observed and increased gradually with the increase of the dinoterbon concentration. The good linear relationship between oxidation current and log *C* dinoterbon was obtained from 0.05 μg mL^{-1} to 50.0 μg mL^{-1} with the regression equation of i / μA = 0.4742x+0.1283 (R = 0.9992). A LOD of 0.0283 μg mL^{-1} was calculated according to the formula LOD = 3 σ/S, where σ is the mean of standard deviation of five measurements taken from the signal obtained from the blank, S is the slope of the calibration curve, and the number 3 comes from the required ~98 % level of confidence in the difference between the observed signal and the blank response.

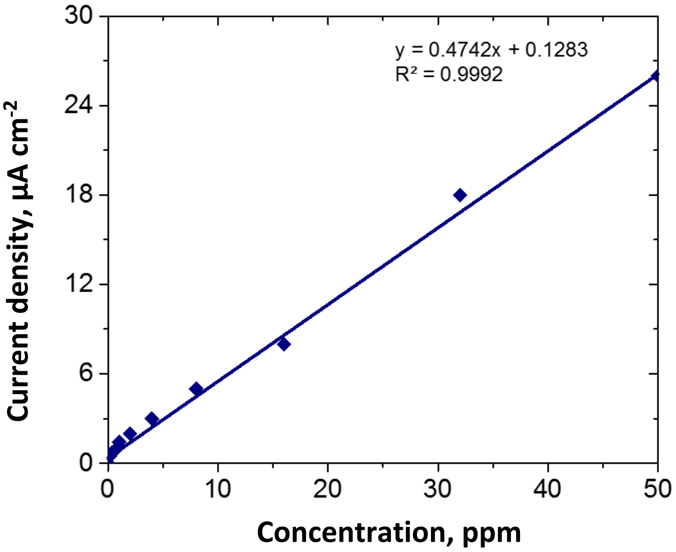

Figure 9. *Calibration curve on the AdSV response of dinoterbon at NiO-GO/GCE; 5.0 μg mL^{-1}; accumulation time of 80 s, stirring rate: 1500 rpm; scan rate: 20 mV s^{-1}; pH: 4.0 (BR buffer); pulse amplitude: 25 mV.*

Table 2. *AdSV determination of pesticide in food samples (no. of determinations =5)*

Name of the food samples	Amount added, μg mL^{-1}	Amount found, μg mL^{-1}	Recovery, %	R.S.D*
Onion	5.0	4.98	99.60	0.11
	10.0	9.92	99.20	0.08
	25.0	24.96	99.84	0.16
Cauliflower	5.0	4.87	97.40	0.02
	10.0	9.94	99.40	0.12
	25.0	24.82	99.28	0.14
Cucumber	5.0	4.88	97.60	0.22
	10.0	9.94	99.40	0.04
	25.0	24.96	99.84	0.16
Sweet Potato	5.0	4.91	98.20	0.12
	10.0	9.89	98.90	0.05
	25.0	24.97	99.88	0.20
Tomato	5.0	4.99	99.80	0.16
	10.0	9.93	99.30	0.08
	25.0	24.89	99.56	0.06

*R.S.D: Relative standard deviation

The inter-assay precision was estimated at six different NiO-GO a nanocomposite modified electrodes for the determinations in 0.1 mol L^{-1} BR buffer (pH = 4.0) containing 5.0 μg L^{-1} dinoterbon.

Similarly, the intra-assay precision was evaluated by assaying one working electrode for five replicate determinations under unvarying conditions. The relative standard deviation values of inter-assay and intra-assay were found to be 6.8% and 4.6%, respectively, indicating acceptable precision and reproducibility. In addition, the developed electrochemical metal oxide nanosensor (NiO-GO) was very stable at room temperature. No obvious decrease in the electrochemical response was observed in the 5 days and over ~90% of the initial response remained after four weeks, indicating that is acceptable stability.

Conclusions

In this paper, combining the advantageous characteristics of dinoterbon at NiO/GCE, GO/GCE and the NiO-GO/GCE nanocomposite have been prepared. The NiO-GO/GCE nanocomposite with excellent electrocatlytic and between NiO and GO modified electrode. It's improved the absorptivity and charge transfer properties on the surface of nanocomposite and improve the stability. The constructed NiO-GO/GCE sensor exhibited many advantages such as low applied potential, good fabrication reproducibility, acceptable stability, fast response and low detection limit. The NiO-GO/GCE sensor has potential application in monitoring of dinoterbon in food samples.

References

[1] R. C. Gupta, *Toxicol. Mechan. Methods*, **14** (2004) 103-143

[2] W. T. Song, Y. Q. Zhang, G. J. Li, H. Y. Chen, H. Wang, Q. Zhao, D. He, C. Zhao, L. Ding, *Food Chem*. **143** (2014) 192-198

[3] P. Lautala, M. Kivimaa, H. Salomies, E. Elovaara, J. Taskinen, *Eur. J. Pharm. Sci.* **4** (1996) S167-168

[4] X. Guo, Z. Wang, S. Zhou, *Talanta* **6** (2004) 135-139

[5] K. S. Novoselov, A. K. Geim, S. V. Morozov, D. Jiang, Y. Zhang, S. V. Dubonos, I. V. Grigorieva, A. A. Firsov, *Science* **306** (2004) 666-669

[6] M. D. Stoller, S. J. Park, Y. W. Zhu, J. H. An, R. S. Ruoff, *Nano Letters* **8** (2008) 3498-3502

[7] A. K. Mishra, S. Ramaprabhu, *Journal of Physical Chemistry C*, **115** (2011) 14006-14013

[8] E. Yoo, J. Kim, E. Hosono, H. S. Zhou, T. Kudo, I. Honma, *Nano Letters* **8** (2008) 2277-2282

[9] J. Xiao, D. Mei, X. Li, W. Xu, D. Wang, G. L. Graff, W. D. Bennett, Z. Nie, *Nano Letters* **11** (2011) 5071-5078

[10] X. Wang, L.J. Zhi, N. Tsao, Z. Tomovic, J.L. Li, K. Mullen, *Angew and te Chemie International Edition* **47** (2008) 2990-2992

[11] S. J. Guo, S. J. Dong, *Journal of Materials Chemistry* **21** (2011) 18503-18516

[12] J. D. Qiu, J. Huang, R. P. Liang, *Sensors and Actuators B* **160** (2011) 287-294

[13] D. Chen, L. H. Tang, J. H. Li, *Chemical Society Reviews* **39** (2010) 3157-3180

[14] S. S. Han, H. Kim, N. Park, *Journal of Physical Chemistry* **C115** (2011) 24696-24701.

[15] D. Li, R. B. Kaner, *Science* **320** (2008) 1170-1171

[16] S. Stankovich, D. A. Dikin, G. H. B. Dommett, K.M. Kohlhaas, E.J. Zimney, E.A. Stach, R.D. Piner, S.T. Nguyen, R.S. Ruoff, *Nature* **442** (2006) 282-286

[17] D. Li, R. B. Kaner, *Science* **320** (2008) 1170-1171.

[18] K. Wang, Q. Liu, L.N. Dai, J.J. Yan, C. Ju, B.J. Qiu, X.Y. Wu, *Analytica Chimica Acta,* **695** (2011) 81-84

[19] D. Zheng, S. K. Vashist, K. Al-Rubeaan, J.H.T. Luong, F.S. Sheu, *Talanta,* **99** (2012) 22-28

[20] T. Seto, H. Akinaga, F. Talano, K. Koga, T. Orii, M. Hirasawa, *J.Phys. Chem.B* **109** (2005)13403-13405

[21] P. Lunkenheimer, A. Loidl, C. Ottermann, H. Bange, *Phys.Rev.B:Condens. Matter* **44** (1991) 5927-5930

[22] C. N. Reddy, P. R. Prasad, and N.Y. Sreedhar, *Journal of Analytical Methods in Chemistry* **2013** (2013) 1-7

[23] D. Rekha, N. Y. Sreedhar, P.R. Prasad, *Global journal of frontier Science research*, **10** (2010) 21-29

[24] Y. Li, B. Zhang, J.X. Zhao, Z. Ge, X. Zhao, L. Zou, *Applied Surface Science* **279** (2013) 367-373

[25] H. Zhang, H. Huang, H. Ming, H. Li, L. Zhang, Y. Liu and Z. Kang, *J. Mater. Chem.*, **22** (2012) 10501-10506

J. Electrochem. Sci. Eng. **6(3)** (2016) 265-276; doi: **10.5599/jese.308**

Open Access : : ISSN 1847-9286
www.jESE-online.org

Original scientific paper

Simultaneous electrochemical determination of acetaminophen and metoclopramide at electrochemically pre-treated disposable graphite pencil electrode

Shreekant M. Patil, Vijay P. Pattar, Sharanappa T. Nandibewoor✉

P. G. Department of Studies in Chemistry, Karnatak University, Dharwad 580003, India

✉Corresponding author: stnandibewoor@yahoo.com; Tel.: +91 836 2215286; Fax: +91 836 2747884

Received: May 30, 2016; Revised: September 22, 2016; Accepted: September 26, 2016

Abstract

A sensitive and economic voltammetric method was developed for the simultaneous determination of acetaminophen (AMP) and metoclopramide (MCP) using pre-treated graphite pencil electrode (PTGPE). Compared to a graphite pencil electrode, the pre-treated electrode showed an apparent shift of the oxidation potentials in the positive direction and a notable enhancement in the current responses for both AMP and MCP. Cyclic voltammetry (CV) was used to study the voltammetric behavior of the drugs, while differential pulse voltammetry (DPV) was used to determine AMP and MCP simultaneously. The dependence of the current on scan rate, pH and concentration was investigated to boost the experimental conditions for simultaneous determination. The calibration curves were obtained over the range of 0.1×10^{-7} *to* 1.1×10^{-7} *M, the concentration of each of both the drugs was varied by keeping the other constant, and achieved lower detection limit of 3.25 nM for AMP and 1.16 nM for MCP. The developed method was found to be selective and rapid for the simultaneous determination of AMP and MCP. The proposed method was applied simultaneously in real samples and pharmaceutical samples, with satisfactory results.*

Keywords
Acetaminophen, metoclopramide, voltammetry, graphite pencil electrode, analytical applications

---

Introduction

The development of a sensitive, simple, reliable and rapid method for the determination of analyte is of great importance. The pre-treated graphite pencil electrode (PTGPE) has been used as a biosensor in modern electroanalytical field due to its high mechanical rigidity, highly economical, good electrochemical reactivity, ease of modification, renewal of electrode and low background current [1,2]. PTGPE has good application in analysis of drugs, detection of traces of metal ions and neurotransmitters. Metoclopramide (4-amino-5-chloro-N-[2-(diethylamino)ethyl]-2-methoxybenzamide) (MCP) as shown in Scheme 1 has wide range of clinical applications in different fields such as gastroenterology, gynaecology, surgery, radiology and cardiology. It shows antiemetic and prokinetic properties in disorders of decreased gastrointestinal motility and it is a dopamine receptor antagonist which also plays very important role as active ingredient of many pharmaceutical formations related with the modification of digestive behavior. MCP hydrochloride is commonly used in prevention and relief of nausea and vomiting [3-4] but mainly used in combination with chemotherapy, where drugs such as cisplatin, and some cytotoxic agents, are highly emetic [5].

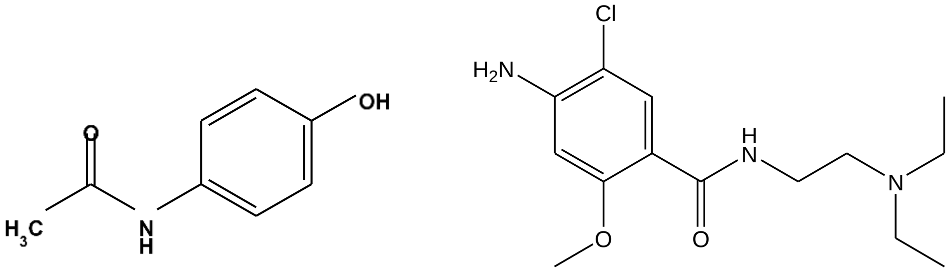

Scheme 1. *Chemical structure of AMP and MCP*

Acetaminophen (AMP) (paracetamol, N-acetyl-*p*-aminophenol) (Scheme 1) is a well-known drug which has extensive applications in pharma industries. It is a non-steroidal, antipyretic and anti-inflammatory drug [6]. It is the preferred alternative to Aspirin, specifically for patients who cannot tolerate Aspirin [7] and its use is one of the common causes of poisoning worldwide [8] and analgesic compound that has high therapeutic value. It is also used as a precursor in penicillin and as stabilizing agent for hydrogen peroxide, photographic chemical, *etc.* [9]. At the recommended dosage, there are no side effects. However, overdoses of acetaminophen cause liver and kidney damage [10] and may lead to death. It is suspected that a metabolite of acetaminophen is the actual hepatotoxic agent [11].

Acetaminophen/metoclopramide hydrochloride is an oral fixed dose combination containing the analgesic acetaminophen and the antiemetic metoclopramide hydrochloride. The combination is used to treat the migraine symptoms, both to relieve headache and to treat associated nausea and vomiting (the antiemetic). In addition to its direct antiemetic effect, MCP also stimulates gastric emptying (prokinetic), which is often delayed during migraine attacks, and accelerates the absorption of AMP. The combination of AMP and MCP has shown to enhance the analgesia relief when used to treat the arthritis pain.

As MCP is always given with AMP in any formulations, it is important to determine both the components simultaneously. Allthough there are different methods of anlysis of AMP [12] and MCP [13] separately mentioned in the literature, only a few classical methods are available [14-18] for the simultaneous determination of these componds. In the present study, the electrochemical method, a very sensitive and selective method of analysis using newly functionalised PTGPE has been used in the determination of AMP and MCP simultaneously. The proposed method was applied in real samples and pharmaceuticals.

Experimental aspects

Reagents and chemicals

The pencil-lead rods (HB 5 cm length and 0.5 mm in diameter) were purchased from a local stationary. AMP and MCP were purchased from Sigma Aldrich, India. Stock solutions of AMP and

MCP (1.0 mM) were freshly prepared in Millipore water. The phosphate buffer solutions (PBS) from pH 3.0 to 11.2 were prepared according to the method of Christian and Purdy [19]. Other reagents used were of analytical grade. All other solutions were prepared with Millipore water.

Instrumentation and analytical procedures

The voltammetric experiments were carried out on a CHI 630D electrochemical analysing system (CH instruments Inc., USA). The voltammetric experiments were carried out in a 10 ml single-compartment of three electrode glass cell with the reference electrode as silver electrode (Ag/AgCl), platinum as counter electrode and PTGPE as working electrode. pH measurements were carried with Elico LI120 pH meter (Elico Ltd., India). All experiments were performed at an ambient temperature of 298± 0.2K.

The area of the electrode was obtained by the cyclic voltametric method using 1.0 mM $K_3Fe(CN)_6$ at different scan rates. For a reversible process, the following Randles-Sevcik formula was used [20].

$$I_p = 0.4463(F^3/RT)^{1/2} n^{3/2} A_0 D_0^{1/2} C_0 v^{1/2} \quad (1)$$

where I_p refers to the anodic peak current, A_0 is the surface area of the electrode, n is number of electrons transferred, v is the scan rate, D_0 is the diffusion coefficient and C_0 is the concentration of $K_3Fe(CN)_6$. For 1.0 mM $K_3Fe(CN)_6$ in 0.1M KCl electrolyte, T = 298 K, R= 8.314 J $K^{-1}mol^{-1}$, F = 96,480 Coulombs mol^{-1}, n=1, and $D_0=7.6\times10^{-6} cm^2 s^{-1}$;then from the slope of the plot of I_p versus $v^{1/2}$, relation, the surface area was calculated. In our experiment the slope was 4.136×10^{-5}A $(Vs^{-1})^{1/2}$ and the area of electrode was calculated to be 0.1311 cm^2 which is three times more than that of the GPE.

Measurement procedure

Stock solutions of 1 mM of AMP and MCP were prepared by dissolving the desired amount in millipore water. Voltammograms were then recorded using voltammetric analyzer under the optimized parameters.

The parameters for DPV were, amplitude: 0.05 V; initial potential: 0.0 V; final potential: 1.4 V; increase in potential: 0.004 V; pulse width: 0.06s; sample width: quiet time: 2 s; sensitivity: 1×10^{-6} A V^{-1}.

Pre-treatment of electrode

The electrochemical treatment of GPE was performed in different supporting electrolytes by potential cycling between -2.0 V and +2.0 V with a scan rate of 50 mV s^{-1} for six scans. The investigated supporting electrolytes were each of 0.1 M H_3BO_3, $NaNO_3$, $HClO_4$, H_2SO_4, H_3PO_4, HCl, $LiClO_4$, and Na_2CO_3. The results showed that the GPE electrodes pretreated in 0.1 M HCl was the most selective and sensitive towards a AMP and MCP. So 0.1 M HCl was chosen for pre-treatment of electrodes. The prepared electrodes (PTGPE) were stored at room temperature in desiccators.

Preparation of real and pharmaceutical samples

The urine samples were collected from healthy humans and were diluted 100-fold with the phosphate buffer solution before analysis. Quantitative determination was performed by adding a standard solution of AMP and MCP to the detection system with the urine sample.

Metpar® tablets (Cipla, India) containing 500 mg of acetaminophen and 5 mg of metoclopramide were purchased from local pharmacy and were ground to a homogeneous fine powder in a mortar separately. A suitable amount of this powder was weighed and was treated with Millipore water for 20 minutes. The mixture was then filtered and solutions obtained from the filtration were diluted to 100 ml with Millipore water. Aliquots of this solution were analyzed within the calibration conditions.

Results and discussion

Cyclic voltammetry

Electrochemical response of a solution having homogeneous mixture of 1.0 µM of each AMP and MCP was estimated by cyclic voltammetry at 10 mV s^{-1} under optimized parameters using PTGPE. Anodic peaks for the oxidation of AMP and MCP were observed at 0.693 V and 1.123 V, respectively, as shown in Fig. 1. Reduction peak is absent in the reverse sweep for both compounds which clearly indicates the irreversibility of the electrode reaction. The peak intensities for PTGPE are better compared to the peak intensities obtained by using bare GPE.

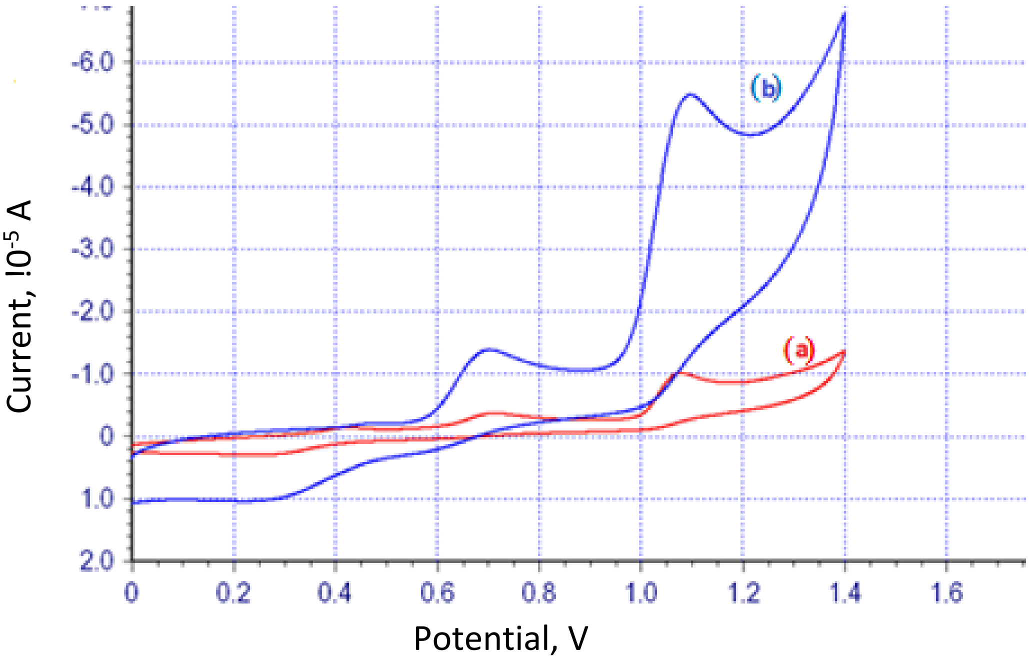

Fig. 1. *Comparison of electrochemical behavior of mixture of 1mM of AMP and 1mM of MCP at (a) bare GPE, (b) PTGPE, with scan rate 10 mV s^{-1} at pH 4.2.*

Effect of pH

The electro-oxidation of mixture of 1.0 µM each of AMP and MCP was studied over the pH range of 3.0–8.0 in phosphate buffer solution by differential pulse voltammetry which is as shown in Fig. 2A. The pH of solution influenced the peak current [21-23]. The pH dependence of the peak potential when DPV was used is shown in Fig. 2B (a and b). With an increase in pH of the solution, peak potential shifted to less positive values and was found to obey the following equations:

E_p = -0.0293 pH + 0.7214; r = 0.9821 for AMP

E_p = -0.0297 pH + 1.1483; r = 0.9615 for MCP

The best result with respect to sensitivity accompanied with sharper response and well separated peaks was obtained with pH = 4.2 (Fig. 2C), and hence it was selected for further experiments.

A

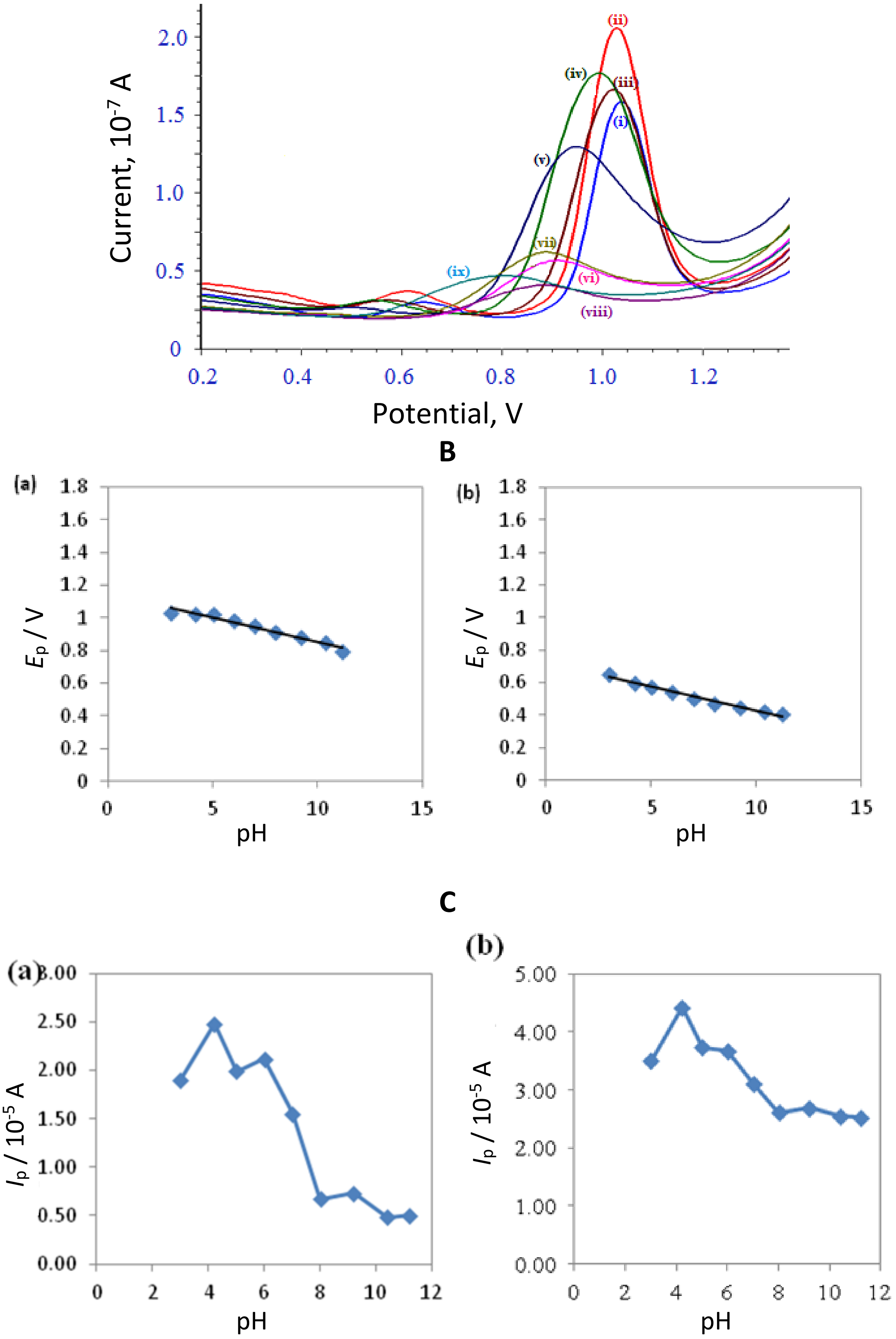

Fig. 2. *A - dependence of pH on the oxidation of mixture of AMP and MCP at pH (i) 3.0, (ii) 4.2, (iii) 5.0, (iv) 6.0, (v) 7.0, (vi) 8.0, (vii) 9.0, (viii) 10.4, (ix) 11.2;* ***B*** *- variation of peak potential with pH for (a) 1.0 µM MCP and (b) 1.0 µM AMP;* ***C*** *- variation of peak current with pH for (a) 1.0 µM MCP and (b)1.0 µM AMP*

Effect of scan rate

The effect of scan rate on the voltammetric oxidation of a mixture of AMP and MCP was examined by cyclic voltammetry between 10 to 190 mV s^{-1} (Fig. 3A). A linear relationship was observed between log I_p and log v, (Fig. 3B) corresponding to the following equations:

A

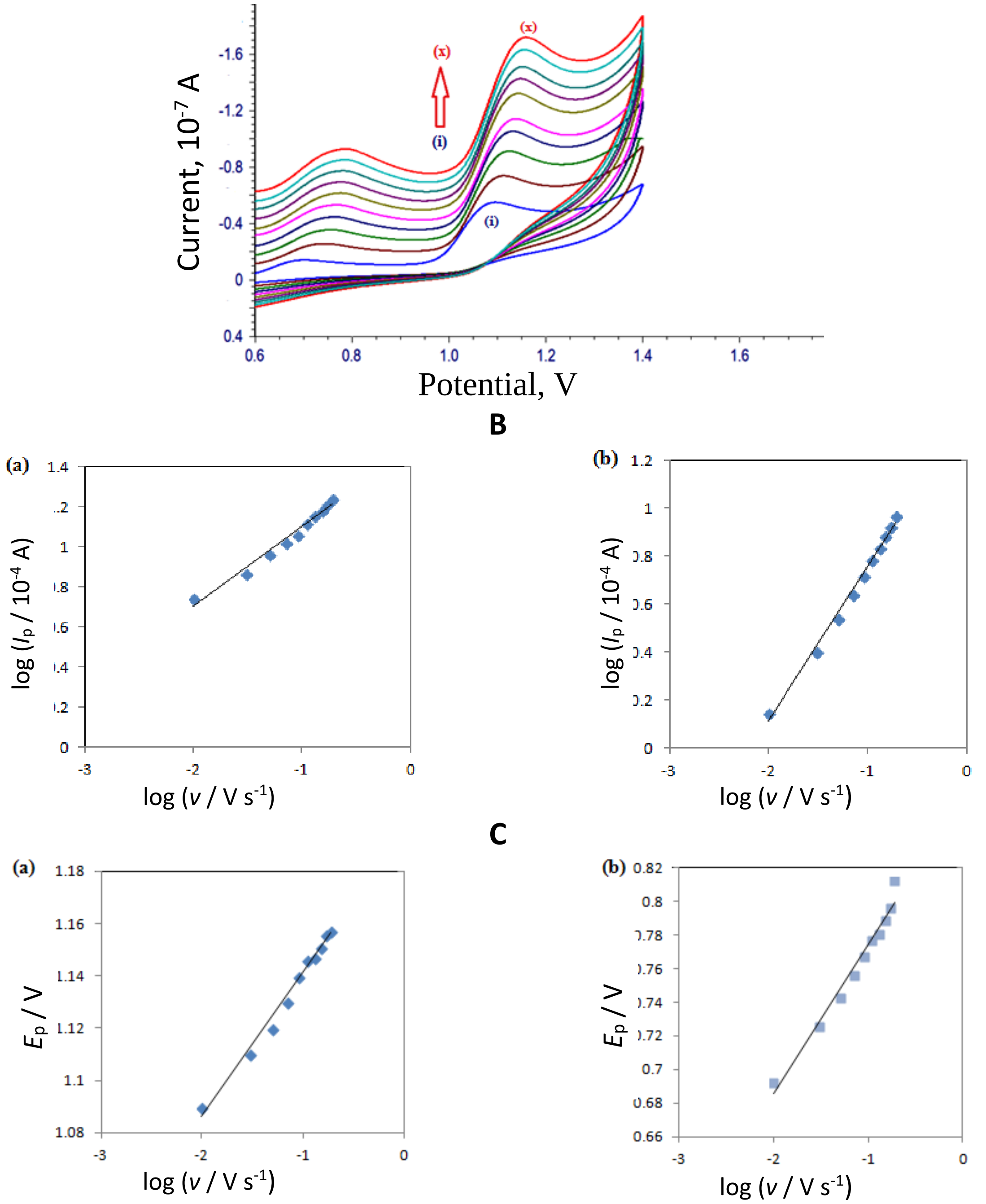

Fig. 3. A *- Effect of scan rate on the electro-oxidation of a mixture of AMP and MCP. (i) 10, (ii) 30, (iii) 50, (iv) 70, (v) 90, (vi) 110, (vii) 130, (viii) 150, (ix) 170, (x) 190 mV s-1;*
B *- observed dependence of peak current on the square root of scan rate for (a) MCP and (b) AMP;*
C *- plot of variation of peak potential with logarithm of scan rate for (a) MCP and (b) AMP.*

$\log I_p = 0.6508 \log v + 1.4111$, $r = 0.9942$ for AMP and

$\log I_p = 0.3989 \log v + 1.4981$, $r = 0.9796$ for MCP

The slopes of 0.65 V s^{-1} and 0.39 V s^{-1} were in the neighborhood of the theoretically expected value of 0.5 V s^{-1} for a purely diffusion controlled process [24] which, in turn, further confirms that the electro-oxidation of AMP and MCP were diffusion controlled. With an increase in scan rate, the peak potential shifted to a more positive value and a linear relationship was observed in the range 0.01 to 0.19 V s^{-1} as shown in Fig. 3C (a) and (b). The corresponding equations are expressed as:

$E_p = 0.0887 \log v + 0.8629$, $r = 0.9746$ for AMP and

$E_p = 0.0550 \log v + 1.1962$, $r = 0.9858$ for MCP

For an irreversible electrode process, according to Laviron [25], E_p is defined by the following equation (2).

$$E_p = E^0 + \frac{2.303RT}{\alpha nF}\log\left(\frac{RTk^0}{\alpha nF}\right) + \left(\frac{2.303RT}{\alpha nF}\right)\log v \tag{2}$$

where n is the number of electrons transferred, v is the scan rate, α is the transfer coefficient, k^0 is the standard heterogeneous rate constant of the reaction and E' is the formal redox potential. Other symbols have their usual meanings. Thus the value of αn was easily calculated from the slope, and k^0 was calculated from the intercept of E_p *vs.* log v. E^0 was obtained from the intercept of E_p vs. v plot by extrapolating to the vertical axis at $v = 0$ [24] Taking $T = 298$ K, $R = 8.314$ J K^{-1} mol^{-1} and $F = 96\ 480$ C mol^{-1}, the transfer coefficient (α) and number of electrons transferred (n) were calculated for both the drugs. The α value was calculated according to the Bard and Faulkner [26] equation (3).

$$\alpha = \frac{47.7}{E_p - E_{p/2}}\,\text{mV} \tag{3}$$

where $E_{p/2}$ is the potential when the current is at half the peak value. From this, the value of α was calculated to be 0.29 for AMP and 0.47 for MCP. Further, the number of electrons (n) transferred in the electro-oxidation of AMP and MCP were calculated to be 2.1≈2 and 2.28≈2.0, respectively.

Plausible mechanism

Based on the experimental results, the number of electrons transferred (n) for both the drugs were calculated to be two. Hence the probable electrooxidation mechanisms for both the drugs are proposed as given in Scheme 2, which are based on earlier works [27,28].

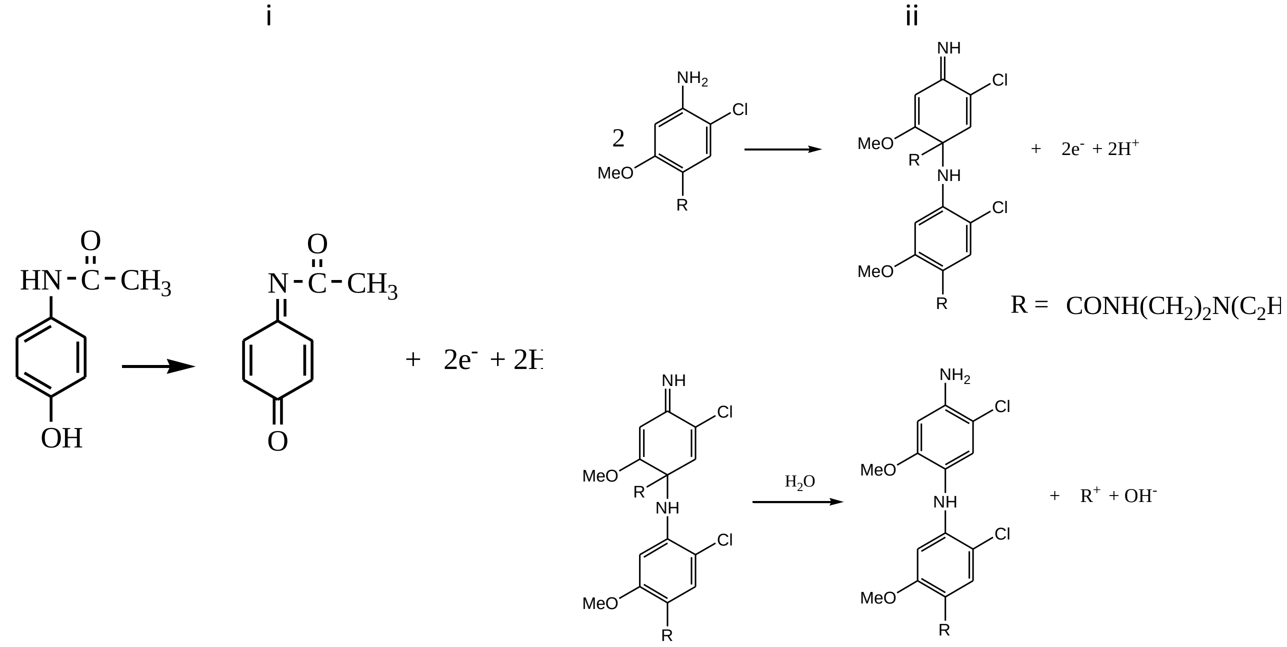

Scheme 2. *Proposed mechanisms for oxidation of (i) AMP and (ii) MCP*

Analytical application

To obtain an analytical curve for the sensor, quantitative analyses of the AMP and MCP concentrations were performed by DPV [29] at a PTGPE under the optimized experimental conditions. The oxidation of MCP occurs at high positive potential and there can be a chance of overlapping of MCP potential with the increasing concentration of drugs. Oxidation peak current was found to increase and no change in the peak current or potential of another drug indicates that these two drugs do not interact with each other. The peak current versus concentration of drug plots show a good linearity for AMP and MCP in certain concentration ranges as depicted in Fig. 4A and B. Peak current values were obtained by subtracting the background current of PBS and average of three replicate measurements were used to plot calibration curves. Linear regression equations for both the drugs arising from calibration plots are represented as:

$I_p = 0.212\,C + 0.344$, $r = 0.9703$ for AMP

$I_p = 0.928\,C + 1.257$, $r=0.9767$ for MCP

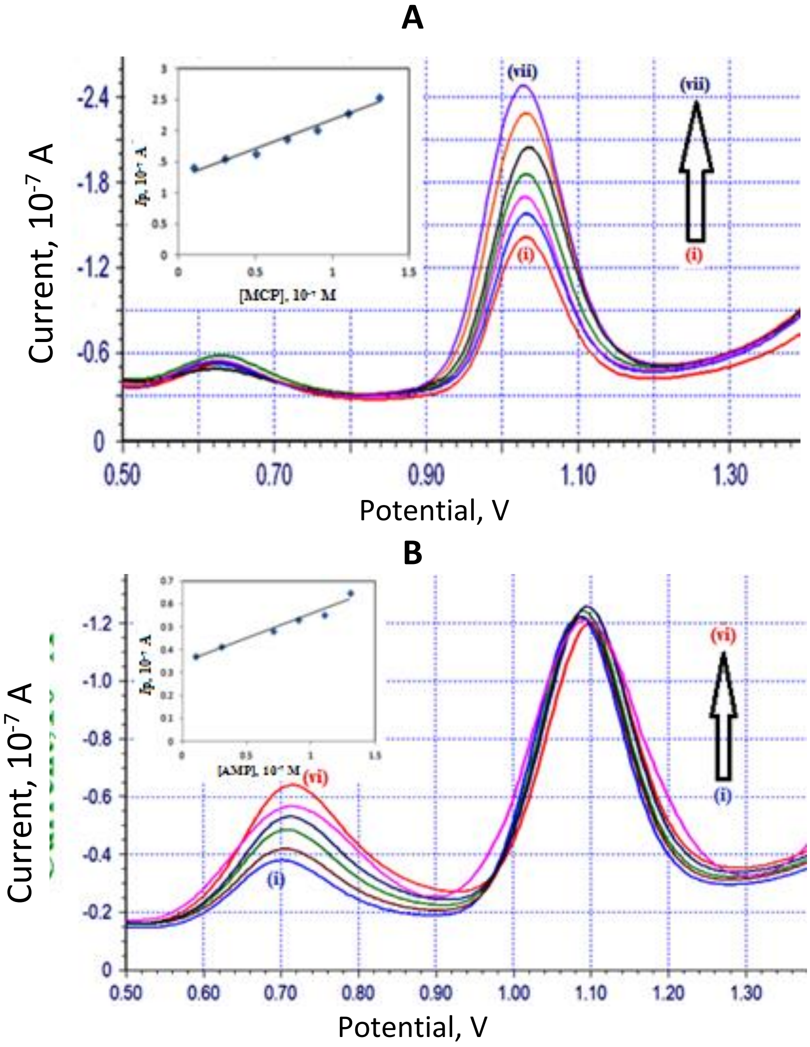

Fig. 4. *A - differential pulse voltammograms for increasing concentration of MCP at PTGPE (i) 1, (ii) 3, (iii) 5, (iv) 7, (v) 9, (vi) 11, (vii) 13, 10^{-7}M with AMP concentration 1×10^{-6}M.;* ***B*** *- differential pulse voltammograms for increasing concentration of AMP at PTGPE (i) 1, (ii) 3, (iii) 7, (iv) 9, (v) 11, (vi) 13, 10^{-7}M with MCP concentration 1x10^{-7}M.*

The limit of detection (LOD) and limit of quantification (LOQ) were calculated by using the formulae LOD = 3*s*/*m* and LOQ = 10*s*/*m*, where *s* is the standard deviation of peak current and *m* is the slope of calibration curves. LODs were found to be 3.25×10^{-9} M and 1.16×10^{-9} M for AMP and MCP respectively and the LOQs were calculated as 10.84×10^{-9} M and 3.88×10^{-9} M, respectively. Since, it is important to calculate validation parameters for any analytical method, the calibration characteristics obtained for MCP and AMP are given in Table 1.

Table 1. *The calibration characteristics for metoclopramide and acetaminophen at PTGPE.*

	MCP	AMP
Linearity range, 10^{-7} M	0.1-1.1	0.1-1.1
Slope of the calibration plot	0.928	0.212
Intercept	1.275	0.344
Correlation coefficient (*r*)	0.9767	0.9703
RSD of slope, %	1.21	0.82
RSD of intercept, %	0.12	0.65
Number of data points	5	5
LOD, nM	1.16	3.25
LOQ, nM	3.88	10.84
Repeatability of peak current, %	0.79	1.14
Repeatability of peak potential, %	0.51	0.35
Reproducibility of peak current, %	0.92	0.71
Reproducibility of peak potential, %	0.24	0.43

The precision of the method was calculated by repeating five experiments on the same day in standard conditions (repeatability) and over two days from the different standard solutions (reproducibility). For these studies 1.0×10^{-6} M of each of AMP and MCP standard solutions were used. From RSD values of peak potential and peak current between day reproducibility were similar to that of within a day if the temperature was kept almost unchanged which shows the excellent stability and reproducibility of PTGPE.

Effect of excipients

The effect of some common excipients used commonly in pharmaceutical preparations was examined. The tolerance limit was defined as the maximum concentration of the interfering substance that caused less than 5 % error for the determination of AMP and MCP. The effects of these excipients on the voltammetric response were obtained by analyzing sample solutions containing a fixed amount of AMP and MCP (1.0×10^{-6} M) spiked with various amounts of each excipient under the same experimental conditions. The experimental results showed that a hundred-fold excess of gum acacia, citric acid, dextrose, glucose, lactose, tartaric acid and sucrose did not interfere with the voltammetric signal of AMP and MCP. Hence, these compounds need not be extracted from these tablet additives prior to their determination in tablets.

Detection of AMP and MCP in human urine samples

The developed DPV method for the AMP and MCP determination was applied to human urine samples. The recoveries from urine were measured by spiking drug free urine with known amounts of AMP and MCP. The urine samples were diluted 100 times with the PBS before analysis without further pretreatment. A quantitative analysis was carried out by adding the standard solutions of AMP and MCP into the detection system of urine samples. The peak current increased linearly in height. The calibration plot was used for the determination of spiked AMP and MCP in urine samples. The results of four urine samples obtained are listed in Table 2. Thus, satisfactory recoveries of the analytes from the real samples were in a good agreement with the concentration ranges studied and the real ranges encountered in the urine samples when treated with drug, make the developed method applicable in clinical analysis.

Table 2. *Results of analysis of metoclopramide and acetaminophen in spiked urine samples*

MCP added, 10^{-8} M	Quantity found$^{(a),}$ 10^{-8} M	Average recovery, %	RSD^{a}, %
		Metoclopramide	
10	9.7	97.0	1.91
15	14.5	96.6	2.20
20	19.2	96.0	2.12
25	24.6	98.2	2.66
30	29.6	98.8	1.59
35	34.2	97.4	2.21
		Acetaminophen	
10	9.5	95.0	1.83
15	14.9	99.5	1.24
20	20.1	100.5	2.62
25	24.4	97.6	2.31
30	29.1	98.8	1.02
35	34.1	96.4	1.61

a -average of five determinations

Determination of AMP and MCP in pharmaceutical samples

This method was applied for the determination of AMP and MCP in tablets. As shown in Table 3, the content of AMP and MCP was calculated to be 495.1 mg/tablet (the nominal content is 500 mg/tablet) and 9.7 mg/tablet (the nominal content is 10 mg/tablet) respectively. To validate and obtain the accuracy and precision of the developed method, recovery studies were performed at different drug concentrations by the standard addition method. For the present study, known quantities of AMP and MCP were mixed separately with definite amounts of pre-analyzed formulations and mixtures were analyzed as before. Table 3 shows the measurement results, and the average recovery was found to be 99.02 % and 97.0 % for AMP and MCP respectively. The F and Student t tests were also calculated with confidential level of 95 % and are shown in Table 3.

Table 3. *Results of analysis of tablet containing both the analytes (acetaminophen 500 mg and metoclopramide 10 mg) in commercially available tablet samples by DPV*

	Acetaminophen	Metoclopramide
Labeled claim, mg	500.00	10.00
Quantity found, mg	495.10	9.70
Recovery^{a}, %	99.02	97.00
RSD^{a}, %	1.92	2.31
t- value at 95% confidence level	0.16	0.21
F-value at 95% confidence level	1.47	1.76

a -average of five determinations

Conclusion

The pre-treated pencil graphite electrode was applied successfully as a sensor for fast, accurate and simultaneous determination of AMP and MCP in some pharmaceutical samples. The present method is a good alternative for the analytical determination of AMP and MCP simultaneously, because it is simple, sensitive, accurate, fast, and inexpensive. The results were successfully applied in urine samples and pharmaceuticals. Furthermore, the present method could possibly be employed for pharmacokinetic studies and also in clinical and quality control laboratories.

***Acknowledgement**: The author thanks the UGC, New Delhi for the award of UGC-BSR faculty fellowship to Dr. S. T. N.*

References

[1] J. I. Gowda, S.T.Nandibewoor, *Anal. Methods* **6** (2014) 5147-5154.
[2] E. Alipour, S. Gasemlou, *Anal. Methods* **4** (2012) 2962-2969.
[3] I. Parlak, R. Atilla, M. Cicek, M. Parlak, B. Erdur, M. Guryay, M. Sever, S. Karaduman, *Emerg. Med. J.* **22** (2005) 621-624.
[4] P. Norouzi, M. R. Ganjali, P. Matloobi, *Electrochem. Commun.* **7** (2005) 333-338.
[5] C. P. Page, M. J. Curtis, M. C. Sutter, M. J. A. Walker, B. B. Hoffman, *Farmacología Integrada*, Ed. Harcourt. España. 1998.
[6] L. J. Roberts, J. D. Morrow, in: *The Pharmacological Basis of Therapeutics*, 10th ed., J. G. Hardman, L. E. Limbird, A. G. Gilman (Eds.), McGraw-Hill, London, 2001.
[7] R. V. Blanke, W. J. Decker, in: *Textbook of Clinical Chemistry*, N.W. Tietz (Ed.), W.B. Saunders, Philadelphia, 1986.
[8] D. Gunnell, V. Murray, K. Hawton, *Suicide Life Threat. Behav*. **30** (2000) 313-326.
[9] W. A. Martindale, *The Extra Pharmacopoeia*, 27th ed., The Pharmaceutical Press, London, 1979.
[10] B. D. Clayton, Y. N. Stock, *Basic Pharmacology for Nurses*, Mosby Inc, Harcourt Health Sciences Company, St. Louis, Mo, USA, 2001.
[11] N. Wangfuengkanagul, O. Chailapakul, *J. Pharm. Biomed. Anal.* **28** (2002) 841-847.
[12] J. I. Gowda, D. G. Gunjiganvi, N. B. Sunagar, M. N. Bhat, S. T. Nandibewoor, *RSC Adv.* **5** (2015) 49045-49053.
[13] S. M. Patil, S. T. Nandibewoor, *Anal. Bioanal. Electrochem*. **7** (2015) 387-400.
[14] S. J.Wadher, P. R.Pathankar, M. Puranik, R.O. Ganjiwale, P. G. Yeole, *Ind. J. Pharm. Sci.***70** (2008) 393-395.
[15] A. E. El-Aleem, S. M. Khalile, A. M. Badawy, O. K. El-Naggar. *Research J. Pharma. Dosage Forms and Tech*. **5** (2013) 270-274.
[16] G. Shubhangee, K. Manish, N. Swapnil, *Int. J. Pharm. Li. Sci*, **1** (2010) 127-132.
[17] N. P. Dudhane, S. S.Vidhate. B. H.Borkar, R. T. Lohiya, M. J. Umekar, *J. Pharm. Sci. & Res.* **2** (2010) 48-52.
[18] G. Vamshikrishna, M. Neelima, M. Bhavani, G,Sreekanth, S. Shobha Rani. *IOSR J. Pharm. Bio. Sci.* **9** (201) 69-78.
[19] G. D. Christian, W. C. Purdy, *J. Electroanal. Chem.* **3** (1962) 363-367.
[20] B. Rezaei, S. Damiri, *Sens. Actuators B,* **134** (2008) 324-331.
[21] B. D. Topal, B. Bozal, B. T. Demircigil, B. Ulsu, S.A. Ozkan, *Electroanalysis*. **21** (2009) 2427-2439.
[22] J. Wang, *Electroanalytical Techniques in Clinical Chemistry and Laboratory Medicine*; VCH: New York, 1988.
[23] P. T. Kissinger, W. R. Heineman, *Laboratory Techniques in Electroanalytical Chemistry*, 2nd ed.; Marcel Dekker: New York, 1996.
[24] D. K. Gosser, *Cyclic Voltammetry: Simulation and Analysis of Reaction Mechanisms*, VCH, New York, 1993.
[25] E. Laviron, *J. Electroanal. Chem*. **101** (1979) 19-21.
[26] J. Bard, L. R. Faulkner, *Electrochemical Methods Fundamentals and Applications*, Wiley, 2nd ed, 2004,

[27] B. Habibi, M. Jahanbakhshi, M. H. Pournaghi-Azar, *Analytical Biochemistry*. **411** (2011) 167–175.
[28] S. Shahrokhian, L. Naderi and M. Ghalkhani, *Electroanalysis* **27 (**2015) 2637 – 2644.
[29] N. L. Teradal, S. N. Prashanth, J. Seetharamappa, *J. Electrochem. Sci. Eng.* **2** (2012) 67-75.